APPENDIX A

1. NEW BATHYMETRY AND GEOPHYSICAL DATA ALONG SOUTHERN CASCADIA

The tsunami hazard modeling referenced by Page and Nishenko (2015) used the most up-to-date bathymetric information available. As they stated in their report, they combined several data to construct topography and bathymetry including:

- USGS 7.5 minute 10m DEM for Buhne Hill and HBGS site -
- NOAA 1:25,000 navigation charts for Humboldt Bay
- NOSS National Geophysical Data 3 arc second (90 m) Coastal Relief Model for continental shelf
- ETOPO2vs 2arc minute (~4km) for open ocean
- 2008 - 5 m lidar and CICORE multibeam sonar for North Bay, North Spit, South Bay, south spit and main shipping channels

There have been some significant updates to some data sources that may be relevant to further tsunami hazard models at Buhne Hill.

1.1 Nearshore and within Humboldt Bay bathymetry, including onland topography

National Oceanic and Atmospheric Administration (NOAA) lidar collected in 2019 resulting in a 1 foot DEM with a point density of 35.44 pts.m^2. Available at https://portal.opentopography.org/noaaDataset?noaaID=9026. It should be noted that this lidar distribution does not include deep channels within Humboldt Bay (Figure 1).

Prior to the 2019 lidar dataset the California Coastal Conservancy (jointly with other agencies) provided coverage of nearshore (500 m) topography along with bathymetry out to 3 miles (Figure 2). This data product included 2009-2011 data merged with 2013 data. The point density for these data are more sparse (1.34 pts/m^2) than the 2019 lidar data. These data are available at https://portal.opentopography.org/noaaDataset?noaaID=2612

1.2 Offshore bathymetry

Hill et al (2020) use 2018 to 2019 multibeam bathymetry, sparker multichannel seismic and chirp sub-bottom data (Balster-Gee et al., 2020a, 2020b) along with existing data from the Ocean Exploration Trust, Monterey Bay Aquarium Research Institute, USGS, National Oceanic and Atmospheric Administration (NOAA) and University-National Oceanographic Laboratory System (UNOLS) vessels to evaluate offshore structure and geomorphology along the Cascadia margin from Cape Mendocino to Oregon border (Figure 3). This resulted in nearly complete bathymetric coverage with 10 to 40 m resolution and dense crossings of seismic reflection profiles throughout the region (Hill et al., 2020). The data are available at https://www.ngdc.noaa.gov and https://walrus.wr.usgs.gov/NAMSS/.

Additionally, Ryan et al.(2009) provide global coverage of multi-resolution bathymetry from ship cruises and satellite altimetry in what they refer to as The Global Multi-Resolution Topography synthesis. This is a series hierarchical tiles “with digital elevations and shaded relief imagery spanning nine magnification doublings from pole to pole.” Data are accessed via a maptool online at https://www.gmrt.org/index.php. The portal is active and was last updated May 2024. This is a curation of 1,490 cruises.

FIGURES

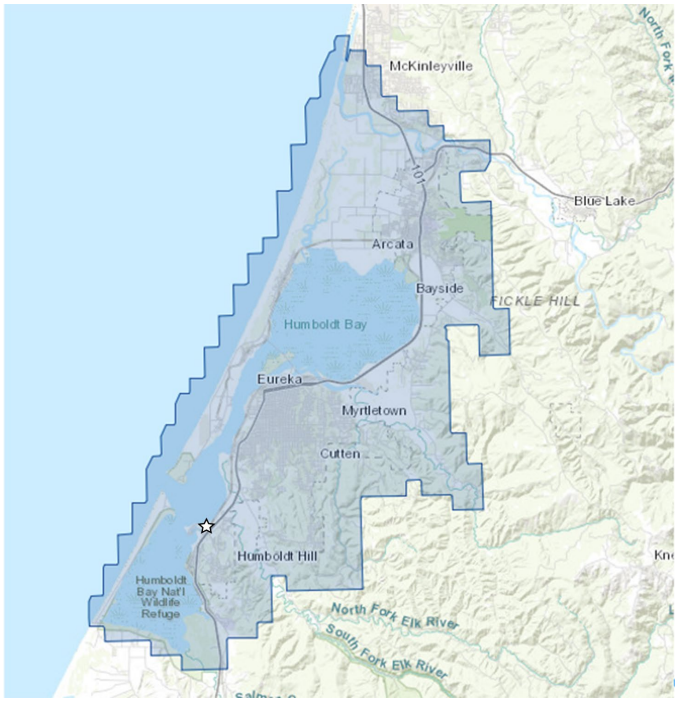

Figure 1 – Coverage map for 2019 NOAA lidar. Star indicates approximate location of Buhne Hill and ISFSI.

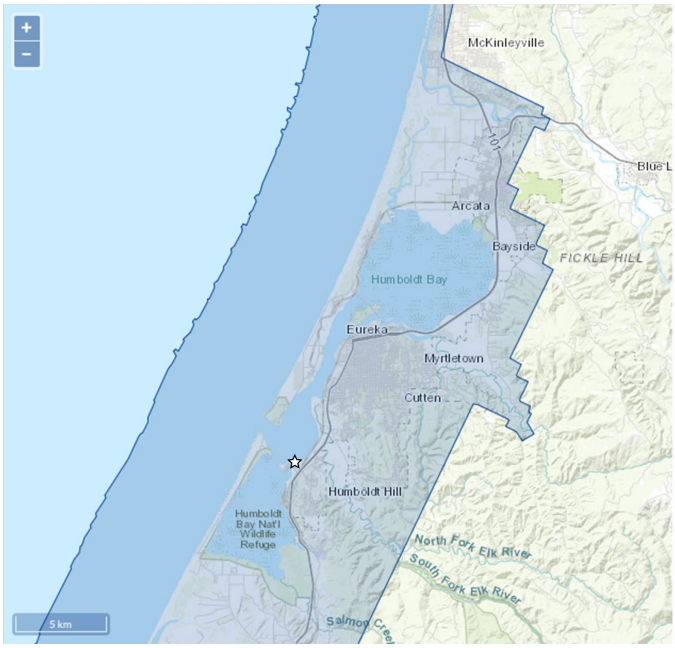

Figure 2 – Coverage for 2009-2011 Topobathy lidar from approximately 10 m elevation onland to California 3 mile state water boundary. Star indicates approximate location of Buhne Hill and ISFSI.

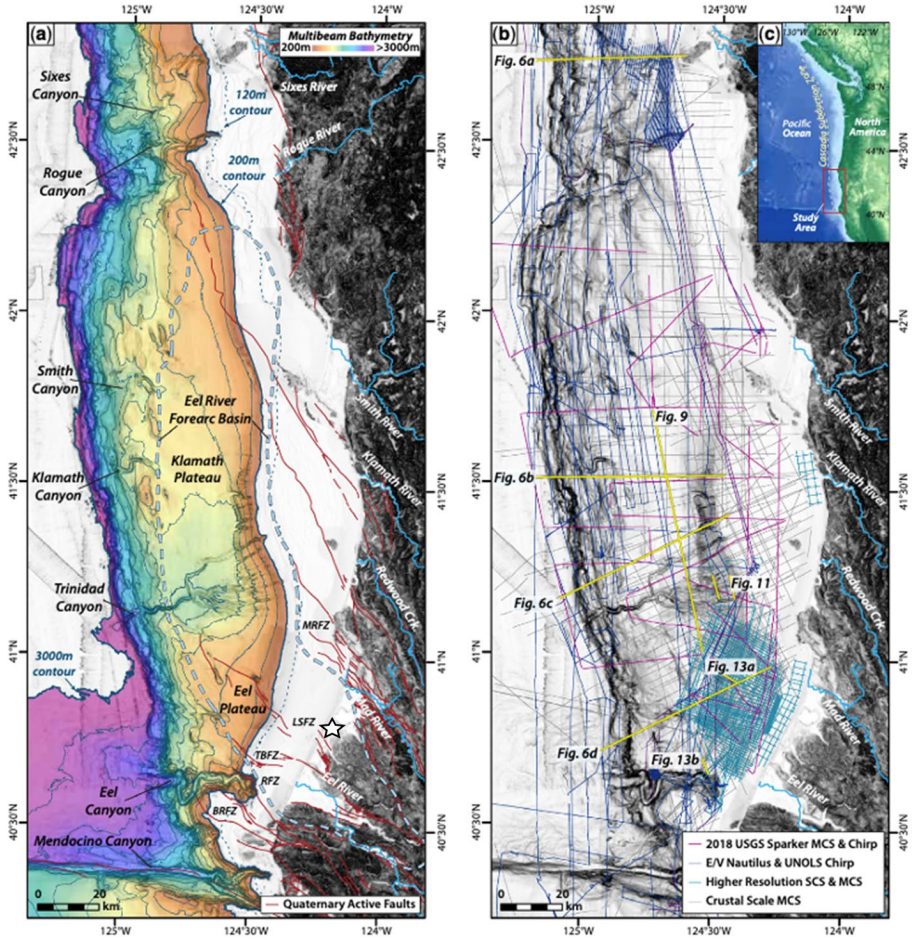

Figure 3 - (a) Location map showing the bathymetry, major rivers and structural features of the southern Cascadia region (from Hill et al. 2020), which is bounded to the north by Rogue and Sixes canyons, and to the south by the Mendocino fault at Mendocino Canyon. The Eel River forearc basin (dashed outline) lies primarily offshore. Dark red lines are faults from the USGS Quaternary Fault and Fold Database. Bathymetric contours are every 200 m; several key isobaths are noted, including the approximate sea-level lowstand shoreline (c. 120 m), the shelf break at c. 200 m and the c. 3000 m isobath that marks the base of slope along much of the region. (b) Trackline coverage of seismic datasets for southern Cascadia, including a range of high-resolution Sparker and Air Gun Multi-Channel Seismics (MCS) and Chirp sub-bottom profiles, as well as legacy and crustal-scale MCS from the 1970s to 1990s. Star indicates approximate location of Buhne Hill and the ISFSI.

REFERENCES

Balster-Gee, A.F., Hill, J.C., and O'Brien, T.F., 2020b, Archive of boomer sub bottom data collected off shore Eureka, California during USGS field activity W-1-96-NC from 1996-06-29 to 1996-07-07: US Geological Survey Data Release, doi:https://doi.org/10.5066/ P950276G.

Balster-Gee, A.F., Kluesner, J.W., Watt, J.T., Hill, J.C., Brothers, D.S., Michalak, M.J., and O'Shea, D., 2020a, Multichannel minisparker seismic reflection data of USGS field activity 2018-658-FA collected between Cape Blanco and the Mendocino Triple Junction from 2018-10-04 to 2018-10-18: US Geological Survey Data Release, doi:https://doi.org/10.5066/P9R3QM97.

Hill, J.C., Watt, J.T., Brothers, D.S., and Kluesner, J.W., 2020, Submarine canyons, slope failures and mass transport processes in southern Cascadia: Geological Society, London, Special Publications, p. SP500-2019–169, doi:10.1144/SP500-2019-169.

Page, W.D., and Nishenko, S., 2015, Assessment of Potential Tsuanami Runup at the Humboldt Bay Generating Station Site: PG&E Internal, 89 p.

Ryan, W.B.F. et al., 2009, Global Multi-Resolution Topography synthesis: Geochemistry, Geophysics, Geosystems, v. 10, doi:10.1029/2008GC002332.

APPENDIX B

1 Introduction: Vertical Land Motion

As a basis for this review we consider the analysis by Lettis and Thompson (2020) that incorporate climatically-induced sea level rise (SLR), long-term regional uplift, interseismic and coseismic vertical land motion (VLM) into their 100 year assessment of relative sea level change at Buhne Point. We also compare more recent data to those considered by Page and Nishenko (2015). Tables comparing projected sea level to various target years (typically 2000, 2120 and 2150) and SLR rates are provided in Tables 1 and 2.

Vertical land motion (VLM) encompasses both uplift (positive) and subsidence (negative) of a datum on land. Relative sea level (RSL) change is relative change between absolute changes in sea level and VLM. VLM can be caused by several factors which predominantly include crustal rebound due to the rapid unloading of glacial ice, referred to as glacial isostatic adjustment (GIA) and tectonic forces. Absolute sea level change can be influenced by changes in sea ice volumes, changes in water temperature and salinity and changes in the bathymetry of ocean basins (Patton et al., 2017; Frederikse et al., 2020; Patton et al., 2023a). Changes in RSL can be quantified by accounting for VLM and absolute sea level changes at a site. Along an active tectonic margin two influences of VLM occur at different temporal and physical scales. They are coseismic and interseismic land-level changes. Coseismic changes tend to be episodic, occurring over periods of seconds to minutes and can be accompanied by significant amounts of uplift or subsidence (up to 10's of meters). Interseismic land-level changes occur between coseismic events, occur slowly (decades to centuries) and have small rates of change (mm or cm per year).

Coseismic land-level changes refer to abrupt movements either up (uplift) or down (subsidence) during large earthquakes. Coseismic land-level changes may accompany large magnitude earthquakes, including those possible from rupture of the Cascadia Subduction Zone (CSZ) megathrust and/or large local thrust or reverse faults within the accretionary prism in the vicinity of Humboldt Bay. The vertical motion is the result of land movement from fault rupture, and in the case of subduction zone earthquakes (such as those along the CSZ megathrust) areas of sudden vertical land-level change may be found in coastal areas along the length of the subduction zone (Atwater et al., 2003; Imakiire and Koarai, 2012). In subduction zone earthquakes, whether the vertical land movement is up, down, or neutral depends on the location of the site relative to a flexure point in the overriding plate above the megathrust. For example, for the 1964 M9.2 Alaska earthquake, areas of uplift occurred largely offshore, whereas areas of subsidence, as much as 2-3 m in some places (Plafker, 1969), occurred onshore along the coast (Carver and Plafker, 2008; Freymueller et al., 2013; Shennan et al., 2014). In the most recent full-margin rupture of the CSZ, in 1700 C.E., all coastal sites evaluated between Northern California and Vancouver Island experienced coseismic subsidence with no evidence for areas of coseismic uplift during this event. For the 1964 Alaska earthquake, the absolute amounts of subsidence measured at some locations was attributed to vertical land motion from crustal deformation with the added effects of liquefaction of unconsolidated deposits (Walsh et al., 1995).

2 Coseismic Subsidence

Unlike the temporary inundation from climatic events such as coastal storms or floods, coseismically subsided areas abruptly drop from elevations unaffected by sea level to areas permanently inundated by

tides. A clear modern example of this are the large industrial and agricultural areas on the Sendai plain that subsided during the 2011 M9.2 Tohoku-aki earthquake and are now continuously inundated by seawater (Imakiire and Koarai, 2012). Relatively high-density geodetic stations throughout Japan recorded abrupt coseismic VLM during the earthquake where up to 1.2 m of subsidence occurred (Figure 1). Therefore, the inherent risk to buildings or infrastructure close to sea level in areas adjacent to subduction zones, such as the ISFSI on Buhne Hill located in the southern CSZ, lies in their potential to become submerged and unusable following the earthquake-induced subsidence.

It has been well-established that strong evidence for past instances of abrupt coseismic subsidence at coastal sites is stratigraphic juxtaposition of two dissimilar kinds of sedimentary deposits in sharp contact with one another: an organic-rich soil (peat) indicating a former marsh, meadow, or coastal woodland—a type of environment which would be infrequently or possibly never submerged by tides—abruptly overlain by thick deposits of mud indicative of a lower intertidal setting such as a tidal flat (as depicted in Figure 2). This stratigraphic signature is observed at coastal and estuarine sites along the length of the CSZ and records the conversion of vegetated areas to tidal flats as a result of coseismic subsidence. These unusual mud-over-soil sequences are similarly observed at numerous locations along Humboldt Bay and the Eel River estuary (Hemphill-Haley, 2017; Jacoby et al., 1995; Padgett, 2019; Padgett et al., 2021; 2022; Patton, 2004; Pritchard, 2004; Valentine, 1992; Valentine et al., 2012; Vick, 1988; Li, 1992) and are interpreted, as elsewhere, of recording coseismic subsidence from past CSZ megathrust earthquakes.

The most recent of the paleoseismic studies in Humboldt Bay (Padgett et al., 2019, 2021, 2022) (Figures 3 and 4) focused on sites in northern Humboldt Bay (Arcata Bay) where they described four past incidences of earthquake-driven subsidence from CSZ earthquakes. From multiple radiocarbon dates, the ages of the four events are identified as:

(1) 1700 C.E.;

(2) ~875 cal yrs B.P.[1];

(3) 1,120 cal yrs B.P.; and

(4) ~1,620 cal yrs B.P.

The estimated amounts of coseismic subsidence from these past earthquakes, determined statistically from changes in microfossil assemblages across the soil-mud contacts, are about 0.8 ± 0.5 m (2.6 ± 1.6 ft) for the earthquake in 1700 C.E.; 0.4 ± 0.4 (1.3 ft) for the earthquake in 875 cal yr B.P.; 0.8 ± 0.5 m (2.6 ± 1.6 ft) and likely greater than 0.9 m (3ft) for the oldest recorded event in 1,620 cal yr B.P. (Padgett et al., 2021). Comparable qualitative or semi-quantitative estimates for subsidence were determined from earlier studies, although without the precision of the later study by Padgett et al. (2021, 2022).

The Padgett et al. (2022) study revised the subsidence estimates by using stratigraphic control and analysis of multiple cores collected at each of the sites investigated during 2021. By using multiple cores, they were able to assess the variability of the subsidence estimates for the last three events reported in Padgett et al. (2021). Their analysis did not include the 1,620 cal yr B.P. event. They were able to estimate an average and range for those events (Table 1). Thus, the revised estimates are an average of 0.6

[1] The unit "cal yrs B.P." refers to "calibrated radiocarbon years before present" with "present" defined as the year 1950 C.E.

± 0.1 m (2 ± 0.3 ft) for the 1700 C.E. earthquake; an average of 0.4 ± 0.2 m (1.3 ± 0.7 ft) for the ca. 875 cal yr BP earthquake and 0.7 ± 0.2 m (2.6 ± 0.7 ft) for the ca. 1120 cal yr BP event (Padgett et al., 2022).

Thus, the combined results of the various paleoseismic studies for northern Humboldt Bay suggest that coseismic subsidence on the order of 0.5 - 1 m (1.6 – 3.3 ft) or more is a possibility for future CSZ earthquakes.

Both Valentine et al. (2012) and Padgett et al. (2021, 2022) note the occurrence of at least one possible episode of subsidence about 500 years ago that does not appear to correlate to well-documented CSZ earthquakes. Padgett et al. (2021) do not specify a possible source of the buried soil of this age in the Mad River slough, cautioning that the dynamic sedimentary processes in Mad River slough, including past altering of the slough channel from dredging, may make the stratigraphic record at that site particularly more complex and less reliable. Valentine et al. (2012, p. 1070) speculate that the possible evidence for subsidence at about 500 years ago in Mad River slough and sites farther to the south in Humboldt Bay may be recording coseismic land-level change from past rupture on faults in the fold and thrust belt. They noted that the "expected effects" of rupture on the Little Salmon fault or Mad River fault zone would be "*minor amounts of subsidence within the frontal syncline adjacent to the fault, larger amounts of subsidence in the syncline behind the fault, or uplift."* They also state that "*For an event on the Mad River fault zone, subsidence would be expected in the Freshwater syncline (Mad River slough)… Subsidence would be variable from 0.25–1 m in the frontal portion to 1–3 m in the back basin*." However, they express uncertainties as to the possible record of subsidence from fold and thrust earthquakes, conceding that (p. 1074): '*There is not sufficient evidence from the data to evaluate the cause(s) of this RSL*[2] [Relative Sea Level] *event* [500 years ago] *or whether it represents a coseismic subsidence due to an earthquake or coincidental RSL changes at several sites. If an earthquake caused the observed RSL changes, then based on the distribution of the changes the earthquake was probably a local event*."

There is no recent work in southern Humboldt Bay since Witter et al. (2001, p. 44) who compiled evidence for coseismic subsidence accompanying rupture of the Little Salmon fault, and reported that the "*data suggest that submergence in the footwall of the Little Salmon fault occurs during upper-plate earthquakes." Significantly, based on the results at their study sites near College of the Redwoods and Hookton Slough, they concluded that although subsidence accompanied rupture on the LSF, the LSF ruptures were in turn triggered by and coincident with ruptures in the CSZ megathrust." Evidence for subsidence of the [LSF] western fault scarp along with stratigraphic records of abrupt soil submergence suggests that coseismic subsidence of the Humboldt Bay region also accompanied upper-plate seismicity. We conclude that where evidence for slip on the Little Salmon fault and regional coseismic subsidence coincide, the evidence supports an interpretation of upper-plate faulting triggered by rupture on the southern Cascadia plate-interface*" (Witter et al., 2001, p. 41). Therefore, it is possible that Humboldt Bay coseismic subsidence may have, occasionally, included forcing rupture on faults in the accretionary prism in addition to the deformation associated with rupture of the southern CSZ megathrust. This is a situation unique to the North Coast where the accretionary wedge of the subduction zone is located onshore.

[2] RSL – "relative sea level."

3 Coseismic and Interseismic Uplift

There is currently no direct evidence for coseismic uplift along the CSZ related to a megathrust only earthquakes. All sites have experienced coseismic subsidence (for example Nelson et al., 2006; Hutchinson and Clague, 2017), however, an uplift signal has been documented along the north coast of Humboldt county (Woodward-Clyde Consultants, 1980; Burke and Carver, 1992; Swan et al., 2002; McCrory, 2000). This is represented as a series of marine terraces that occur along the hills and coastal exposures of Humboldt Bay (Figure 5) and throughout Oregon and Washington. It is thought that this permanent, long-term strain is evidence that megathrust earthquakes do not completely release all interseismic elastic strain stored along the subduction zone (Stanton et al., 2024). At Humboldt Bay, these terraces record the progressive regional uplift of the accretionary sediments above the megathrust while adjacent synclines are absent of terraces. Relative dating (soil development and vertical position) and few absolute dates suggest that these terraces record at least 200,000 years of uplift along these structures. Evidence of a longer record of uplift is not apparent in the terraces due to erosion. An older record of uplift is recorded in separation of the base of Neogene sediments forming the cores of the folds where it is estimated that more than 3,400 m of separation exists across the Little Salmon and Table Bluff faults (Ogle, 1953; Kelsey and Carver, 1988; Swan et al., 2002; Vadurro, 2006). These terraces record a longer-term trend of tectonic uplift that is accumulated over many episodes of megathrust activity and not the interspersed, episodic coseismic events.

North of Humboldt Bay, near Trinidad, CA, Padgett et al. (2019) describe upper plate deformation associated with the Trinidad fault and anticline (Figures 6 and 7). They identified fine-grained, uplifted and deformed marine terraces ranging in age from 80ka to <500 ka. Using paleosol weathering relative age parameters, they correlated these terraces to the marine oxygen isotope sea level curve. They estimated an average maximum uplift rate of ~1mm/yr (3.3ft/ky) for these terraces. This estimate is approximately 3 times that described near Buhne Point by Lettis and Thompson (2020) for the long-term regional uplift, 0.36 mm/yr (1.2 ft/ky), while Page and Nishenko (2015) report that the National Research Council (2012) estimated the area north of Cape Mendocino is rising interseismically at 1.5 mm/yr (4.96 ft/ky) to 3.0 mm/yr (9.9 ft/ky). Patton et al. (2023) report an interseismic uplift signal near Trinidad of approximately 2.66 mm/yr (0.01 ft/yr).

4 Interseismic Subsidence at Humboldt Bay

In addition to episodic coseismic subsidence at Humboldt Bay from great earthquakes, Patton et al. (2017, 2023) have shown that Humboldt Bay is interseismically subsiding on the order of millimeters per year (Figures 8, 9 and 10), resulting in relative sea level rise at Humboldt Bay that is “2-3 times greater than anywhere else in California” (Patton et al., 2017, p.3). Patton et al. (2017) report the rates of land subsidence for five locations on Humboldt Bay: South Humboldt Bay/Hookton Slough (-3.56 mm/yr); Fields Landing (-2.66 mm/yr); North Spit (-3.21 mm/yr); Samoa (-3.05 mm/yr); and Arcata Bay/Mad River Slough (-1.58 mm/yr). Patton et al. (2023) use data from tide gages, benchmark releveling and Global Navigational Satellite System (GNSS) to reevaluate vertical land motion (VLM) rates in the Humboldt Bay area. One implication is that these relatively high rates of interseismic subsidence are recording the effects of a locked megathrust boundary, with the overriding North America plate being pulled downward as subduction of the Gorda plate continues beneath it (Savage et al., 1991; Hyndman and Wang, 1995; Wang et al., 2003; Wang and Tréhu, 2016). Another plausible explanation for the relatively high rate of subsidence is that many observation points adjacent to Humboldt Bay reported in

Patton (2017 and 2023) are located on sites underlain by soft sediments. Compaction of these soft sediments may exacerbate the relative subsidence rate as observed in Blackwell et al. (2020) who used multitemporal interferometric synthetic aperture radar (InSAR) analysis of large datasets.

Near Buhne Point, Patton et al.(2017, 2023) suggest that Humboldt Bay is interseismically subsiding at a rate ranging from -1.82 mm/yr (-0.07 in/yr) to -2.66 mm/yr (-0.1 in/yr) along HWY 101 to the immediate north and south of Buhne Point, respectively (Figure 9). These values differ slightly from those used by Lettis and Thompson (2020) who used a value of -2mm/yr (-0.08 in/yr) and likely reflect small refinements in those estimates.

The accepted subduction zone interseismic and coseismic model first proposed by Plafker (1972) following the 1960 M9.5 Chile and 1964 M9.2 Alaska earthquakes and Atwater (1987) following investigations of coastal Cascadia that suggests that portions of the coast that are interseismically subsiding will subsequently coseismically uplift (Figure 7 inset). However, the current interseismic subsidence signal for all parts of Humboldt Bay (Patton et al., 2017, 2023a) is in conflict with evidence for substantial coseismic subsidence for at least the last four CSZ earthquakes within parts of both southern and northern Humboldt Bay (Witter et al., 2001; Patton, 2004; Padgett et al., 2021, 2022). Pre-seismic subsidence has been documented for the 1964 and earlier earthquakes in the Upper Cook Inlet region of Alaska (Zong et al., 2003; Shennan and Hamilton, 2006), that is, the area that was slowly subsiding prior to the 1964 M9.2 earthquake also dropped >2 m within minutes during the mainshock event.

It is possible that interseismic and coseismic strain on the adjacent crustal faults (Table Bluff, Little Salmon and Fickle Hill) are also being manifest in the permanent strain record, thus making a prediction of the direction, up or down, of coseismic land level change that may occur when the megathrust ruptures next uncertain.

5 Vertical Land Motion uncertainty complications at Humboldt Bay

Patton et al. (2023) suggest that complications in resolving VLM around Humboldt Bay are not only due to the interseismic loading along the Cascadia subduction megathrust but also the local crustal faults. A large part of the uncertainty is due to the presence of the fold and thrust belt structures located within the accretionary prism that transect the onland and near offshore part of the coast at Humboldt Bay. As described earlier, there is paleoseismic evidence that coseismic events on the Little Salmon fault are accompanied by upper plate folding that may include uplift directly above the fault and subsidence on either side (Witter et al., 2001). This is a smaller scale deformation than one would expect along the Cascadia megathrust but over time results a significant geomorphic feature (i.e., Arcata Bay is largely a syncline formed with the lower plate footwall of the Fickle Hill fault with the hanging wall represented by uplifted terraces at Arcata. It bears repeating that some of the interseismic subsidence signal may be due to soft sediment compaction (for example, Blackwell et al., 2020), especially adjacent to Humboldt Bay,

6 Sea Level Rise

Important to the discussion of potential tsunami inundation and VLM is future sea level rise (SLR) and the rates of sea level change. Page and Nishenko (2015) and Lettis and Thompson (2020) addressed future sea level using global and regional estimates of sea level rise. The estimates are reevaluated periodically and thus it is relevant to revisit new values during this review. Page and Nishenko (2015)

used the guidance of (National Research Council, 2012) to estimate a minimum and maximum SLR by 2115 of 0.1 m (0.3 ft) and 1.4 m (4.7 ft), respectively (Table 2). This would project to 100 years in the future for the facility. Lettis and Thompson (2020) used estimates by IPCC (2019) to estimate a 100 year minimum and maximum SLR in 2120 of 0.3 (1 ft) and 1.5 m (5 ft), respectively (Table 1).

Since those two reports there have been several updates (see Table 2) including (Horton et al., 2020; Sweet et al., 2022; IPCC, 2022; Ocean Protection Council, 2024). The minimum values projected to year 2100 for these later estimates include a low range of 0.2 to 0.4 m (0.7 to 1.4 ft) and a high range of 0.9 to 2.0 m (2.8 to 6.6 ft). Projections as far as 2150 (Sea-level Rise Leadership Team and Ocean Protection Council, 2022; Sweet et al., 2022) provide minimum SLR estimates of 0.3 to 0.4 m (1 to 1.3 ft) and maximum SLR estimates of 3.3 to 3.6 m (10.8 to 11.9 ft).

These projected SLR's, for 2100 and 2150 years, at their minimum values, differ from Page and Nishenko (2015) and Lettis and Thompson (2020) by less than about 0.1 m (0.3 ft) to 0.4 m (1.3 ft) respectively. The maximum values projected to 2100 and 2150 years differ from Page and Nishenko (2015) and Lettis and Thompson (2020) by -0.5m (1.6 ft) (for IPCC, 2022) to 0.6 m (2 ft) (for SLRT&OPC, 2024) for 2100 and 1.9 m (6.2 ft) to 2.2 m (7.2 ft) for 2150.

Thus, there are small differences in the minimum projected SLR estimates since the most recent evaluation was made for Buhne Hill in 2020. The maximum range of projected SLR is more significant for projections to 2100 and 2150 years.

7 Rate of Sea Level Rise

Page and Nishenko (2015) and Lettis and Thompson (2020) also considered rates of sea level rise (Table 3). Also included in the table is an early estimate of SLR rate (Burgette et al., 2009) ranging from 2.0 mm/yr (0.08in/yr) to 2.54 mm/yr (0.1 in/yr) that was considered for local conditions.

For comparison to more recent SLR estimates, Page and Nishenko (2015) reported a rate of 4.06 mm/yr (0.16 in/yr). Lettis and Thompson (2020) used a rate ranging from 8 mm/yr (0.3 in/yr) to 15 mm/yr (0.6 in/yr) 4.06 mm/yr (0.16 in/yr).

He et al. (2022) evaluated sea level rise from Southern California to Vancouver Island. They estimated an average rise rate for the entire coast ranging from 1.5 mm/yr (0.06 in/yr) to 1.78 mm/yr (0.07 in/yr).

Patton et al. (2023) based their rate on Montillet (2018) for a range of 1.8 mm/yr (0.07 in/yr) and 2.08 mm/yr (0.08 in/yr).

The Ocean Protection Council (2024) proposed minimum, intermediate and maximum sea level rise rates for projected year 2100 of 2.5 mm/yr (0.1 in/yr), 20.3 mm/yr (0.8 in/yr) and 33 mm/yr (1.3 in/yr).

8 Impact of sea level rise estimates on tsunami runup estimates

Future considerations of tsunami hazards, including Probabilistic Tsunami Hazard Assessments (PTHA) may have to consider SLR. Lettis and Thompson (2020) described this possibility when they projected a 100 year RSL change in elevation of Buhne Hill that included sea level rise along with interseismic and coseismic vertical land motion.

Recent Probabilistic Tsunami Hazard Assessments (PTHA) typically do not include SLR in their models (González et al., 2009; Selva et al., 2016; De Risi and Goda, 2016; Park et al., 2017; Davies et al., 2018;

Small and Melgar, 2021; Goda, 2023) and only recently has it become a consideration (Li et al., 2018; Nagai et al., 2020; Sepúlveda et al., 2021; Alhamdi et al., 2022).

Nagai et al (2020) used multiple sea level rise scenarios based on accepted curves to investigate potential tsunami inundation for Tokyo Bay, Japan. They concluded that tsunami hazards will not become sensitive to SLR until it reaches about 1 m above current levels at which time the depth and velocity of tsunami waves will "substantially rise." Based on the IPCC curves available at the time of their research they assumed that 2100 water levels could be 0.26 to .92 m higher than the time of publication. So, using the higher SLR projection in 2100 sea level may become important in the hazard.

Li et al. (2018) constructed a PTHA for Macau in the South China Sea. They concluded that SLR increases of 0.5 m (by 2060) and 1 m (by 2100) would dramatically increase the frequency of tsunami-induced hazard by a factor of 1.2 to 2.4 and 1.5 to 4.7, respectively. Their analysis only considers mean high water (MHW).

Sepúlveda et al. (2021) argue that tsunami assessments are complicated by SLR which they refer to as non-stationary conditions because they are always changing. They propose a variant of the PTHA that includes SLR as a nPTHA (non-stationary probabilistic tsunami hazard assessment). They propose that not all PTHA's have to include SLR, especially in cases where tsunami wave heights are not significantly greater than the accumulated SLR amount or the frequency is short enough that little SLR change has occurred.

Thus, a Buhne Hill tsunami runup analysis, may involve projection of SLR to 2100 or greater, and consideration of the recurrence and lapsed time (since 1700 C.E.) of a M>8.0 earthquakes along the CSZ.

FIGURES

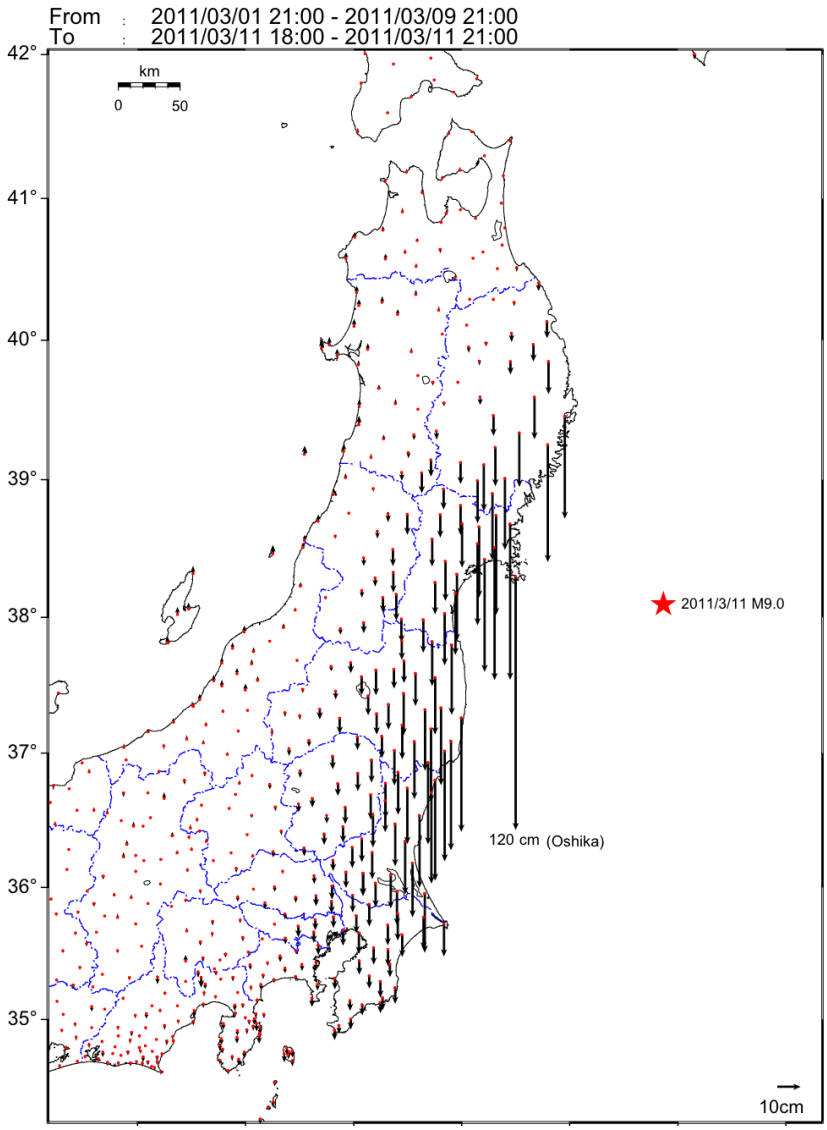

Figure 1 - Vertical crustal deformation associated with the 2011 M 9.2 earthquake (red star) off the Pacific Coast of Japan. Displacement vectors increase at stations closest to the megathrust and epicenter ( ).

(Jacoby Creek marsh)

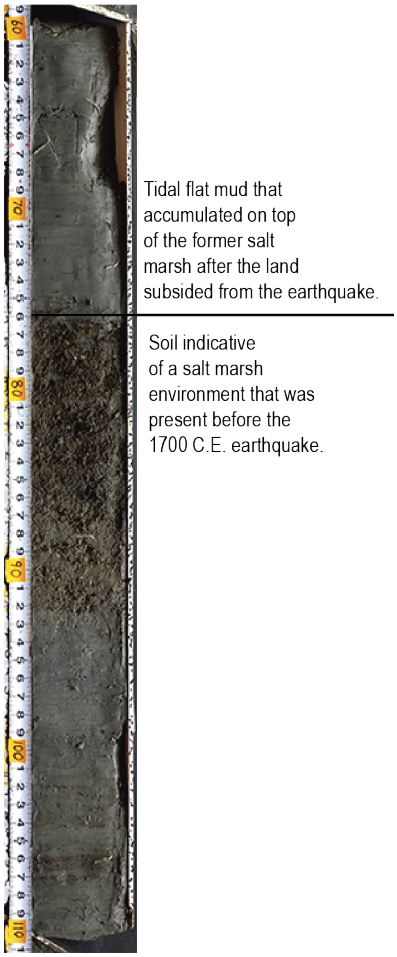

Figure 2 - Photo of a core collected from Jacoby Creek marsh at the edge North Bay (Arcata Bay). The stratigraphy shows the remains of a marsh soil that was buried by tidal flat mud through coseismic subsidence following the CSZ earthquake in 1700 CE (Photo and interpretation by Eileen Hemphill-Haley).

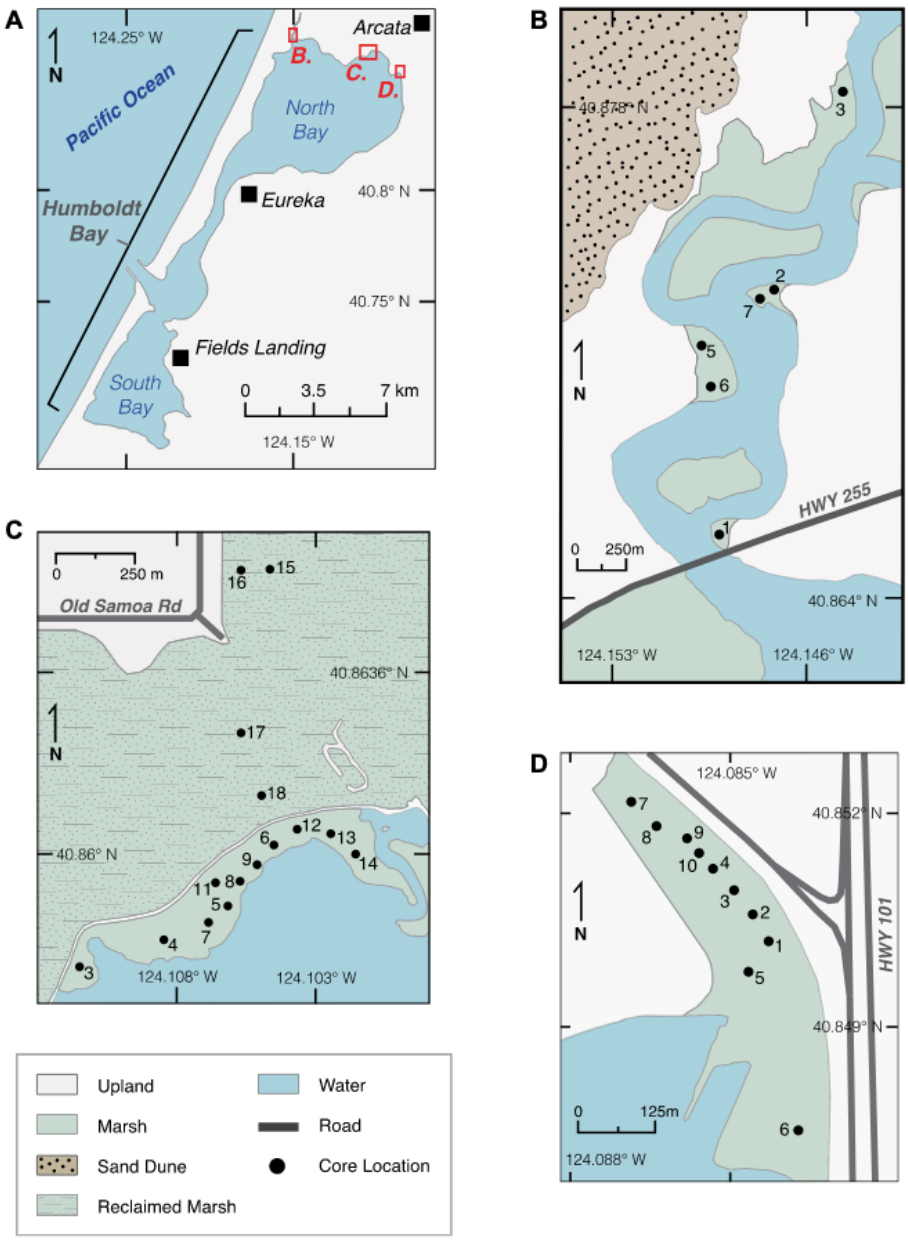

Figure 3 – Locations of marsh borings on the margin of North Bay (from Padgett et al. (2021, their Figure 2).

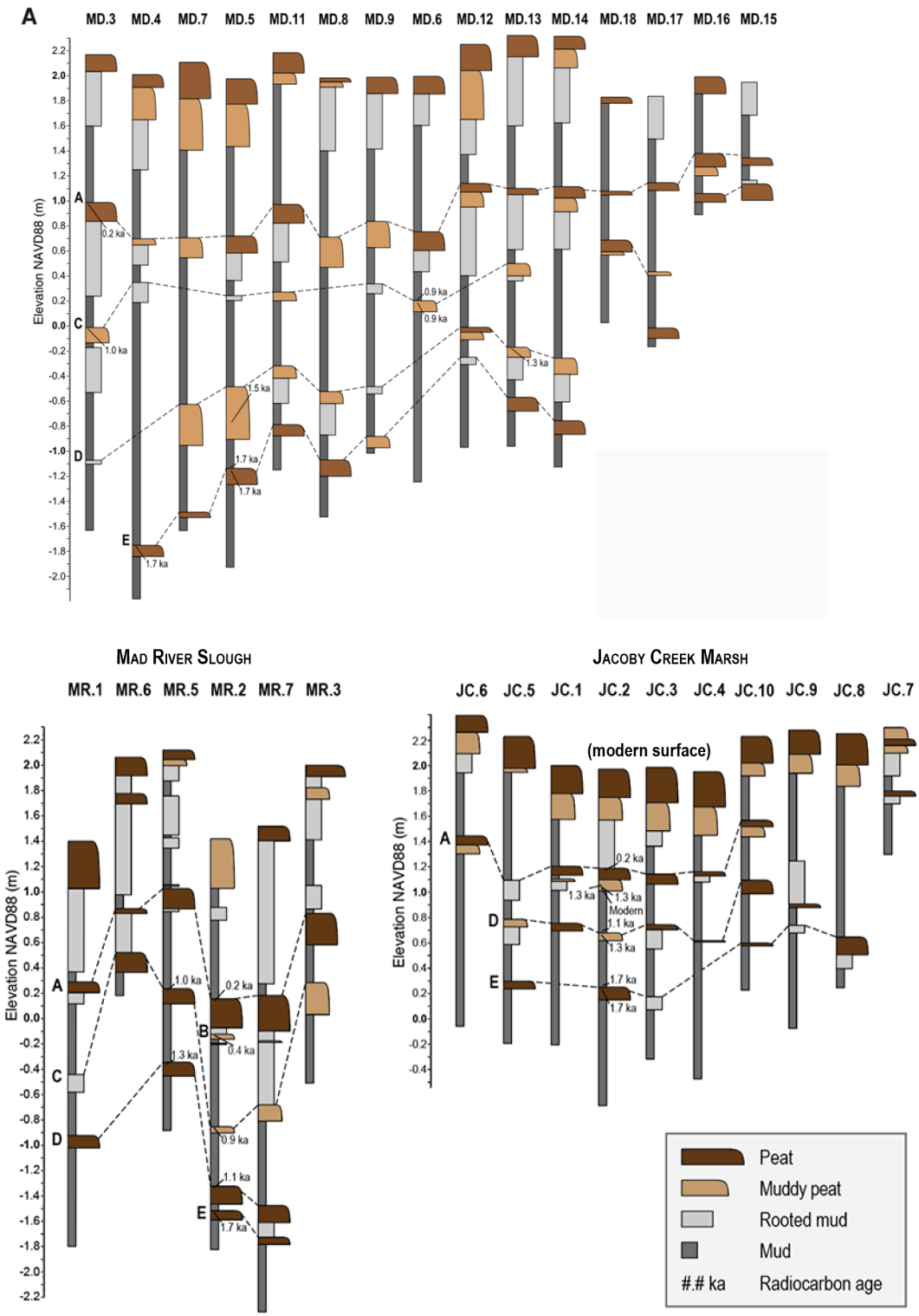

Figure 4 - Core diagrams al. (from Padgett et 2021, 2022) showing multiple times in the past that areas of northern Humboldt Bay coseismically subsided and former marshes (indicated by the dark brown "peat" symbols) were buried by thick accumulations intertidal mud (indicated by gray symbols). Following subsidence, the land builds back up over time to an elevation high enough to support marsh growth again, until the next great earthquake and subsequent burial.

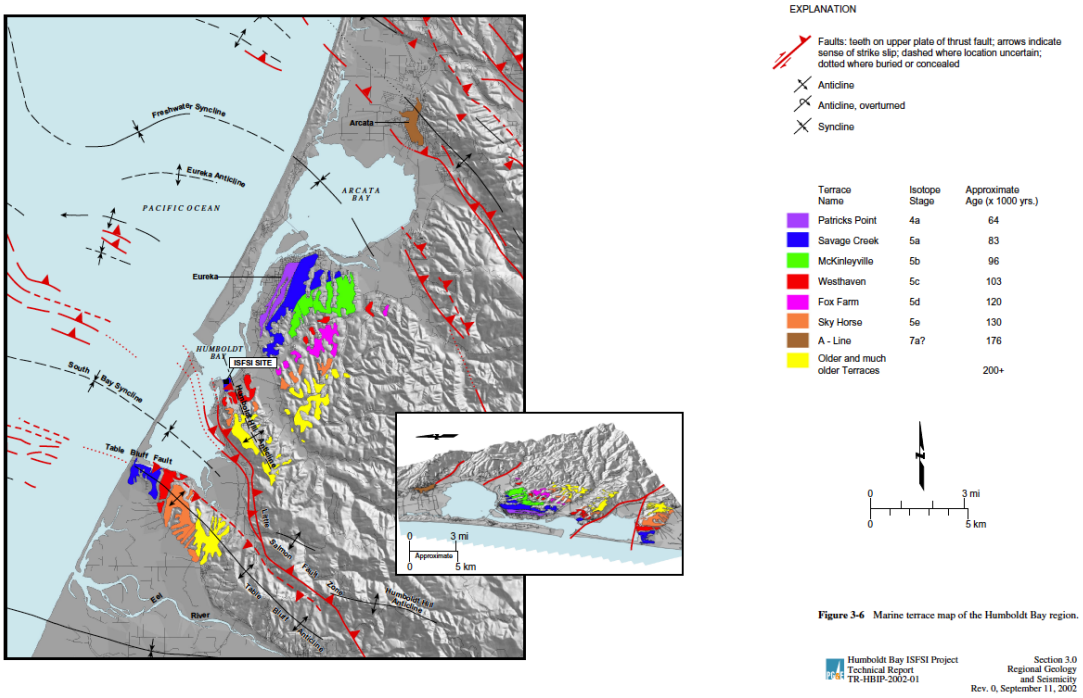

Figure 5 - Marine terrace sequence within Humboldt Bay, CA. Note that the terraces record progressive uplift of anticlinal folds as they grow, presumably coseismically, above thrust faults, including the Table Bluff fault, Little Salmon fault, and an unnamed structure beneath Eureka. Marine terrace geomorphology is absent from intervening synclines. (From Swan et al., 2002, his Figure 3-6).

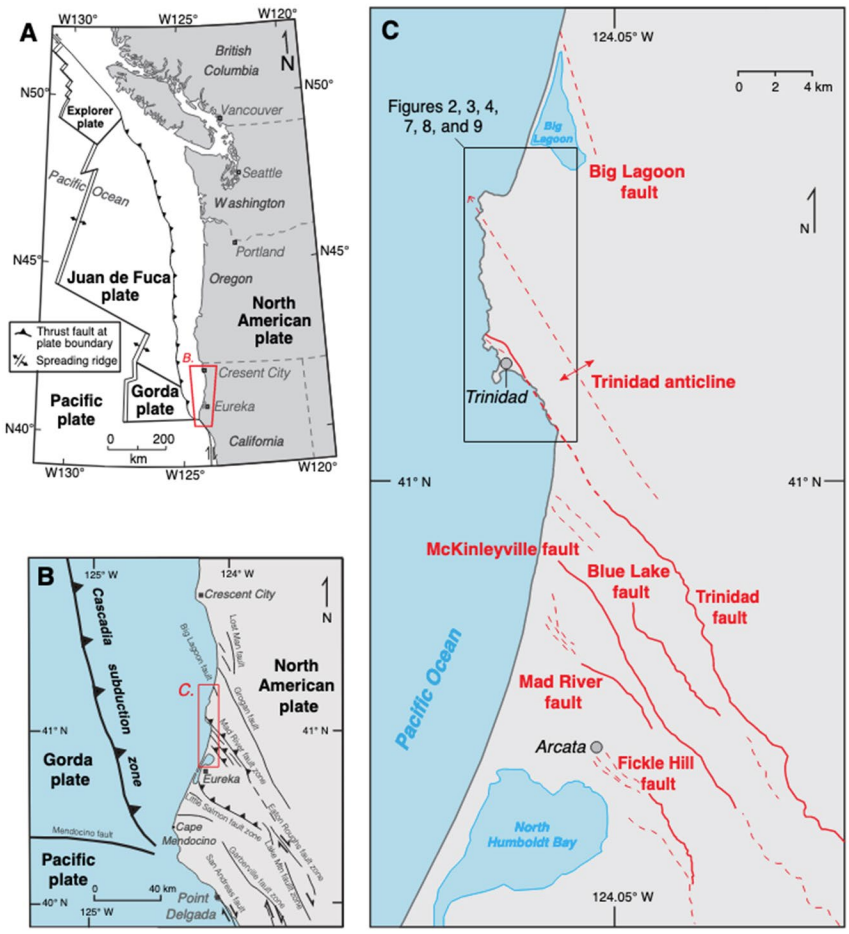

Figure 6 – Configuration of A. fold and thrust belt faults at the southernmost end of the Cascadia subduction zone (from Padgett et al., 2019). B. Location of the Mad River fault zone, within the fold and thrust belt, consisting of five strands; the Trinidad fault is the northernmost. C. Enlarged section of the Mad River fault zone. All bolded lines represent southeast-vergent thrust faults dipping to the northeast. Also, notable is the Trinidad anticline formed in the hanging wall of the thrust fault. All

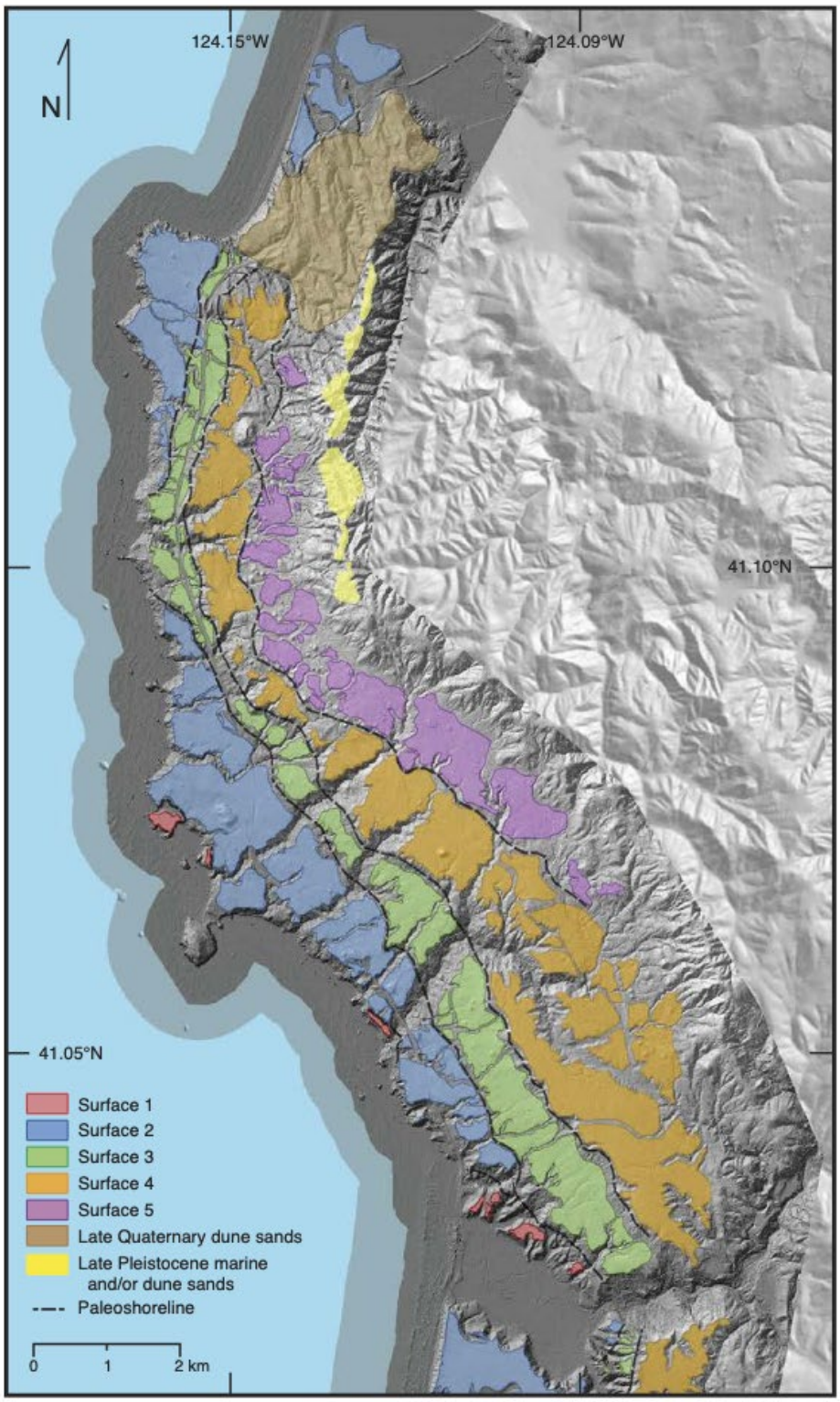

Figure 7 – Mapped marine terrace surfaces (denoted 1, 2, 3, 4 and 5) near Trinidad, CA. Paleoshorelines (terrace back edges) are delineated as black dashed lines (from Padgett et al. (2019, their Figure 7).

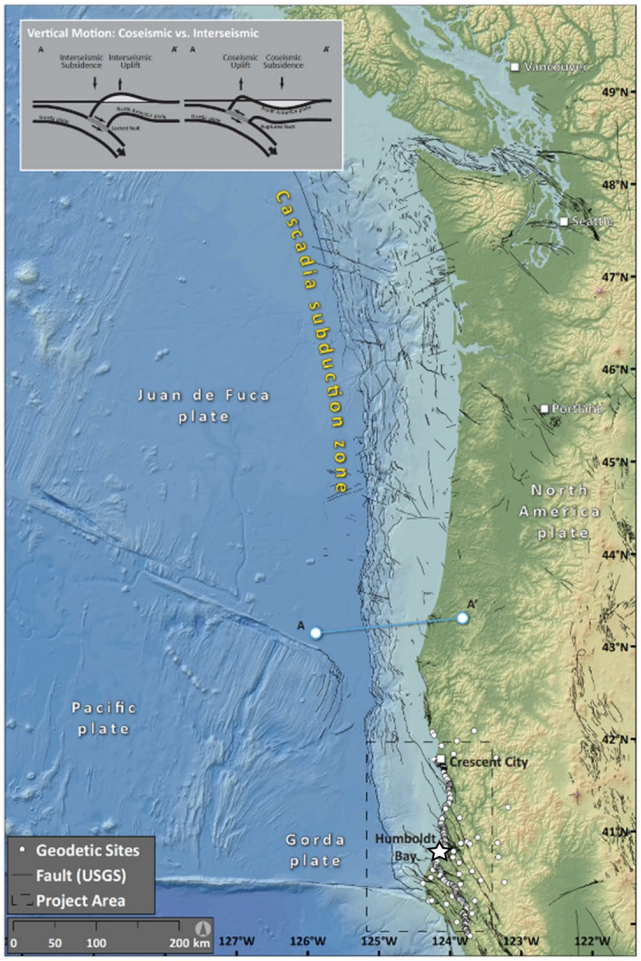

Figure 8 - Map showing locations of faults, geodetic sites and profile (A-A') across the Cascadia subduction zone megathrust and overlying accretionary prism. Inset image depicts interseismic and coseismic deformation across a typical section of the accretionary prism directly above the locked megathrust interface is pulled downward along with the subducting oceanic plate. At the same time, the portion of the accretionary prism immediately landward is bowed upward causing local uplift. Typically, the subsiding part of the accretionary prism is submerged, however, in the Humboldt Bay region, this portion of the upper plate is partially onland which accounts for some of the complexity of the uplift signal. Also note the position of Crescent City relative to Humboldt Bay. Crescent City, located almost twice the distance from the megathrust than Humboldt Bay is experiencing interseismic uplift, Humboldt Bay is experiencing subsidence (From Patton et al., 2023).

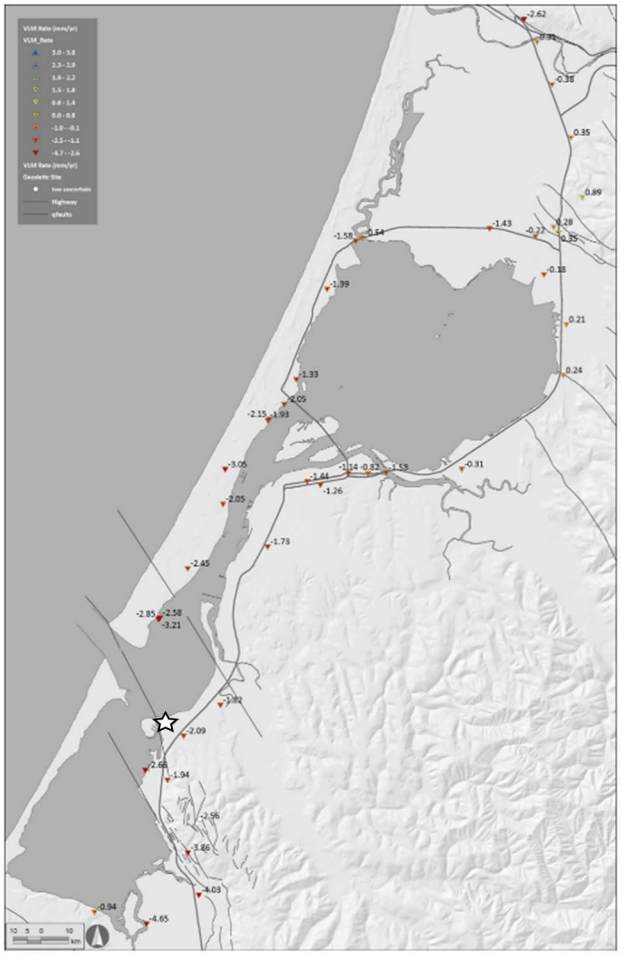

Figure 9 -Vertical Land Motion (VLM) for the Humboldt Bay area (modified from Patton, 2024). Interseismic VLM estimates are based on GNSS Geodetic data and first-order level-line surveys and tide-gauge data. Downward pointing triangles denote subsiding areas while upward-pointing triangles indicate uplift. Triangles are color-coded to indicate ranges of rates. Highest rates of subsidence occur along margin of Humboldt Bay (red to orange colors). They are largely bound on the north by the Mad River fault zone (top of figure) and by the Little Salmon fault zone to the south (at Buhne Hill – white star). Figure 10 provides a profile of interseismic VLM along the same area as this figure.

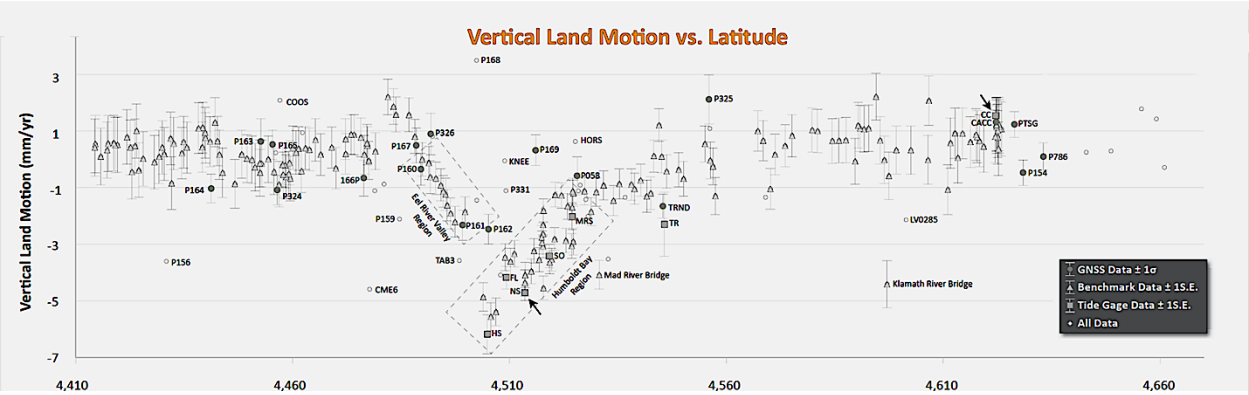

Figure 10 - Plot of vertical land motion (VLM) versus latitude inland of the Cascadia subduction zone (from Patton et al., 2023). Black arrows point to the locations of North Spit (NS) and Crescent City (CC). North Spit is closer to the megathrust and also within the zone of crustal faults such as the Little Salmon and Mad River fault zones. Note the significant negative vertical motion within Humboldt Bay relative to CC.

TABLES

Age of earthquake (youngest at top)	Estimate of coseismic subsidence
250 cal yr BP (1700 CE)	**Average**: 0.6 ± 0.1 m 2 ± 0.3 ft **Range**: 0.2 ± 0.3 to 1.0 ± 0.4 m 0.7 ± 1 to 3 ± 1.3 ft
ca. 875 cal yr BP	**Average**: 0.4 ± 0.2 m 1.3 ± 0.7 ft **Range**: 0.4 ± 0.4 to 0.5 ± 0.4 m 1.3 ± 1.3 to 1.6 ± 1.3 ft
ca. 1120 cal yr BP	**Average**: 0.7 ± 0.2 m 2.6 ± 0.7 ft **Range**: 0.5 ± 0.4 to 0.8 ± 0.5 m 1.6 ± 1.3 to 2.6 ± 1.6 fy
ca. 1620 cal yr BP*	> 0.9m 3 ft

Table 1 – Coseismic subsidence estimates combined from three sites in northern Humboldt Bay (Padgett et al., 2021, 2022). The averages and ranges of ages are from Padgett et al. (2022) with the exception of the ca. 1620 cal yr BP event which is from Padgett et al. (2021).

SLR	Min (ft)	Min (m)	Intermediate (ft)	Intermediate (m)	High (ft)	High (m)
Page and Nishenko (2015) 2115 projection	0.3	0.1			4.7	1.4
Lettis (2020) using IPCC (2019) 2120 projection	1	0.3			5.0	1.5
ICPP (2022) 2100 projection	1.4 (RCP2.6)	0.4			2.8 (RCP8.5)	0.9
Horton et al. (2020) 2100 projection	0.98 (RCP2.6)	0.3			4.26 (RCP8.5)	1.3
Sweet et al. (2022) 2100 Projection 2150 Projection	0.7 1.0	0.2 0.3	2.6 5.2	0.8 1.6	5.9 10.8	1.8 3.3
OPC (2024) 2100 Projection 2120 Projection 2150 Projection	1.0 1.1 1.3	0.3 0.3 0.4	3.1 4.5 6.1	0.9 1.4 1.9	6.6 9.1 11.9	2.0 2.8 3.6

Table 2 – Sea level rise comparison (oldest at the top of table) for several sources. Baseline information from Page and Nishenko (2015) and Lettis and Thompson (2020) are highlighted in gray. Representative Concentration Pathways (RCP) values are accepted low (RCP2.6) and high (RCP8.5) curves.

SLR Rates	Min (in/yr)	Min (mm/yr)	Intermediate (in/yr)	Intermediate (mm/yr)	Max (in/yr)	Max (mm/yr)
Burgette (2009)	0.08	2.0			0.1	2.54
Page and Nishenko (2015)					0.16	4.06
Lettis (2020) using IPCC (2019)	0.3	8			0.6	15
He et al. (2022) GLOBAL	0.06	1.5			0.07	1.78
Patton et al. (2023) using Montillet (2018)	0.07	1.8			0.08	2.03
OPC (2024) 2025 2100	 0.1 0.1	 2.5 2.5	 0.3 0.8	 7.6 20.3	 0.7 1.3	 17.78 33.02

Table 3 – SLR rate comparisons with oldest at top. Baseline information from Page and Nishenko (2015) and Lettis and Thompson (2020) are highlighted in gray.

REFERENCES

Alhamid, A.K., Akiyama, M., Ishibashi, H., Aoki, K., Koshimura, S., and Frangopol, D.M., 2022, Framework for probabilistic tsunami hazard assessment considering the effects of sea-level rise due to climate change: Structural Safety, v. 94, p. 102152, doi:10.1016/j.strusafe.2021.102152.

Atwater, B.F., 1987, Evidence for Great Holocene Earthquakes Along the Outer Coast of Washington State: Science, v. 236, p. 942–944, doi:10.1126/science.236.4804.942.

Atwater, B.F., Tuttle, M.P., Schweig, E.S., Rubin, C.M., Yamaguchi, D.K., and Hemphill-Haley, E., 2003, Earthquake recurrence inferred from paleoseismology, *in* Developments in Quaternary Sciences, Elsevier, v. 1, p. 331–350, doi:10.1016/S1571-0866(03)01015-7.

Blackwell, E., Shirzaei, M., Ojha, C., and Werth, S., 2020, Tracking California's sinking coast from space: Implications for relative sea-level rise: Science Advances, v. 6, p. eaba4551, doi:10.1126/sciadv.aba4551.

Burgette, R.J., Weldon, R.J., and Schmidt, D.A., 2009, Interseismic uplift rates for western Oregon and along-strike variation in locking on the Cascadia subduction zone: Journal of Geophysical Research: Solid Earth, v. 114, p. 2008JB005679, doi:10.1029/2008JB005679.

Burke, R.M., and Carver, G.A., (eds), 1992, A look at the southern end of the Cascadia subduction zone and the Mendocino triple junction: Guidebook for the Pacific Cell Friends of the Pleistocene Field Trip to Coastal Northern California: 256 p.

Carver, G.A., and Plafker, G., 2008, Paleoseismicity and neotectonics of the Aleutian Subduction Zone—An overview, *in* Active Tectonics and Seismic Potential of Alaska, Washington, D.C., American Geophysical Union Geophysical Monograph Series, v. 179, p. 43–63, http://adsabs.harvard.edu/abs/2008GMS...179...43C (accessed June 2020).

Davies, G. et al., 2018, A global probabilistic tsunami hazard assessment from earthquake sources: Geological Society, London, Special Publications, v. 456, p. 219–244, doi:10.1144/SP456.5.

De Risi, R., and Goda, K., 2016, Probabilistic Earthquake–Tsunami Multi-Hazard Analysis: Application to the Tohoku Region, Japan: Frontiers in Built Environment, v. 2, doi:10.3389/fbuil.2016.00025.

Frederikse, T. et al., 2020, The causes of sea-level rise since 1900: Nature, v. 584, p. 393–397, doi:10.1038/s41586-020-2591-3.

Freymueller, J.T., Haeussler, P.J., Wesson, R.L., and Ekström, G., 2013, Active Tectonics and Seismic Potential of Alaska: John Wiley & Sons, 850 p.

Goda, K., 2023, Probabilistic Tsunami Hazard Analysis for Vancouver Island Coast Using Stochastic Rupture Models for the Cascadia Subduction Earthquakes: GeoHazards, v. 4, p. 217–238, doi:10.3390/geohazards4030013.

González, F.I. et al., 2009, Probabilistic tsunami hazard assessment at Seaside, Oregon, for near- and far-field seismic sources: Journal of Geophysical Research: Oceans, v. 114, doi:10.1029/2008JC005132.

He, X., Montillet, J.-P., Fernandes, R., Melbourne, T.I., Jiang, W., and Huang, Z., 2022, Sea Level Rise Estimation on the Pacific Coast from Southern California to Vancouver Island:

Hemphill-Haley, E., 2017, Observations on the distributions of modern benthic diatoms to improve estimates of past coseismic land-level changes, Humboldt Bay, California: Seismological Research Letters, v. 8, https://www.seismosoc.org/wp-content/uploads/2018/09/srl-2017035.1.pdf.

Horton, B.P., Khan, N.S., Cahill, N., Lee, J.S.H., Shaw, T.A., Garner, A.J., Kemp, A.C., Engelhart, S.E., and Rahmstorf, S., 2020, Estimating global mean sea-level rise and its uncertainties by 2100 and 2300 from an expert survey: npj Climate and Atmospheric Science, v. 3, p. 18, doi:10.1038/s41612-020-0121-5.

Hutchinson, I., and Clague, J., 2017, Were they all giants? Perspectives on late Holocene plate-boundary earthquakes at the northern end of the Cascadia subduction zone: Quaternary Science Reviews, v. 169, p. 29–49, doi:10.1016/j.quascirev.2017.05.015.

Hyndman, R.D., and Wang, K., 1995, The rupture zone of Cascadia great earthquakes from current deformation and the thermal regime: Journal of Geophysical Research: Solid Earth, v. 100, p. 22133–22154, doi:10.1029/95JB01970.

Imakiire, T., and Koarai, M., 2012, Wide-area land subsidence caused by "the 2011 Off the Pacific Coast of Tohoku Earthquake": Soils and Foundations, v. 52, p. 842–855, doi:10.1016/j.sandf.2012.11.007.

IPCC, 2019, Summary for Policymakers, In: IPCC Special Report on the Ocean and Cryosphere in a Changing Climate: Intergovernmental Panel on Climate Change.

IPCC, 2022, The Ocean and Cryosphere in a Changing Climate: Special Report of the Intergovernmental Panel on Climate Change: Intergovernmental Panel on Climate Change, doi:10.1017/9781009157964.

Jacoby, G.C., Carver, G.A., and Wagner, W., 1995, Trees and herbs killed by an earthquake ~300 yr ago at Humboldt Bay, California: Geology, v. 23, p. 77–80, doi:10.1130/0091-7613(1995)023<0077:TAHKBA>2.3.CO;2.

Kelsey, H.M., and Carver, G.A., 1988, Late Neogene and Quaternary tectonics associated with northward growth of the San Andreas Transform Fault, northern California: Journal of Geophysical Research: Solid Earth, v. 93, p. 4797–4819, doi:10.1029/JB093iB05p04797.

Lettis, W.R., and Thompson, S.C., 2020, Estimated 100-year Relative Sea-Level Change at Buhne Hill, Humboldt County, California:, 15 p.

Li, W.-H., 1992, Evidence for the late Holocene coseismic subsidence in the Lower Eel River valley, Humboldt county, Northern California: An application of foraminiferal zonation to indicate tectonic submergence [Masters Thesis]: Humboldt State University.

Li, L., Switzer, A.D., Wang, Y., Chan, C.-H., Qiu, Q., and Weiss, R., 2018, A modest 0.5-m rise in sea level will double the tsunami hazard in Macau: Science Advances, v. 4, p. eaat1180, doi:10.1126/sciadv.aat1180.

Nagai, R., Takabatake, T., Esteban, M., Ishii, H., and Shibayama, T., 2020, Tsunami risk hazard in Tokyo Bay: The challenge of future sea level rise: International Journal of Disaster Risk Reduction, v. 45, p. 101321, doi:10.1016/j.ijdrr.2019.101321.

National Research Council, 2012, Sea Level Rise for the Coasts of California, Oregon and Washington: Past Present and Future:, https://nap.nationalacademies.org/resource/13389/sea-level-rise-brief-final.pdf (accessed September 2024).

Nelson, A.R., Kelsey, H.M., and Witter, R.C., 2006, Great earthquakes of variable magnitude at the Cascadia subduction zone: Quaternary Research, v. 65, p. 354–365, doi:10.1016/j.yqres.2006.02.009.

Ocean Protection Council, 2024, California Sea Level Rise Guidance: 2024 Science and Policy Update: , p. 101.

Ogle, B.A., 1953, Geology of the Eel River Basin, Humboldt County, California: California Division of Mines Bulletin 164, 128 p., http://archives.datapages.com/data/bulletns/1953-56/data/pg/0037/0012/2750/2777.htm (accessed February 2020).

Padgett, J., 2019, CASCADIA SUBDUCTION ZONE COSEISMIC SUBSIDENCE ESTIMATES FROM NORTHERN CALIFORNIA AND WASHINGTON: University of Rhode Island, doi:10.23860/diss-padgett-jason-2019.

Padgett, J.S., Engelhart, S.E., Kelsey, H.M., Witter, R.C., and Cahill, N., 2022, Reproducibility and variability of earthquake subsidence estimates from saltmarshes of a Cascadia estuary: Journal of Quaternary Science, v. 37, p. 1294–1312, doi:10.1002/jqs.3446.

Padgett, J.S., Engelhart, S.E., Kelsey, H.M., Witter, R.C., Cahill, N., and Hemphill-Haley, E., 2021, Timing and amount of southern Cascadia earthquake subsidence over the past 1700 years at northern Humboldt Bay, California, USA: GSA Bulletin, v. 133, p. 2137–2156, doi:10.1130/B35701.1.

Padgett et al. - 2021 - Timing and amount of southern Cascadia earthquake .pdf.

Padgett et al. - 2022 - Reproducibility and variability of earthquake subs.pdf.

Padgett, J.S., Kelsey, H.M., and Lamphear, D., 2019, Upper-plate deformation of Late Pleistocene marine terraces in the Trinidad, California, coastal area, southern Cascadia subduction zone: Geosphere, v. 15, p. 1323–1341, doi:10.1130/GES02032.1.

Page, W.D., and Nishenko, S., 2015, Assessment of Potential Tsunami Runup at the Humboldt Bay Generating Station Site: PG&E Internal, 89 p.

Park, H., Cox, D.T., Alam, M.S., and Barbosa, A.R., 2017, Probabilistic Seismic and Tsunami Hazard Analysis Conditioned on a Megathrust Rupture of the Cascadia Subduction Zone: Frontiers in Built Environment, v. 3, doi:10.3389/fbuil.2017.00032.

Patton, J.R., 2004, Late Holocene coseismic subsidence and coincident tsunamis, southern Cascadia subduction zone, Hookton Slough, Wigi (Humboldt Bay), California: Humboldt State University, 76 p.

Patton, J.R., Williams, T.B., Anderson, J., and Heaton, T.H., 2017, Tectonic land level changes and their contribution to sea-level rise, Humboldt Bay region, Northern California: U.S. Fish and Wildlife Service Final Technical Report F11AC01092, 47 p.

Patton, J., Williams, T., Anderson, J., Hemphill-Haley, M., Burgette, R., Weldon Ii, R., McPherson, R., and Leroy, T., 2023a, 20th to 21st Century Relative Sea and Land Level Changes in Northern California:Tectonic Land Level Changes and their Contribution to Sea-Level Rise, Humboldt Bay Region, Northern California: Tektonika, v. 1, doi:10.55575/tektonika2023.1.1.6.

Patton, J., Williams, T., Anderson, J., Hemphill-Haley, M., Burgette, R., Weldon Ii, R., McPherson, R., and Leroy, T., 2023b, 20th to 21st Century Relative Sea and Land Level Changes in Northern California:Tectonic Land Level Changes and their Contribution to Sea-Level Rise, Humboldt Bay Region, Northern California: Tektonika, v. 1, p. 17, doi:10.55575/tektonika2023.1.1.6.

Plafker, G., 1972, Alaskan earthquake of 1964 and Chilean earthquake of 1960: Implications for arc tectonics: Journal of Geophysical Research (1896-1977), v. 77, p. 901–925, doi:10.1029/JB077i005p00901.

Plafker, G., 1969, Tectonics of the March 27, 1964 Alaska Earthquake, *in* Washington, D.C., U.S. Geological Survey Professional Paper 543-I, p. 74, https://pubs.usgs.gov/pp/0543i/ (accessed June 2020).

Pritchard, C.J., 2004, Late Holocene relative sea-level changes, Arcata Bay, California : evaluation of freshwater syncline movement using coseismically buried soil horizons [Masters Thesis]: Humboldt State University, 63 p., http://dspace.calstate.edu/handle/2148/883 (accessed May 2020).

Savage, J.C., Lisowski, M., and Prescott, W.H., 1991, Strain accumulation in western Washington: Journal of Geophysical Research: Solid Earth, v. 96, p. 14493–14507, doi:10.1029/91JB01274.

Sea-level Rise Leadership Team and Ocean Protection Council, 2022, State Agency Sea-Level Rise Action Plan for California: State and Federal Reports and Publications, 28 p.

Selva, J., Tonini, R., Molinari, I., Tiberti, M.M., Romano, F., Grezio, A., Melini, D., Piatanesi, A., Basili, R., and Lorito, S., 2016, Quantification of source uncertainties in Seismic Probabilistic Tsunami Hazard Analysis (SPTHA): Geophysical Journal International, v. 205, p. 1780–1803, doi:10.1093/gji/ggw107.

Sepúlveda, I., Haase, J.S., Liu, P.L. -F., Grigoriu, M., and Winckler, P., 2021, Non-Stationary Probabilistic Tsunami Hazard Assessments Incorporating Climate-Change-Driven Sea Level Rise: Earth's Future, v. 9, p. e2021EF002007, doi:10.1029/2021EF002007.

Shennan, I., Barlow, N., Carver, G., Davies, F., Garrett, E., and Hocking, E., 2014, Great tsunamigenic earthquakes during the past 1000 yr on the Alaska megathrust: Geology, v. 42, p. 687–690, doi:10.1130/G35797.1.

Shennan, I., and Hamilton, S., 2006, Coseismic and pre-seismic subsidence associated with great earthquakes in Alaska: Quaternary Science Reviews, v. 25, p. 1–8, doi:10.1016/j.quascirev.2005.09.002.

Small, D.T., and Melgar, D., 2021, Geodetic Coupling Models as Constraints on Stochastic Earthquake Ruptures: An Example Application to PTHA in Cascadia: Journal of Geophysical Research: Solid Earth, v. 126, p. e2020JB021149, doi:10.1029/2020JB021149.

Stanton, K.M., Crider, J.G., Kelsey, H.M., and Feathers, J.K., 2024, The signature of accumulated permanent uplift, northern Cascadia subduction zone: Quaternary Research, v. 117, p. 98–118, doi:10.1017/qua.2023.59.

Swan, F.H., Carver, G.A., McLaren, M., and Page, W.D., 2002, Seismic Hazard Assessment for the Humboldt Bay ISFSI Project: Regional Geology and Seismology: Pacific Gas and Electric Company Technical Report TR-HBIP-2002-01, Section 3, 83 p.

Sweet, W.V. et al., 2022, Global and Regional Sea Level Rise Scenarios for the United States: updated Mean Projections and Extreme Water Level Probabilities Along U.S. Coastlines: NOAA Technical Report NOS 01, 111 p., https://oceanservice.noaa.gov/hazards/sealevelrise/noaa-nos-techrpt01-global-regional-SLR-scenarios-US.pdf.

Vadurro, G.A., 2006, Amount and rate of deformation across the Little Salmon fault and Table Bluff anticline within the onland portion of the Southern Cascadia Subduction Zone fold and thrust belt, NW California, *in* Signatures of Quaternary crustal deformation and landscape evolution in the Mendocino deformation zone, NW California, M. Hemphill-Haley, T. Leroy, B. McPherson, J. Patton, J. Stallman, D. Sutherland and T. Williams, Friends of the Pleistocene eds., Pacific Cell, p. 113–120.

Valentine, D.W., 1992, Late Holocene Stratigraphy, Humboldt Bay, California: Evidence for Late Holocene Paleoseismicity of the Southern Cascadia Subduction Zone [Masters Thesis]: Humboldt State University, https://escholarship.org/uc/item/7328g533 (accessed May 2020).

Valentine, D.W., Keller, E.A., Carver, G., Li, W.-H., Manhart, C., and Simms, A.R., 2012, Paleoseismicity of the Southern End of the Cascadia Subduction Zone, Northwestern California: Bulletin of the Seismological Society of America, v. 102, p. 1059–1078, doi:10.1785/0120110103.

Vick, G., 1988, Late Holocene Paleoseismicity and relative vertical crustal movements [Masters Thesis]: Humboldt State University, 96 p.

Walsh, T.J., Combellick, R.A., and Black, G.L., 1995, Liquefaction Features from a Subduction Zone Earthquake:Preserved Examples from the 1964 Alaska Earthquake: Washington State Department of Natural Resources, Division of Geology and Earth Resources Report Investigations 32, 90 p.

Wang, K., and Tréhu, A.M., 2016, Invited review paper: Some outstanding issues in the study of great megathrust earthquakes—The Cascadia example: Journal of Geodynamics, v. 98, p. 1–18, doi:10.1016/j.jog.2016.03.010.

Wang, K., Wells, R.E., Mazzotti, S., Hyndman, R.D., and Sagiya, T., 2003, A revised dislocation model of interseismic deformation of the Cascadia subduction zone: Journal of Geophysical Research B: Solid Earth, v. 108, doi:10.1029/2001JB001227.

Witter, R.C., Patton, J.R., Carver, G.A., Kelsey, H.M., Garrison, C., Koehler, R.D., and Hemphill-Haley, E., 2001, Upper-plate earthquakes on the western Little Salmon fault and contemporaneous

subsidence of southern Humboldt Bay over the past 3,600 years, northwestern California: U.S. Geological Survey, National Earthquake Hazards Reduction Program (NEHRP) Final Technical Report 01HQGR0125, 47 p.

Woodward-Clyde Consultants, 1980, Evaluation of the potential for resolving the geologic and seismic issues at the HBPP Unit No. 3: Summary to Pacific Gas and Electric company, San Francisco, CA:, 74, plus appendix p.

Zong, Y., Shennan, I., Combellick, R.A., Hamilton, S.L., and Rutherford, M.M., 2003, Microfossil evidence for land movements associated with the AD 1964 Alaska earthquake: The Holocene, v. 13, p. 7–20, doi:10.1191/0959683603hl590rp.

APPENDIX C

1 Segmentation, Recurrence and Wedge Fault Structural Models for Cascadia

There has been significant effort since Page and Nishenko (2015) to better characterize the Cascadia Subduction Zone (CSZ). Wang and Tréhu (2016) provided some guidance as to outstanding issues about the seismogenic and tsunamigenic properties of the subduction zone. A paramount question has been "does the Cascadia subduction zone" only have full-length ruptures?

Additional questions include:

- Are there along-strike variations in slip behavior? Is there segmentation of the subduction zone resulting in M<9 earthquakes?
- What is the downdip limit of the seismogenic subduction zone? Does it coincide with the top of Episodic Tremor and Slip zones?
- Is coseismic slip confined to the shallow megathrust and does not involve secondary faulting?
- If secondary faulting is involved in coseismic slip what are the models of fault tips in the accretionary wedge?
- Additionally, models of segmentation and fault architecture bring to question their impacts on tsunami generation.

1.1 Segmentation and Magnitude

Wang and Tréhu (2016) suggested there are areas of adjacent low- and high-slip along the subduction zone that may also coincide with Episodic Tremor and Slip (ETS) segments (Figure 1) first proposed by Brudzinski and Allen (2007)

Recently, four significant papers report on the offshore morphological character of the CSZ accretionary wedge, the downgoing oceanic plate and evidence for possible physical and seismogenic segmentation of the subduction zone.
Watt and Brothers (2020) identified four distinct regions based on outer wedge width and steepness along with patterns of structural vergence and wedge shape (Figures 2 and 3). They are (Figure 2C) **Vancouver Island** (average width, linear wedge, seaward and mixed vergence); **Washington** (higher width, concave wedge, landward and mixed vergence); **north and central Oregon** (average width, linear and convex wedge, mixed and seaward vergence); and **southern Oregon and northern California** (lower width, convex wedge, seaward and mixed vergence).

Watt and Brothers (2020) posit that the differences in the outer wedge morphology are associated with along-strike megathrust segmentation also defined by differences in oceanic asthenospheric velocities, episodic tremor and slip occurrences, plate locking models and seismicity around the boundaries. They also propose that variations in morphotectonics may be related to differences in wedge strength, megathrust friction (possibly due to roughness of downgoing slab, and slip behavior.

Hill et al. (2020) conducted bathymetric and seismic reflection analysis of the CSZ margin from Oregon to Cape Mendocino primarily to evaluate offshore landsliding (Figures 4, 5 and 6). They provide high resolution images of the accretionary wedge in the vicinity of the subducting Gorda plate and in the vicinity of Humboldt Bay. Landslides are important in that they can be tsunamigenic and also they have been used as indicators of strong shaking during large earthquakes (, Goldfinger et al., 2012, 2013). One observation was that there appears to be fewer slope failure features along this portion of the subduction zone relative to areas to the north. They suggest it is due to rapid sediment accumulation masking geomorphic features and that significant sediment loading also causes overpressurization of the sediments

causing them to fluidize. They indicate that although there is significant sediment accumulation most of the wedge area is devoid of landslides despite numerous earthquake events. They postulate that repeated earthquake events may result in seismic strengthening whereby sediments become more consolidated and less prone to failure. Finally, they concluded that the conditions for canyon-confined seismoturbidite generation proposed by Goldfinger elsewhere because the “tectonically influenced margin physiography that inhibits sediment bypass from the shelf to the deep sea.” are absent in this part of Cascadia because the shortening and uplift at the north and south margins of the Gorda plate have created steep and deeply incised channels that induce sediment bypass, thus most of the canyon systems receive little to no fluvial sediment and are not conducive to shelf to abyss sedimentation that produces substantial turbidite records. Instead it appears that much of the sedimentation near the trench may be due to slope failures of the steep outer edge of the accretionary wedge. If this is the case, to the north it may impact the paleoturbidite interpretation for large magnitude events.

Walton et al. (2021) provide a summary of findings to characterize Cascadia. They provide evidence for differences in properties along strike within the subduction margin, both in the upper and lower plates (and plate interface) that support heterogeneity in the subduction zone (Figure 7). They note that some of these differences in the incoming plate include temporal and physical changes in episodic tremor and slip (ETS), presence of seamounts and minor associated seismicity possibly related to subduction of seamounts (Tréhu et al., 2012; Stone et al., 2018). They also prefer a model that the rupture during the 1700 C.E. event was not homogeneous but instead consisted of patches of high slip separated by low slip portions of the megathrust (Figure 8) as proposed by Wang et al. (2013). In the overriding plate, faults within Siletzia terrane may cause fluid conditions that create pressure differentials down to the slab interface (Wells et al., 2003, 2017) and may influence ETS occurrences (for example, Bodmer et al., 2018; Hall et al., 2018; Luo and Liu, 2019; Michel et al., 2019; Bartlow, 2020; Hutchison, 2020; Bombardier et al., 2024). Walton et al. (2021) also suggest, based on interpretations by Watt and Brothers (2020), that Siletzia may serve as a backstop that influences frictional properties in the megathrust possibly causing splay faulting above the décollement. The slow slip portions of the 1700 C.E. earthquake (Figure 7, left map) may be related to the heterogeneity suggested by ETS and Siletzia faults in Figure 8 (Wang et al., 2013; Wells et al., 2017).

Walton et al. (2021) also discuss how the heterogenous nature of the subduction zone may influence rupture length, and, correspondingly magnitude. They describe how persistent rupture barriers (such as described above) may be responsible for more frequent ruptures in southern Cascadia (i.e., M<9 earthquakes) south of Cape Blanco that have also been suggested by others.

More recently Carbotte et al. (2024) review evidence gathered by offshore high-resolution bathymetry and geophysics along the subduction zone from the California/Oregon border to the northern end in Canada. They too find large variability in the oceanic plate that may result in heterogeneity in rupture along the subduction zone (Figure 9). They identify domains of lower plate geometry and sediment underthrusting that had not been previously reported. They also indicate that these low plate domains align with upper plate areas of lithological and structural differences. Additionally, they conclude that differences in upper plate loading of young and weak Juan de Fuca oceanic plate by Franciscan and Siletzia terranes combined with lithified sediments of the inner wedge are, in part, responsible for lower plate geometry variability.

Bodmer et al. (2018) use teleseismic delay time data to image seismic velocities (tomography) of the entire CSZ (Figure 10). Importantly, their imaging shows the high velocity, dense subducting slab is underlain by discontinuous warm and buoyant mantle at between 100 and 300 km depth. They interpret this to affect the coupling stress across the megathrust interface. They describe the “remarkable spatial consistency between segmentation of subslab low-velocity anomalies, plate locking, and tremor density” (Figure 11). This evidence suggests that strong plate locking, caused by buoyant mantle, is occurring in

northern and southern Cascadia and thus may be responsible for rupture segmentation of the subduction zone.

Fan and Zaoh (2021) reviewed the slip histories of six M~9 subduction zones (Figure 12) and, using tomographic imaging, interpreted that low velocity anomalies beneath the subducting slab were locations of mainshock hypocenters for three large subduction zone events (2011 Tohoku-Oki, Japan, 1964 Alaska and 1959 Kamchatka) They also conclude that two other large earthquakes (1960 Chile and 2004 Banda Aceh) initiated at the margins of low velocity zones. Although the hypocenter of the 1700 C.E. Cascadia earthquake is not known they suggest that the two large low velocity zones (Figure 12) (one located at southern Cascadia) may be candidate locations.

Additional research toward the heterogeneity of the subducting slab include Bilek and Lay (2018) who suggest that rough downgoing plate topography, related to seamounts, may serve as rupture barriers and enhance segmentation. Also, upper plate variations in lithology and structure may increase slip variability. Harrichausen et al (2024) conducted numerical modeling to evaluate coupling between the subduction zone and crustal faults in northern Cascadia and concluded that in that location, the upper plate faults are not being driven much by the subducting plate.

McKenzie et al. (2022) used GPS data along the length of Cascadia to better understand the role of upper plate rheology and its connection to locking depth of the subduction zone. They consider the strength of the rigid, basaltic Siletzia terrane throughout most of Oregon and southern Washington compared to northern California and southernmost Oregon where the forearc is largely comprised of accreted rocks including the relatively weak, sheared Franciscan to the west backed, to the east, by relatively rigid Klamath rocks (Figure 13). They show that there are considerably higher horizontal GPS velocities in the Siletzia portion of the subduction zone in Oregon and southern Washington and higher velocities in the Franciscan portion of northern California and southern Oregon (Figure 13 b and c). The western edge of the Siletzia terrane and the accretionary wedge (Figure 13b), is deforming relatively rapidly with velocities that range from ~ 10-15 mm/yr, while the interior of Siletzia at about 200 km from the trench moves considerable slower (5-10 mm/yr). To the south (Figure 13c), the accretionary margin and Franciscan terrane are moving at ~ 10–18 mm/yr and the Klamath terrane has velocities of less than 5 mm/yr. They also report that vertical velocities tend to be greater in the southern portion of the subduction zone. They conclude that Finite Element modeling indicates that the central portion of Cascadia likely does not behave like an elastic homogeneous coupled upper plate and there are various strengths and structures (faults) within Siletzia that likely represent the velocity behavior. They also conclude that the locking portion of the interface likely extends to beneath western Siletzia. To the south, the locking portion of the subduction zone likely is located within the weak Franciscan terrane where vertical and horizontal velocities are high and non-uniform. The Klamath terrane serves as a backstop.

They assume that the locked portion of the subduction zone has remained in its current position over the last 100-1000’s of years and compare magnitude estimates from the model to paleoseismic estimates. In southern Cascadia, from the southernmost end north to ~43°N, they posit that a M8.3-8.4 event with a recurrence interval of 300 years is permissible (consistent with paleoseismic estimates of 220 to 400 years).

1.2 Episodic tremor and slip (ETS) and role in segmentation models

Episodic tremor and slip (ETS) behavior was first identified and described by Dragert et al. (2001) and Rogers and Dragert (2003) along the northern Cascadia margin to explain why permanent GPS stations showed episodes of motion along the upper plate of the subduction zone releasing small amounts of accumulated strain and, simultaneously were associated with small, non-volcanic tremor events. These events tend to have regularly episodic periods of slow-slip, last days and associated tremor located

beneath the seismically-coupled zone, typically in Cascadia at about 30 - 50 km depth (Walton et al., 2021). The ETS zone is typically separated from the seismogenic zone by a steadily creeping gap (Bartlow, 2020). There is no full understanding of why ETS occur but it is thought they may be related to high fluid pressures near the continental mantle beneath the MOHO (Wang and Tréhu, 2016; Gao and Wang, 2017; Walton et al., 2021). Wells et al. (2017) suggest that crustal faults that extend to the megathrust may serve as fluid conduits that create variability in deep fluid pressure thus segmenting the ETS zones and possibly the seismogenic portion of the subduction zone (Figure, 14). ETS tend to occur along subduction zones of young, warm oceanic lithospheric subduction (Walton et al., 2021) and occur with a recurrence time of about 10 to 19 months along Cascadia (Brudzinski and Allen, 2007). Geodetic measurements indicate that as much as 70% of the plate convergence budget is taken up by these events at the base of the seismogenic zone (Bartlow, 2020). The relation between the top of the ETS zone and base of the seismogenic zone is poorly understood as well as any causal relation between ETS activity and megathrust events.

Brudzinski and Allen (2007) suggested the Cascadia ETS earthquakes might be divided into 3 temporal and spatial groups (Figure 15) based on recurrence intervals of ETS events. As with other, later authors (for example, McKenzie 2022), they postulate that these different sections of the ETS zone may, in part, be the result of upper plate terrane rheologies. They suggest that the longer recurrence intervals of the Siletzia grouping (central) might be due to the more rigid, denser Siletzia block that stores strain longer which may impact the strength of the megathrust interface. Continued research in the role of ETS in potential segmentation of the seismogenic CSZ is ongoing (Luo and Liu, 2019; Bartlow, 2020; Hutchison, 2020; Bombardier et al., 2024)

1.3 Wedge and fault tip morphology

New tsunami modeling now includes the structure and geometry of the megathrust deformation zone near the trench-ward tip of the accretionary wedge (Figure 16). The potential role of steeply dipping coseismic faults with significant displacements could greatly increase tsunami wave heights. In the past, most subduction zone earthquakes were considered to be associated with low angle faults producing more horizontal slip (either blind or trench breaching) resulting in lessor tsunami amplitudes. Additionally, it may be that larger vertical displacements near the wedge tip produce similar or larger tsunami amplitudes during smaller (M7-8) events than M8-9 events associated with near horizontal slip at the base of the wedge (Wang and Tréhu, 2016; Melgar et al., 2019; Watt and Brothers, 2020; Small and Melgar, 2021; Walton et al., 2021; Wilson and Ma, 2021; Melgar, 2021; Aslam et al., 2021; Ledeczi et al., 2024). Increased interest in the character of coseismic accretionary wedge deformation accompanied the 2011 Tohoku-Oki earthquake where 50 to 120 m of coseismic slip occurred and significant trench-breaching rupture was largely responsible for the large, devastating accompanying tsunami (Wang and Tréhu, 2016).

The presence of large fault scarps in the accretionary wedge of Cascadia (Figures 3 and 17) suggest buried rupture or trench-breaching rupture may be accompanied by, or even supplanted by splay faults. For example Beeson (2017) identified a 60 m-high scarp representing a landward-frontal thrust in a late Pleistocene erosional surface within the offshore fold and thrust belt of Washington (Watt and Brothers, 2020). It isn’t clear how many events are represented by this scarp landward-vergent frontal thrust. Additionally, Watt and Brothers (2020) point out that splay faults and other structures that may move during the earthquake are closer to the coast than basal or blind thrusts thus decreasing travel time and warning time.

High-resolution seismic profiles along portions of the Cascadia offshore wedge have indicated that there is great variability in the distribution of splay faults and where they are present or absent (Watt and Brothers, 2020). They find that landward vergence within the outer wedge may be more prone to shallow megathrust or trench-breaching rupture than regions characterized by seaward vergence.

Ledeczi et al. (2024) conducted high-resolution near surface seismic reflection analysis of about 400 km of Cascadia offshore of Washington and Oregon. (Figure 18). They found numerous landward and seaward vergent faults with scarps and folds displaying 10's of meters of relief in late Quaternary sediments and surfaces. They suggested that the actively deforming domain is approximately 15 to 30 km wide in the Washington and Oregon portion of the subduction zone and that these structures are likely formed rapidly during coseismic displacement events. They also observe that these faults appear listric, steepening, in some cases to near vertical in the upper parts of the accretionary section. They equate these structures to faults like the Cape Cleare and Patton Bay faults in the Alaskan subduction zone that have near 70° dips and 39 m-high scarps. They conclude that models of splay fault rupture (Aslam et al., 2021) can double median tsunami heights relatively to low-angle basal faults.

Although they did not conduct this analysis at the southern portion of Cascadia, similarities in accretionary wedge morphology imaged near Humboldt Bay (Figures 2, 4 and 5) including an active oceanward, steep deformation front and presence of scarps in late Quaternary sediments suggest similar behavior might be expected. It should be noted that the deformation front is closer to the coast in northern California.

1.4 Recurrence and Segmentation

Recent proposed segmentation models of Cascadia are based on geophysical and geological along-strike similarities and differences, ETS occurrence, megathrust event recurrence based on ages and distributions of tsunami and turbidite deposits and onland evidence of subsidence and tsunami inundation (Figure 20).

In their summary of knowledge of the Cascadia subduction zone Walton et al., (2021) state that "Despite outstanding geologic records of past megathrust events, large uncertainty of the magnitude and frequency of CSZ earthquakes remains." There is little disagreement that the most recent event at Cascadia is the 1700 C.E. M9+ event, and there is general agreement that it was a full-margin rupture creating a M8.7 to 9.2 earthquake (for example, Atwater et al., 2005; Nelson et al., 2020; Walton et al., 2021). However, some recent physical modeling of tsunami generation suggests a tsunami of the size recorded in Japan could have been generated by a 400-km long (M8.7) southern Cascadia rupture (Melgar, 2021). He states that this would not conflict with the subsidence and dating information provided that at least four M<8.7 earthquakes occurring within years to decades afterward might fulfill the subsidence story to the north. He also states that these events would likely not produce a tsunami sufficient in size to be part of the Japan written record.

Salaree et al. (2021) conducted analysis of physics-based M7.5 to 9.2 related deformation of the subduction zone between central Oregon and southern Washington to evaluate tsunami hazard relative to shoreline characteristics, bathymetry and rupture characteristics. They concluded that the largest and most widespread tsunami amplitudes result from ruptures at or starting near mid-latitude portions of the CSZ. They conclude that, based on choice of slip model, a M>8.5 event can produce tsunami amplitudes exceeding 50% of those from a M9.2 rupture. They surmise that M8.5 earthquakes have a higher probability of occurrence (shorter recurrence interval) and hence may pose a more significant hazard than a larger event.

Onland supported recurrence estimates for CSZ events in Washington and northernmost Oregon are based on 10 widely correlated buried soils, often accompanied by overlying tsunami deposits that provide a recurrence average of 500-540 years for the last 5000 years (Atwater and Hemphill-Haley, 1997; Nelson et al., 2006; Walton et al., 2021). In southern Oregon and northern California a record of 12 potential earthquakes and tsunamis provide an average recurrence interval of ~390 years (Witter et al., 2003; Priest et al., 2014, 2017; Graehl et al., 2015; Milker et al., 2016; Walton et al., 2021; Padgett et al., 2021, 2022).

Margin-wide rupture recurrence intervals of 500 -530 years are estimated from offshore turbidite records (Goldfinger et al., 2012) however there are concerns about these estimates (see below).

At the Salmon River estuary in Oregon, La Selle et al (2024) consider the displacement (and thus earthquake rupture length and magnitude) based on 129 marsh cores and reexamined older collected cores to estimate inland inundation by tsunami. They compared 15 rupture models and concluded that 12 to 27 m of slip immediately offshore along with 0.8-1.4 m of coastal subsidence was required to produce tsunami of sufficient size to satisfy their data. With this data they tested the Melgar (2021) model of smaller (M~8.7 earthquake followed a few years or decades by smaller (M<8.7) earthquakes. They were unable to refute that model.

Offshore records of turbidite production proposed by Goldfinger et al. (2012, 2013) provide a much more extensive record of earthquake history than the onshore record. However, questions as to the potential for storm-generated turbidites and overinterpretation of some correlations (Atwater et al., 2014; Goldfinger et al., 2016; Lindh, 2016; Walton et al., 2021) have left some doubt as to the error associated with this proposed longer record offshore. This, in turn, has led to critical discussion about whether all or most of the turbidite sequences represent full-margin rupture as proposed by Goldfinger et al., 2012, 2013, 2016). Additionally, using the turbidite-based earthquake chronology Kulkarni et al. (2013) proposed that statistical analysis of the data suggest temporal clustering of full margin earthquakes in Cascadia separated by temporal seismic gaps of hundreds of years. Lindh (2016) criticizes the method of interpreting magnitude based on turbidite thickness (Goldfinger et al., 2012, 2013) and suggests there is insufficient evidence for temporal clustering.

Staisch (2024) considered uncertainties in radiocarbon-based dates for onshore data and supported the Melgar (2021) conclusion that a series of smaller earthquakes are permissible with those data. She also considered the offshore record, and considers the full-rupture model may not be sound, especially considering modeling by Howarth et al. (2021) that states that not all coseismic turbidites owe their origin to megathrust events but some may be generated by upper-plate earthquakes as small as M7.9. Both also propose that a smaller earthquake, with a rupture of 400-500 km length, and with appropriate splay architecture could produce a large tsunami. Staisch (2024) concludes that large uncertainties in turbidite ages do not necessarily support periodic full-rupture of Cascadia.

Nieminski et al. (2024) tested the ability to correlate age and stratigraphy of marine cores over long and short distances. They conducted numerous tests that indicate significant differences over short distances and they conclude that not all deposits can be correlated with confidence. They refute Goldfinger's (2012) assertion that there are "characteristic" fingerprints that can be correlated over long distances and suggest these can be challenging even over short distances. They posit that statistically significant correlation between cores can only be made over <100 m separation.

Gomberg (2018) evaluated strong motion effects on production of submarine landslides and turbidity currents. She used seismic records from seafloor ocean bottom seismometers and onshore records to conclude that submarine geology, structures and topography strongly impact shaking. She advised that more attention needs to be paid to this information when intepreting widespread records of turbidites as proxies for earthquake chronology and magnitude.

Finally, there are estimates for ages of coseismic subsidence events (Table 1) in northern Humboldt Bay (Padgett, 2021, 2022). They conclude that the magnitudes of subsidence are different for these events suggesting full- and partial margin ruptures may be recorded in the marsh stratigraphy. Additionally, they correlate these events to others as far north as Talbot Creek in southern Oregon a distance of about 300 km which is compatible with smaller rupture events (Figure 21).

Figures

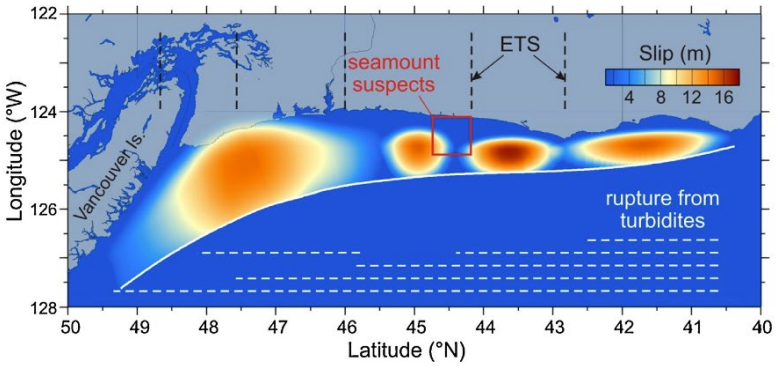

Figure 1 – Proposed variations in megathrust slip behavior along the Cascadia margin (Wang and Tréhu, 2016). The oval colors immediately east of the megathrust are proposed slip distributions associated with the 1700 C.E. earthquake. Black dashed lines are ETS boundaries (Brudzinski and Allen, 2007). White dashed lines suggest rupture extents based on turbidite occurrence (Goldfinger et al., 2012). Based on the turbidite evidence Wang and Tréhu (2016) suggest subduction zone events are more frequent at its southern end (Northern California).

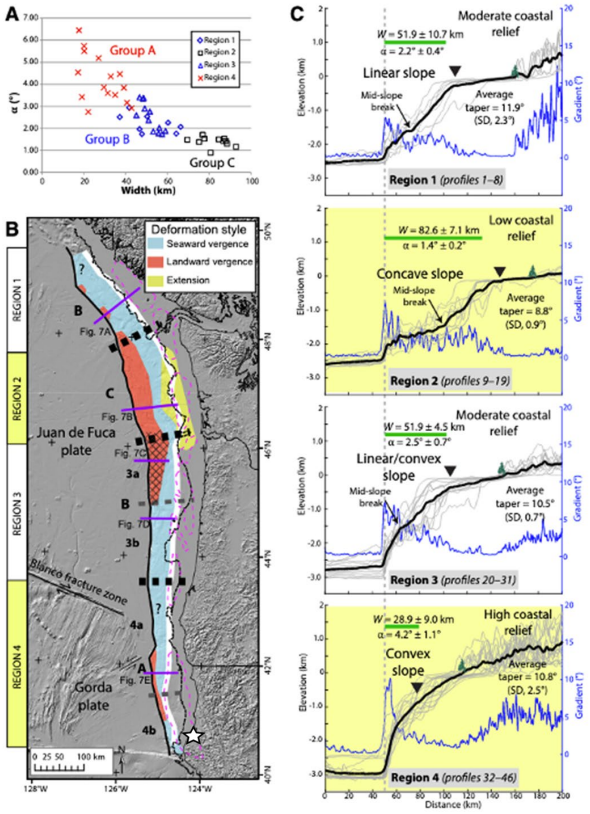

Figure 2 – Morpho-tectonic analysis (modified from Watt and Brothers, 2020). (A) Three groups of wedge width relative to gradient. (B) Map of outer wedge structural vergence with dark gray dashed lines representing groupings from (A). Note Region 4 that includes the southern part of Cascadia is associated with Group A characteristics that are steep and narrow. Red and blue areas contain primarily landward and seaward vergent thrust faults, respectively. Magenta dashed lines encircle shelf forearc basins (Wells et al., 2003). (C) Average topographic profile (black line) and gradient (blue line). Gray dashed vertical line indicates position of the deformation front. Green horizontal bar represents the width of the outer wedge. Multiple faint gray lines are individual profiles. Note that the southern Cascadia margin contains a narrow belt of landward vergent faults in addition to seaward vergent scarps. White star in (B) indicates approximate location of ISFSI.

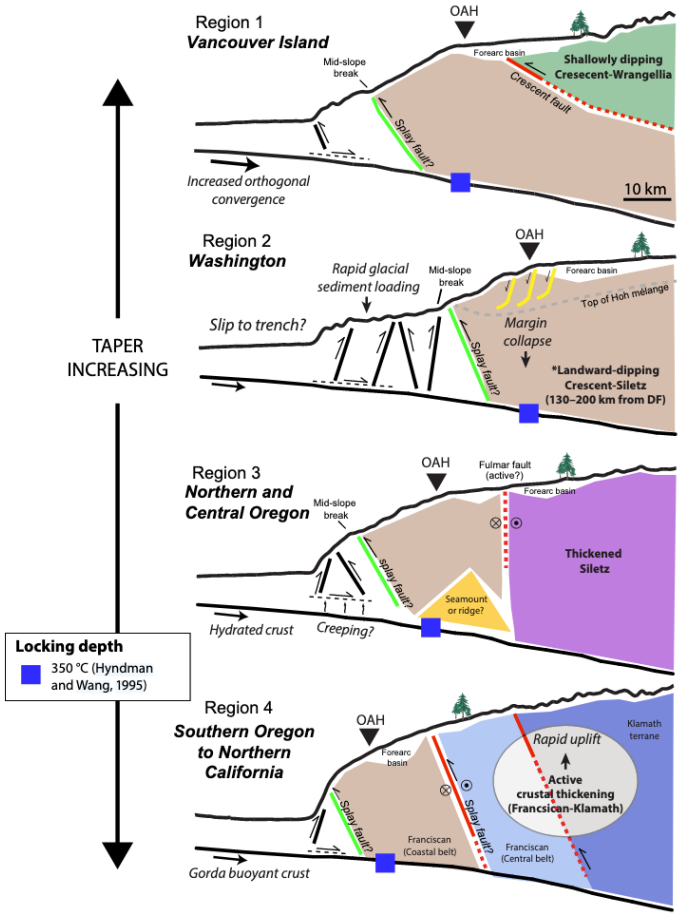

Figure 3 - Regional conceptual models illustrating the first-order along-strike variability in morphology and structure along Cascadia's marine forearc in relation to outer wedge taper and strength heterogeneities in the upper plate (From Watt and Brothers, 2020). It appears that megathrust splay faults are commonly associated with backstop boundaries. Trees depict approximate position of the shoreline within each region. DF—deformation front.. Note that outer wedge taper is lowest in region 2 and increases to the north and south. OAH—outer arc high; DF—deformation front. Note the steep outer wedge in region 4 (Gorda) and landward vergent thrust near the megathrust tip.

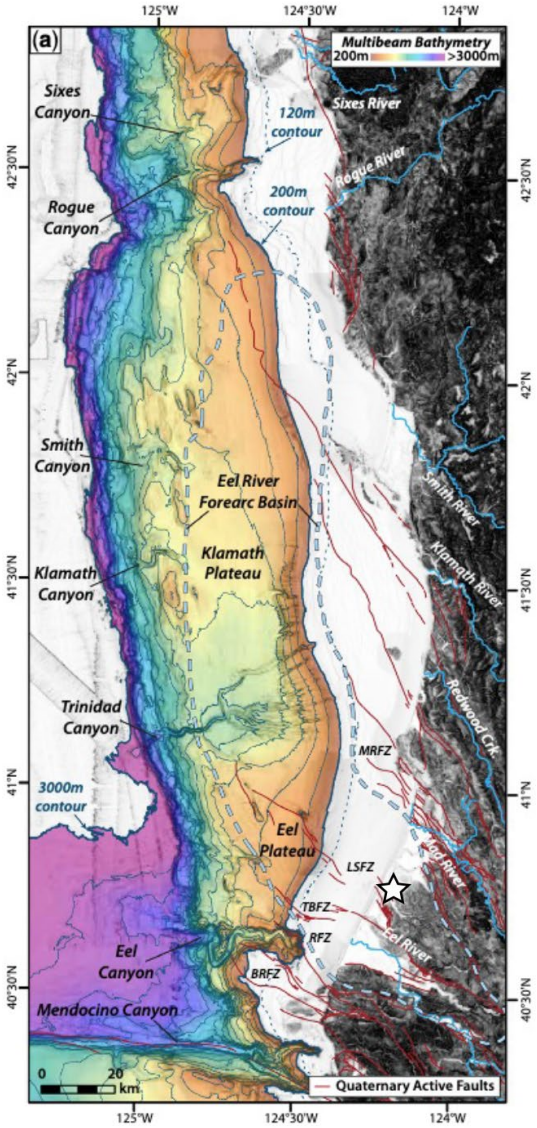

Figure 4 – Bathymetry, major rivers and structural features of the southern Cascadia margin (from Hill et al. 2020). Star indicates approximate location of ISFSI. The steepest part of the accretionary prism is located near the base of the slope. Note the Eel and Trinidad canyons in the vicinity of Humboldt Bay. Also note the steep oceanward tip of the wedge.

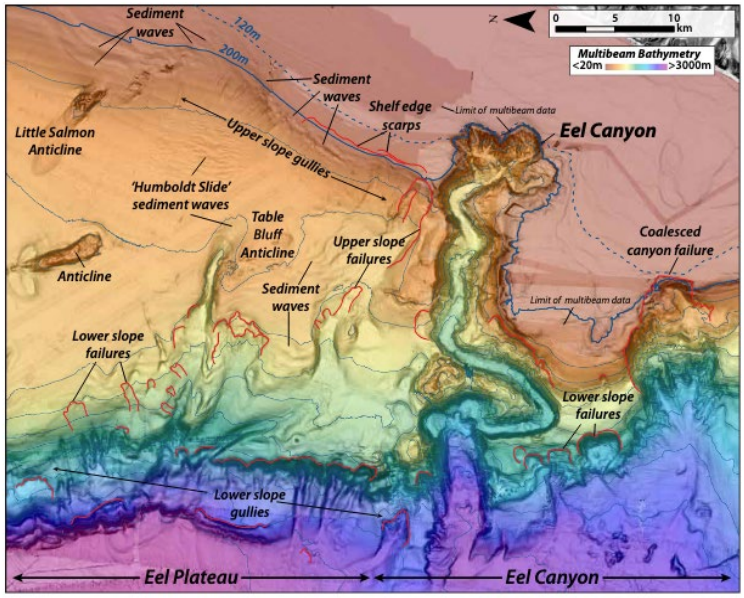

Figure 5 – Bathymetry of the southernmost subduction margin at Eel Canyon. Noticeable are the presence of folds associated with the Little Salmon and Table Bluff faults. Also notable are significant submarine landslide features including sediment waves, coalesced canyon headwall failures and smaller individual failures, mainly located in the steeper outer part of the wedge (from Hill et al., 2020).

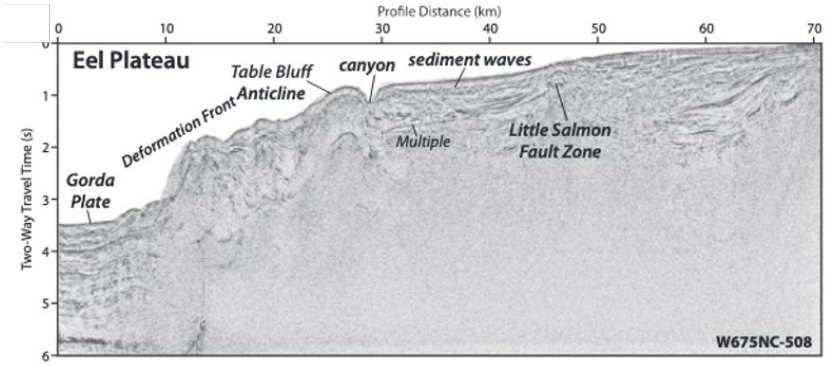

Figure 6 – Sparker profile crossing the Little Salmon and Table Bluff faults and also showing the steep deformation front characteristic of this portion of the subduction margin and the absence of well-defined trench (from Hill et al., 2020).

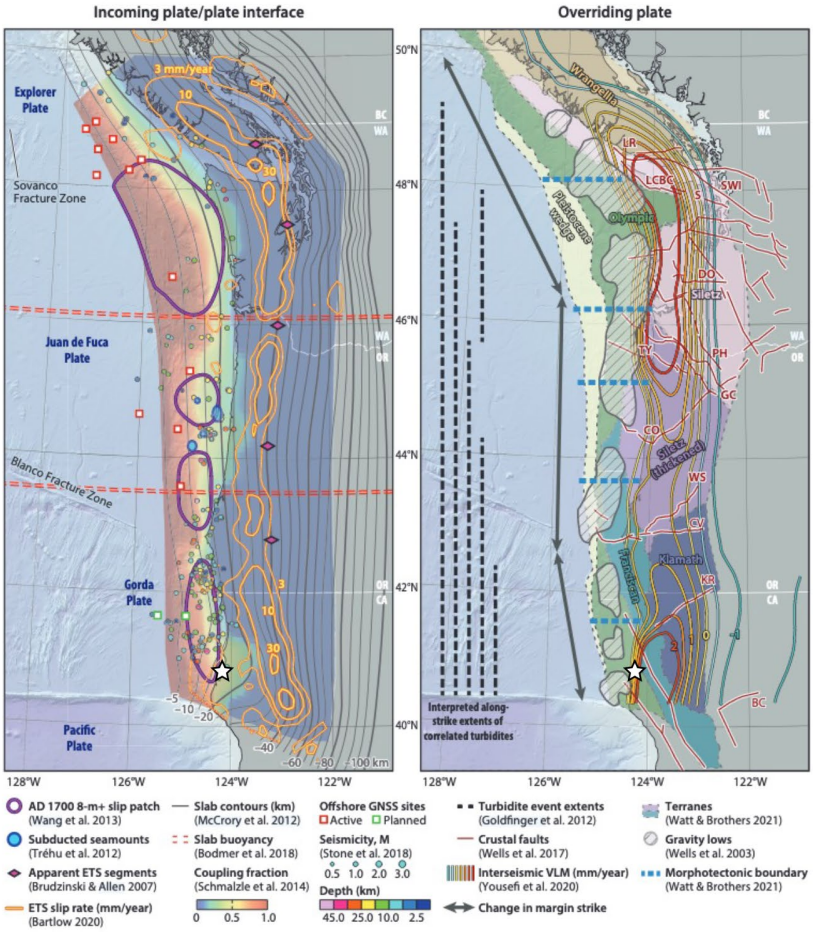

Figure 7 – Geological and geophysical data indicate heterogeneity in the Cascadia margin (from Walton et al., 2021, their Figure 5). Left map shows conditions within the subducting plate and the megathrust. Purple ovals represent interpreted high-slip patches during the 1700 C.E. M>9 earthquake. Orange boundaries indicate slip rates (mm/yr) on ETS patches (Bartlow, 2020). Map on the right shows conditions in the upper plate of the subduction zone. Seismicity in the Juan de Fuca plate may be related to seamounts being subducted (Tréhu et al., 2012; Stone et al., 2018). Seismicity in the Gorda plate likely due to internal deformation of the plate as a result of plate boundary conditions, Pacific plate to the south and Juan de Fuca plate to the north (Rollins and Stein, 2010). Star indicates approximate location if ISFSI.

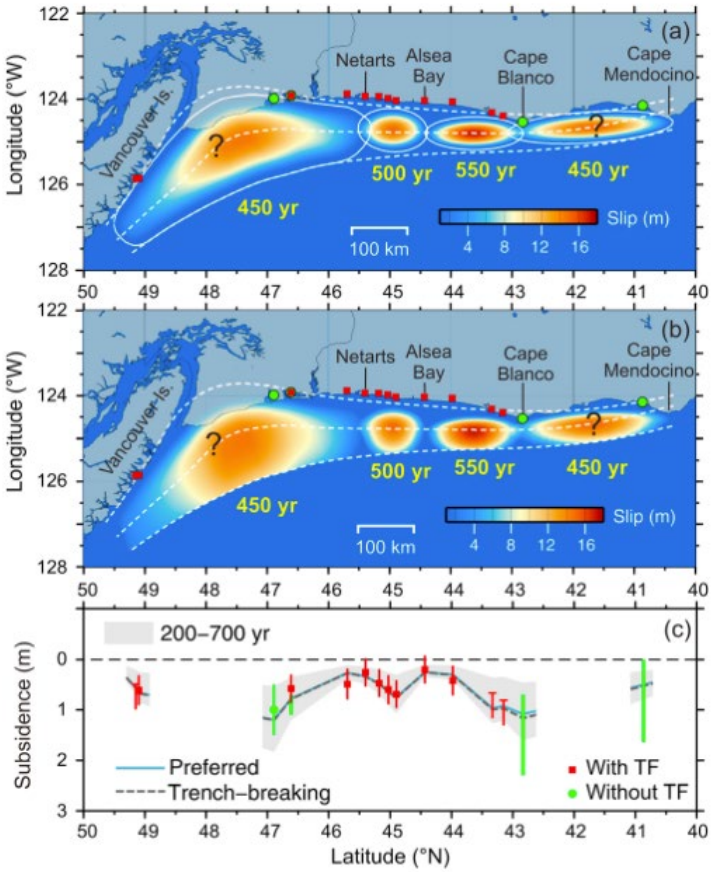

Figure 8 – Preferred along strike rupture model for the 1700 C.E. M9+ Cascadia full length rupture scenario (Wang et al., 2013, their Figure 6). (a) preferred rupture model without the rupture breaking at the trench. (b) alternative model that allows for rupture to extend to the surface at the trench and (c) comparison of rupture models to onshore estimates of coseismic subsidence. Both the preferred (a) model and trench-breaking (b) compare well with the onshore data. Year estimates in (a) and (b) for rupture patches indicate slip accumulation time. TF in (c) stands for transfer function statistical methodology used to analyze coseismic vertical land motion based on foraminifera assemblages and elevations (for example Engelhart et al., 2016).

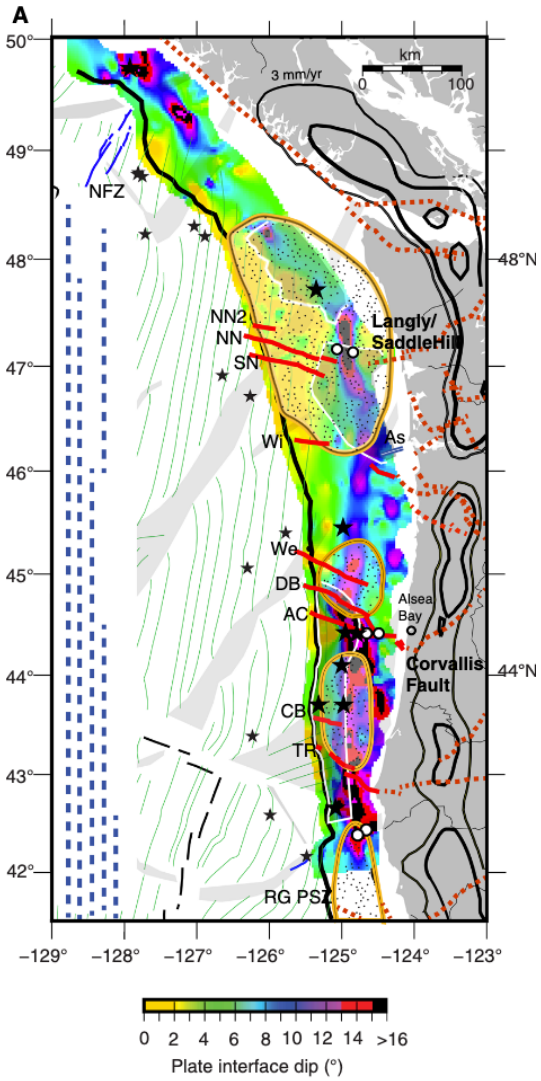

Figure 9 – Plate interface of Cascadia north of California/Oregon border from Carbotte et al. (2024). Offshore base image is calculated dip of the plate interface. Note the steep dip of southern Cascadia in Oregon and lack of appreciable low angle plate near the southern end. Locations of 1700 C.E. M>9 earthquake rupture patches and ETS slip rate contours are similar to Walton et al. (2021). Onshore faults (red dashed lines – Wells et al. (2017) and offshore oblique strike-slip faults (red solid lines (Goldfinger et al., 1997).

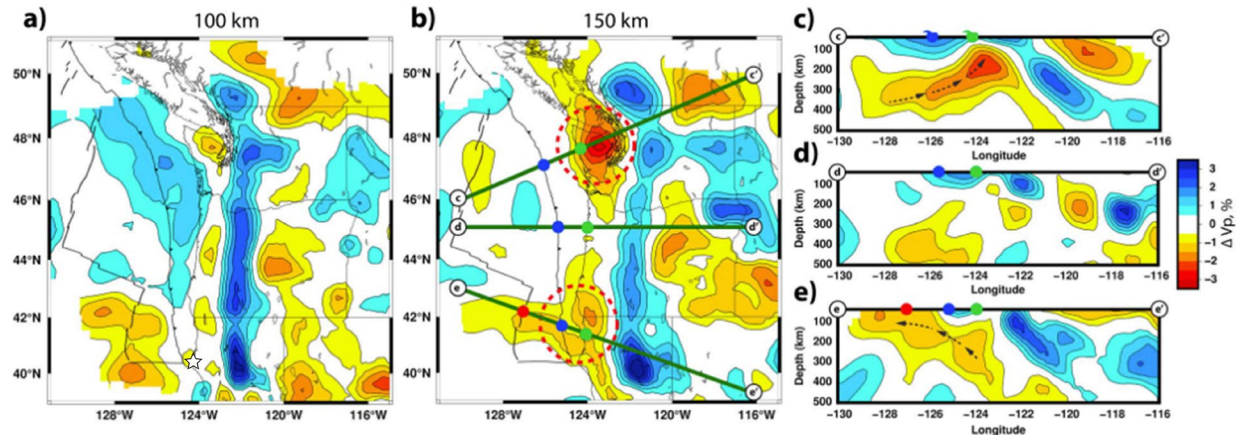

Figure 10 – Tomographic images of the upper mantle of the entire Pacific Northwest and adjacent oceanic plates (from Bodmer et al. (2018, their Figure 2). Dark blue colors are high velocity (relatively cool, dense material) and red colors are low velocity (relatively warm, buoyant material). (a) 100 km depth slice showing the position of the subducting slab at that depth. Also note velocity differences between the Juan de Fuca plate to the north (cool, dense) and Gorda plate (warm, buoyant) to the south. (b) 150 km depth slice showing highly buoyant mantle material in the vicinity of the Olympic Peninsula (c) and at southern Cascadia (e). Star in a) depicts approximate location of ISFSI.

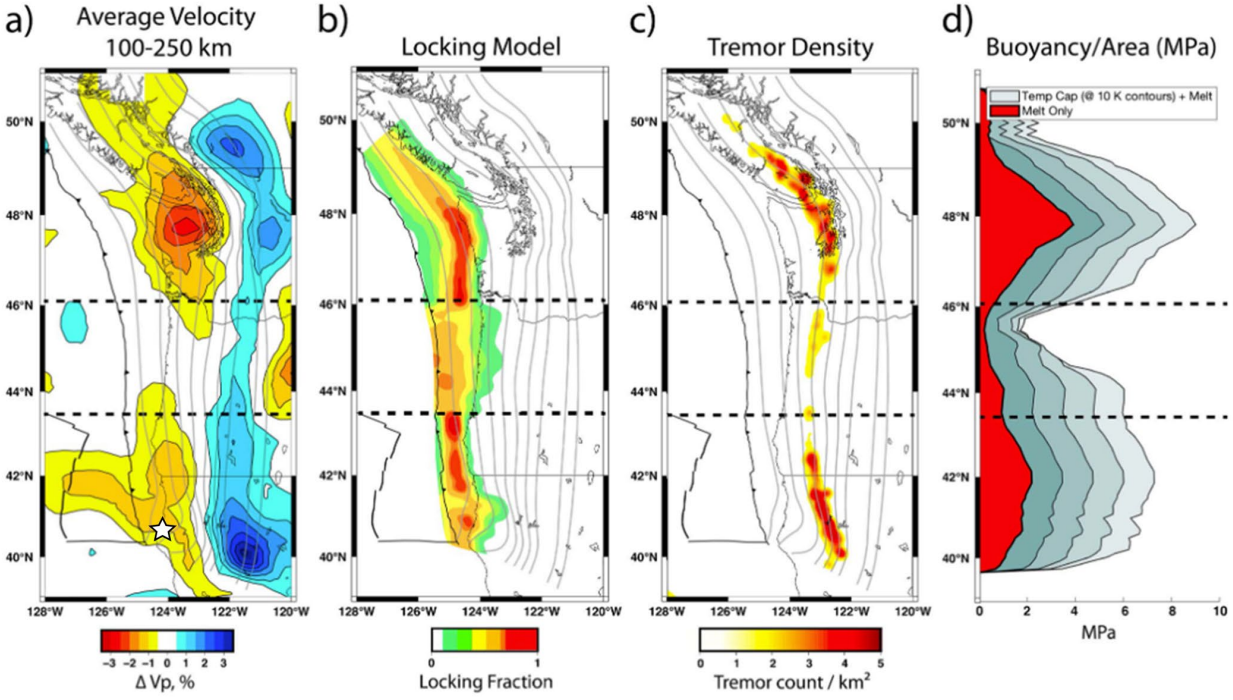

Figure 11 – (a) average P wave velocity between 100-250 km depth, gray contours at 10 km intervals of the top of the subducting plate, (b) plate fraction locking model (red = greater locking), (c) ETS density from 2009 to 2015, (d) average buoyancy variation beneath the slab showing two large buoyant areas at the latitude of Olympic Peninsula and southern Cascadia. Star in a) depicts approximate location of ISFSI.

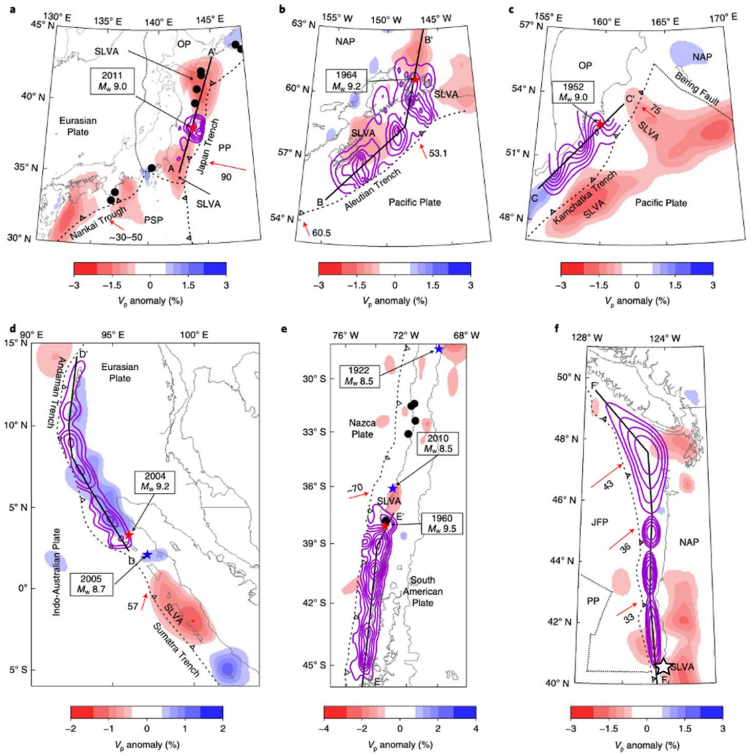

Figure 12 – Tomographic images of Pwave velocity (V_P) beneath the subducting slab, coseismic slip and epicentral locations for 5 historic M9 and smaller earthquakes along with interpreted coseismic slip (f) during the 1700 C.E. Cascadia earthquake (from Fan and Zaoh (2021), their Figure 1). Note low velocity (red) and high velocity (blue) anomalies and their positions relative to M9+ earthquakes (red stars). They tend to be associated with margins of the velocity models. They speculate that the large velocity lows at Cascadia may coincide with the unknown epicenter for the 1700 C.E. rupture. White star in (f) is approximate location for ISFSI.

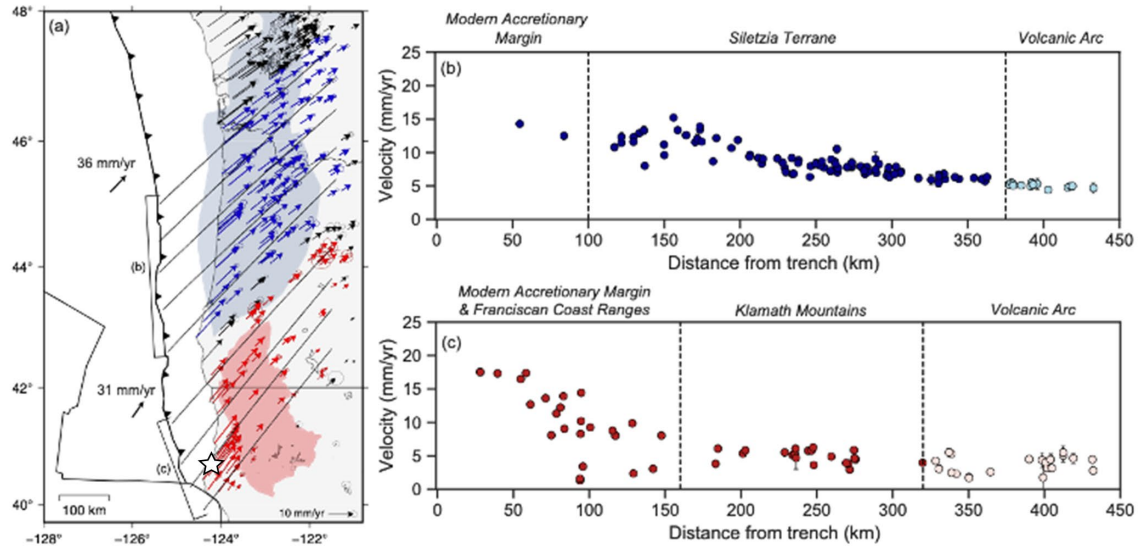

Figure 13 – Juan de Fuca and Gorda horizontal velocity fields relative to North America (from McKenzie et al (2022, their Figure 3). (a) upper plate subduction velocities within the Klamath and Franciscan terrane (red) and Siletzia (blue). Black, northeast oriented lines are velocity profile swaths created parallel to relative oceanic plate motions, (b) subduction-related velocities within Siletzia terrane including the accretionary margin and volcanic arc. (c) subduction-related velocities within the Franciscan and Klamath terranes to the south and volcanic arc. Vertical dashed lines in (b) and (c) are approximate terrane boundaries. White star indicates approximate location of ISFSI.

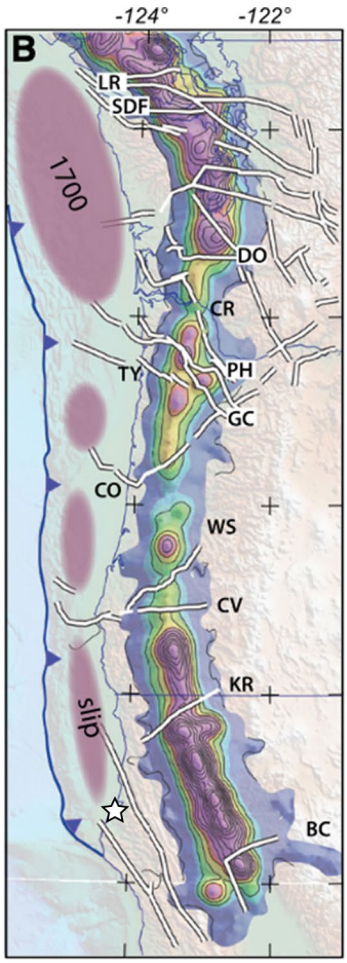

Figure 14 – Tremor density with respect to forearc faults (from Wells et al. 2017). The purple, offshore ovals are areas of possible greatest slip during the 1700 C.E. M9+ earthquake. It is postulated that gaps in the ETS regions may be controlled by the faults that tap high pressure fluids in the ETS region. White lines are crustal faults from state fault database. The importance of the role of ETS in earthquake genesis in subduction zones is still not clear.

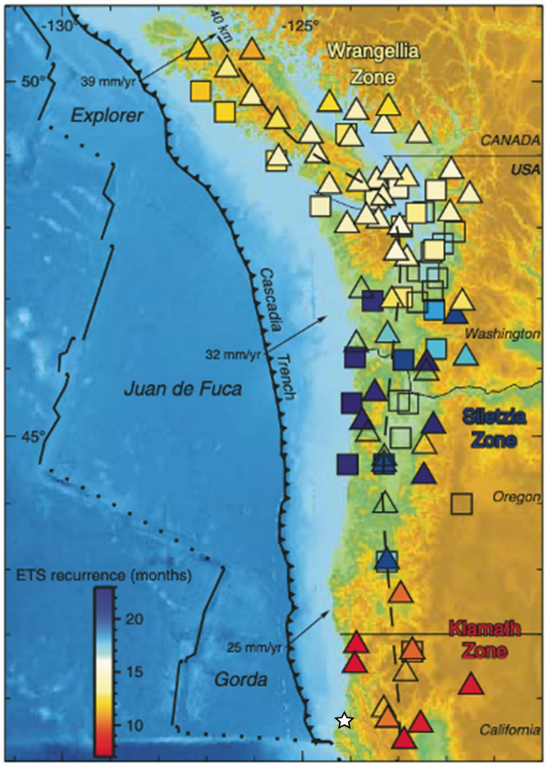

Figure 15 – Map of ETS occurrences along Cascadia along with recurrence (from Brudzinski and Allen, 2007, their Figure 1). Note that shortest recurrence intervals (~10 months) occur in the southernmost "Klamath Zone", the central "Siletzia" zone has the longest recurrence intervals (~ 20 months) and the northern "Wrangellia" zone has an intermediate recurrence (~12-15 months). Squares and triangles indicate the locations of permanent GPS stations and seismometers at the time of the publication. There are more now. White star indicates approximate location of ISFSI.

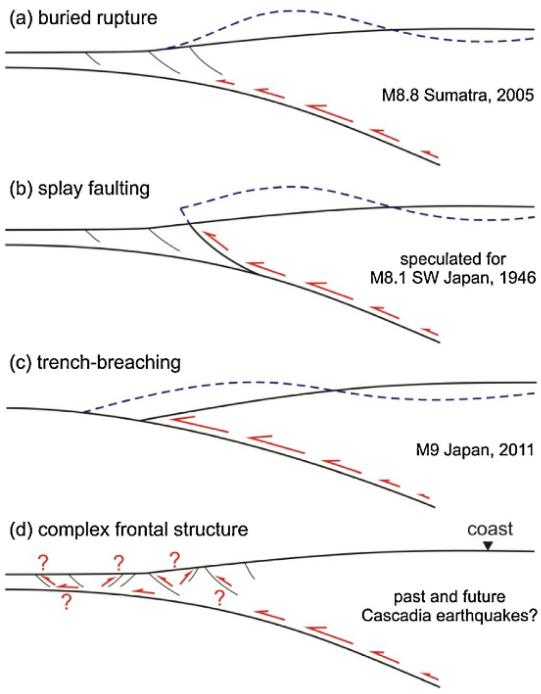

Figure 16 – Potential accretionary wedge deformation scenarios associated with subduction zone megathrust rupture (from Wang and Trehu, 2016, their figure 5).

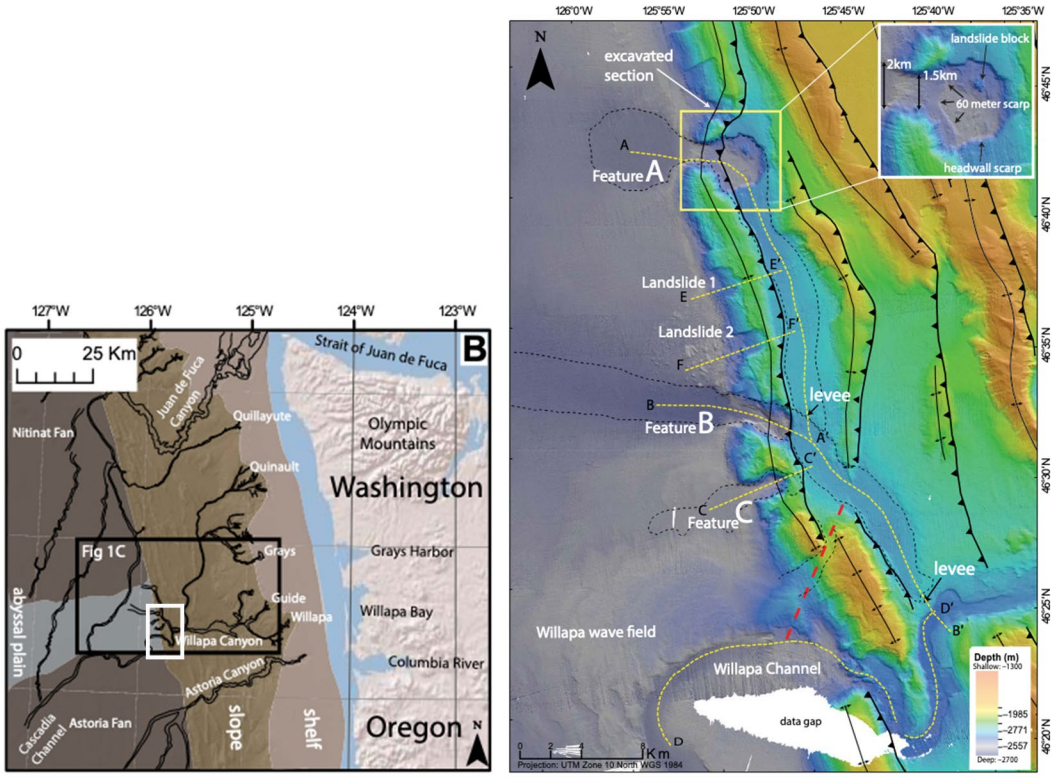

Figure 17 – Bathymetric map of a portion of the Cascadia deformation front offshore of southern Washington at Willapa Bay (from Beeson et al., 2017, their Figure1b and 2). Location of the figure to the right is indicated on the left figure as a white box. Sawtooth lines are locations of thrust faults at the surface along with folds (lines with double arrows). Yellow box highlights enlarged area and 60 m high, landward-facing scarp in a late Pleistocene erosion surface.

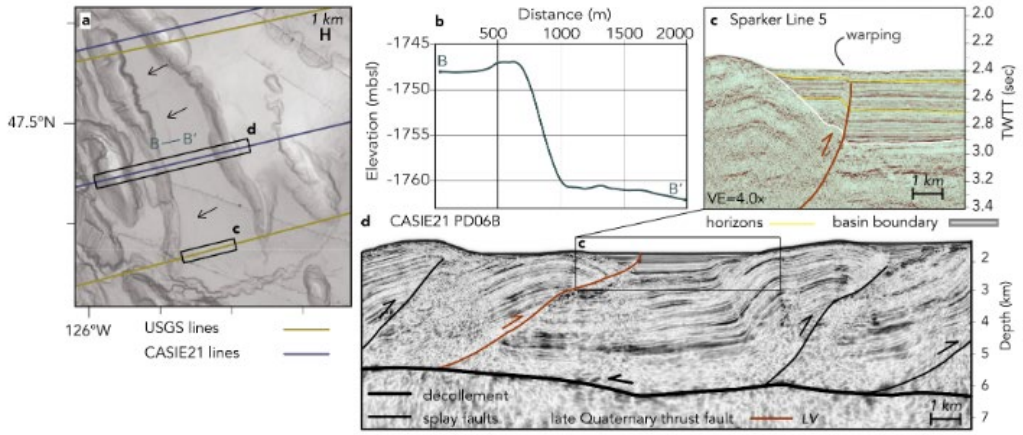

Figure 18 – Seismic reflection profile of a landward-vergent thrust (from Ledeczi et al. 2024, their Figure 3) in offshore northern Washington. (a) map view of fault area with arrows pointing to fault scarp, (b) bathymetric profile of the fault scarp indicating about 13 m of relief on the seafloor, (c) sparker profile showing the faulted and folded older sediments and warping of late Quaternary cover sediments, and (d) projection of the fault onto the larger deformation front and connection to the décollement.

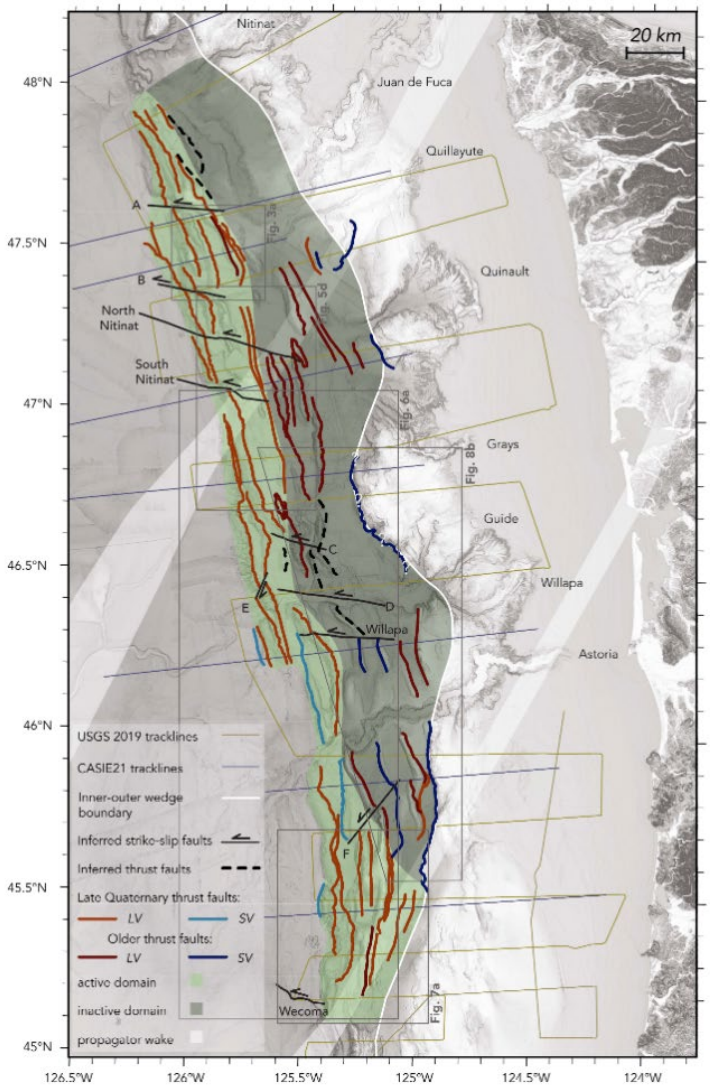

Figure 19 – Outer accretionary wedge of a portion of the deformation front Washington and Oregon (from Ledeczi et al. 2024, their Figure 4). Active landward vergent and seaward vergent thrust faults are represented by light red and light blue lines, respectively. Darker red and blue lines represent older thrust faults. Light green shading indicates actively deforming outward portion of the wedge. Note the position of these active structures in relation to wedge morphology in southern Cascadia and offshore Humboldt Bay (Figures 2, 4 and 5).

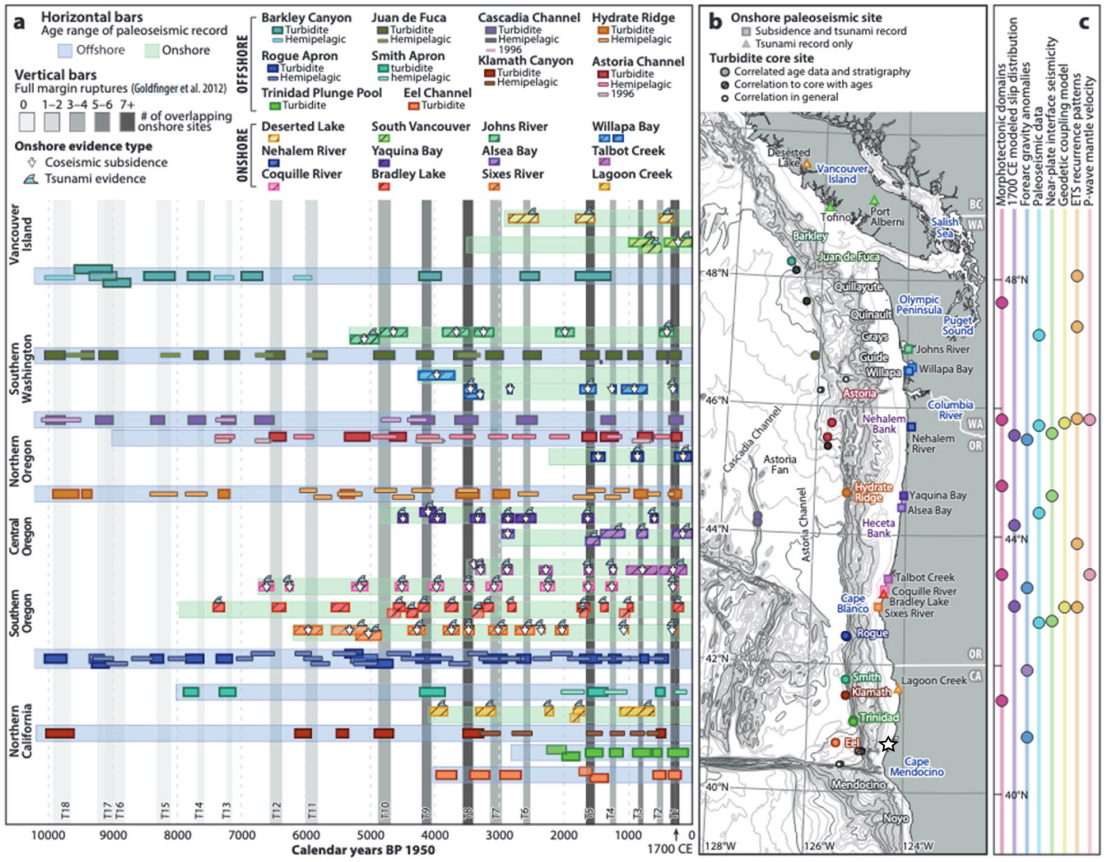

Figure 20 – Onshore and offshore evidence for earthquakes and tsunamis along Cascadia (from Walton et al, 2021, their figure 4).

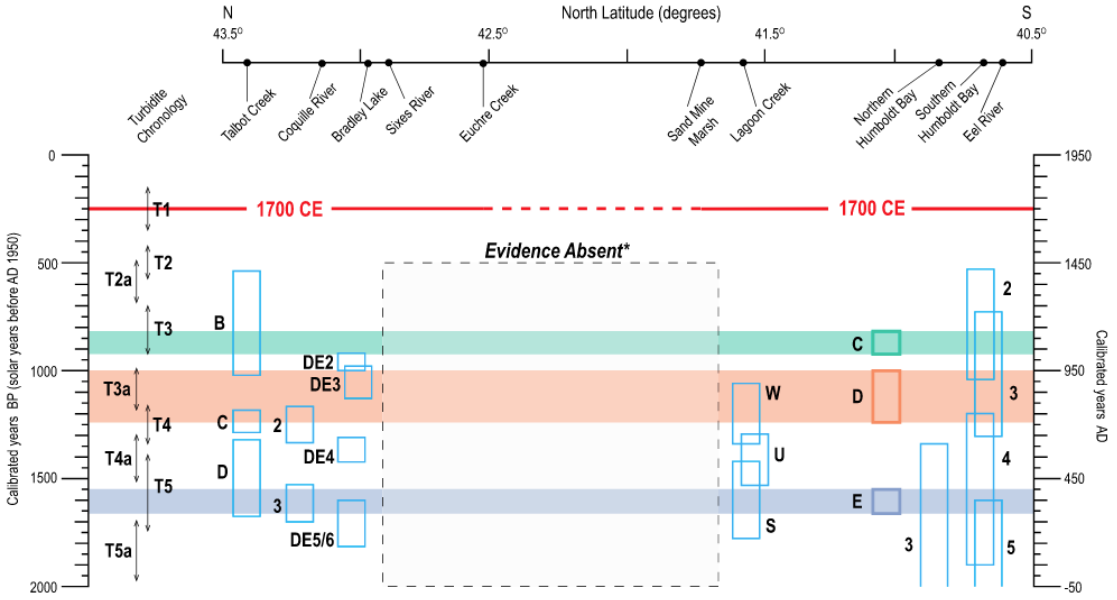

Figure 21 – Comparison of interpreted coseismic subsidence events from Humboldt County north to southern Oregon (Padgett et al, 2021). The 1700 C.E. event and events C, D and E at northern Humboldt Bay appear to correlate with other locations indicting at least 300 km of contemporaneous rupture.

TABLES

Age of earthquake (youngest at top)	Estimate of coseismic subsidence (2021)
250 cal yr BP (1700 CE) -	- 0.4 to -1.3 (m) - 1.3 to -4.3 (ft)
ca. 875 cal yr BP	-0.05 to -0.8 m -0.16 to -2.6 (ft)
ca. 1120 cal yr BP	0.79 ± 0.47 (m) -0.32 to -1.3 (ft)
ca. 1620 cal yr BP	> -0.93m >-3 m

Table 1 – Timing and coseismic subsidence at North Humboldt Bay (from Padgett et al. 2021) identified the four most recent events from cores.

References

Aslam, K.S., Thomas, A.M., and Melgar, D., 2021, The Effect of Fore-Arc Deformation on Shallow Earthquake Rupture Behavior in the Cascadia Subduction Zone: Geophysical Research Letters, v. 48, p. e2021GL093941, doi:10.1029/2021GL093941.

Atwater, B.F., Carson, B., Griggs, G.B., Johnson, H.P., and Salmi, M.S., 2014, Rethinking turbidite paleoseismology along the Cascadia subduction zone: Geology, v. 42, p. 827–830, doi:10.1130/G35902.1.

Atwater, B.F., and Hemphill-Haley, E., 1997, Recurrence Intervals for Great Earthquakes of the Past 3500 Years at Northeastern Willapa Bay, Washington: v. 1576, p. 108.

Atwater, B.F., Musumi-Rokkaku, S., Satake, K., Tsuji, Y., Ueda, K., and Yamaguchi, D.K., 2005, The orphan tsunami of 1700—Japanese clues to a parent earthquake in North America: Seattle, WA / Washington, D.C., University of Washington Press and U.S. Geological Survey Professional Paper 1707, 135 p., http://pubs.er.usgs.gov/publication/pp1707 (accessed May 2020).

Bartlow, N.M., 2020, A Long-Term View of Episodic Tremor and Slip in Cascadia: Geophysical Research Letters, v. 47, p. e2019GL085303, doi:10.1029/2019GL085303.

Beeson, J.W., Goldfinger, C., and Fortin, W.F., 2017, Large-scale modification of submarine geomorphic features on the Cascadia accretionary wedge caused by catastrophic flooding events: Geosphere, v. 13, p. 1713–1728, doi:10.1130/GES01388.1.

Bilek, S.L., and Lay, T., 2018, Subduction zone megathrust earthquakes: Geosphere, v. 14, p. 1468–1500, doi:10.1130/GES01608.1.

Bodmer, M., Toomey, D.R., Hooft, E.E.E., and Schmandt, B., 2018, Buoyant Asthenosphere Beneath Cascadia Influences Megathrust Segmentation: Geophysical Research Letters, v. 45, p. 6954–6962, doi:10.1029/2018GL078700.

Bombardier, M., Cassidy, J.F., Dosso, S.E., and Kao, H., 2024, Spatial Distribution of Tremor Episodes From Long-Term Monitoring in the Northern Cascadia Subduction Zone: Journal of Geophysical Research: Solid Earth, v. 129, p. e2024JB029159, doi:10.1029/2024JB029159.

Brudzinski, M.R., and Allen, R.M., 2007, Segmentation in episodic tremor and slip all along Cascadia: Geology, v. 35, p. 907, doi:10.1130/G23740A.1.

Carbotte, S.M. et al., 2024, Subducting plate structure and megathrust morphology from deep seismic imaging linked to earthquake rupture segmentation at Cascadia: Science Advances, v. 10, p. eadl3198, doi:10.1126/sciadv.adl3198.

Dragert, H., Wang, K.-K., and James, T., 2001, Episodic Silent Slip: A New Aspect of Cascadia Megathrust Behaviour: AGU Fall Meeting Abstracts,.

Engelhart, S.E., Hemphill-Haley, E., Kelsey, H.M., and Padgett, J.S., 2016, Refined Estimates of Coseismic Subsidence along the Southern Cascadia Subduction Zone in Northern Humboldt Bay (Arcata Bay): Collaborative Research with University of Rhode Island and Humboldt State University: U.S. Geological Survey NERHP Final Technical Report G14AP00128, G14AP00129, 38 p.

Fan, J., and Zhao, D., 2021, Subslab heterogeneity and giant megathrust earthquakes: Nature Geoscience, v. 14, p. 349–353, doi:https://doi.org/10.1038/s41561-021-00728-x.

Gao, X., and Wang, K., 2017, Rheological separation of the megathrust seismogenic zone and episodic tremor and slip: Nature, v. 543, p. 416–419, doi:10.1038/nature21389.

Goda, K., 2023, Statistical characterization of full-margin rupture recurrence for Cascadia subduction zone using event time resampling and Gaussian mixture model: Geoscience Letters, v. 10, p. 52, doi:10.1186/s40562-023-00306-6.

Goldfinger, C. et al., 2012, Turbidite event history—Methods and implications for Holocene paleoseismicity of the Cascadia subduction zone: U.S. Geological Survey Professional Paper Professional Paper 1661-F, 170 p.

Goldfinger, C., Kulm, L.D., Yeats, R.S., McNeill, L., and Hummon, C., 1997, Oblique strike-slip faulting of the central Cascadia submarine forearc: Journal of Geophysical Research: Solid Earth, v. 102, p. 8217–8243, doi:10.1029/96JB02655.

Goldfinger, C., Morey, A.E., Black, B., Beeson, J., Nelson, C.H., and Patton, J., 2013, Spatially limited mud turbidites on the Cascadia margin: segmented earthquake ruptures? Natural Hazards and Earth System Sciences, v. 13, p. 2109–2146, doi:10.5194/nhess-13-2109-2013.

Goldfinger, C., Wong, I., Kulkarni, R., and Beeson, J., 2016, Reply to "Comment on 'Statistical Analyses of Great Earthquake Recurrence along the Cascadia Subduction Zone' by Ram Kulkarni, Ivan Wong, Judith Zachariasen, Chris Goldfinger, and Martin Lawrence" by Allan Goddard Lindh: Bulletin of the Seismological Society of America, v. 106, doi:10.1785/0120150282.

Gomberg, J., 2018, Cascadia Onshore-Offshore Site Response, Submarine Sediment Mobilization, and Earthquake Recurrence: Journal of Geophysical Research: Solid Earth, v. 123, p. 1381–1404, doi:10.1002/2017JB014985.

Graehl, N.A., Kelsey, H.M., Witter, R.C., Hemphill-Haley, E., and Engelhart, S.E., 2015, Stratigraphic and microfossil evidence for a 4500-year history of Cascadia subduction zone earthquakes and tsunamis at Yaquina River estuary, Oregon, USA: Geological Society of America Bulletin, v. 127, p. 211–226, doi:10.1130/B31074.1.

Hall, K., Houston, H., and Schmidt, D., 2018, Spatial Comparisons of Tremor and Slow Slip as a Constraint on Fault Strength in the Northern Cascadia Subduction Zone: Geochemistry, Geophysics, Geosystems, v. 19, p. 2706–2718, doi:10.1029/2018GC007694.

Harrichhausen, N., Morell, K.D., and Regalla, C., 2024, Forearc faults in northern Cascadia do not accommodate elastic strain driven by the megathrust seismic cycle: Seismica, v. 2, doi:10.26443/seismica.v2i4.1177.

Hill, J.C., Watt, J.T., Brothers, D.S., and Kluesner, J.W., 2020, Submarine canyons, slope failures and mass transport processes in southern Cascadia: Geological Society, London, Special Publications, p. SP500-2019–169, doi:10.1144/SP500-2019-169.

Howarth, J.D. et al., 2021, Calibrating the marine turbidite palaeoseismometer using the 2016 Kaikōura earthquake: Nature Geoscience, v. 14, p. 161–167, doi:10.1038/s41561-021-00692-6.

Hutchinson, I., and Clague, J., 2017, Were they all giants? Perspectives on late Holocene plate-boundary earthquakes at the northern end of the Cascadia subduction zone: Quaternary Science Reviews, v. 169, p. 29–49, doi:10.1016/j.quascirev.2017.05.015.

Hutchison, A.A., 2020, Inter-episodic Tremor and Slip Event Episodes of Quasi-spatiotemporally Discrete Tremor and Very Low Frequency Earthquakes in Cascadia Suggestive of a Connective Underlying, Heterogeneous Process: Geophysical Research Letters, v. 47, p. e2019GL086798, doi:10.1029/2019GL086798.

Kulkarni, R., Wong, I., Zachariasen, J., Goldfinger, C., and Lawrence, M., 2013, Statistical Analyses of Great Earthquake Recurrence along the Cascadia Subduction Zone: Bulletin of the Seismological Society of America, v. 103, p. 3205–3221, doi:10.1785/0120120105.

La Selle, S.M., Nelson, A.R., Witter, R.C., Jaffe, B.E., Gelfenbaum, G., and Padgett, J.S., 2024, Testing Megathrust Rupture Models Using Tsunami Deposits: Journal of Geophysical Research: Earth Surface, v. 129, p. e2023JF007444, doi:10.1029/2023JF007444.

Ledeczi, A., Lucas, M., Tobin, H., Watt, J., and Miller, N., 2024, Late Quaternary Surface Displacements on Accretionary Wedge Splay Faults in the Cascadia Subduction Zone: Implications for Megathrust Rupture: Seismica, v. 2, doi:10.26443/seismica.v2i4.1158.

Lindh, A., 2016, Comment on “Statistical Analyses of Great Earthquake Recurrence along the Cascadia Subduction Zone” by Ram Kulkarni, Ivan Wong, Judith Zachariasen, Chris Goldfinger, and Martin Lawrence: Bulletin of the Seismological Society of America, v. 106, doi:10.1785/0120150069.

Luo, Y., and Liu, Z., 2019, Rate-and-State Model Casts New Insight into Episodic Tremor and Slow-slip Variability in Cascadia: Geophysical Research Letters, v. 46, p. 6352–6362, doi:10.1029/2019GL082694.

McKenzie, K.A., Kelsey, H.M., Kirby, E., Rittenour, T.M., and Furlong, K.P., 2022, Differential coastal uplift quantified by luminescence dating of marine terraces, central Cascadia forearc, Oregon: Quaternary Science Reviews, v. 298, p. 107853, doi:10.1016/j.quascirev.2022.107853.

Melgar, D., 2021, Was the January 26th, 1700 Cascadia Earthquake Part of a Rupture Sequence? Journal of Geophysical Research: Solid Earth, v. 126, p. e2021JB021822, doi:10.1029/2021JB021822.

Melgar, D., Williamson, A.L., and Salazar-Monroy, E.F., 2019, Differences between heterogenous and homogenous slip in regional tsunami hazards modelling: Geophysical Journal International, v. 219, p. 553–562, doi:10.1093/gji/ggz299.

Michel, S., Gualandi, A., and Avouac, J.-P., 2019, Interseismic Coupling and Slow Slip Events on the Cascadia Megathrust: Pure and Applied Geophysics, v. 176, p. 3867–3891, doi:10.1007/s00024-018-1991-x.

Milker, Y., Nelson, A.R., Horton, B.P., Engelhart, S.E., Bradley, L.-A., and Witter, R.C., 2016, Differences in coastal subsidence in southern Oregon (USA) during at least six prehistoric megathrust earthquakes: Quaternary Science Reviews, v. 142, p. 143–163, doi:10.1016/j.quascirev.2016.04.017.

Nelson, A.R., DuRoss, C.B., Witter, R.C., Kelsey, H.M., Engelhart, S.E., Mahan, S.A., Gray, H.J., Hawkes, A.D., Horton, B.P., and Padgett, J.S., 2021, A maximum rupture model for the central and southern Cascadia subduction zone—reassessing ages for coastal evidence of megathrust earthquakes and tsunamis: Quaternary Science Reviews, v. 261, p. 106922, doi:10.1016/j.quascirev.2021.106922.

Nelson, A.R., Hawkes, A.D., Sawai, Y., Horton, B.P., Witter, R.C., Bradley, L.-A., and Cahill, N., 2020, Minimal stratigraphic evidence for coseismic coastal subsidence during 2000 yr of megathrust earthquakes at the central Cascadia subduction zone: Geosphere, v. 17, p. 171–200, doi:10.1130/GES02254.1.

Nelson, A.R., Kelsey, H.M., and Witter, R.C., 2006, Great earthquakes of variable magnitude at the Cascadia subduction zone: Quaternary Research, v. 65, p. 354–365, doi:10.1016/j.yqres.2006.02.009.

Nieminski, N.M., Sylvester, Z., Covault, J.A., Gomberg, J., Staisch, L., and McBrearty, I.W., 2024, Turbidite correlation for paleoseismology: Geological Society of America Bulletin, doi:10.1130/B37343.1.

Padgett, J.S., Engelhart, S.E., Kelsey, H.M., Witter, R.C., and Cahill, N., 2022, Reproducibility and variability of earthquake subsidence estimates from saltmarshes of a Cascadia estuary: Journal of Quaternary Science, v. 37, p. 1294–1312, doi:10.1002/jqs.3446.

Padgett, J.S., Engelhart, S.E., Kelsey, H.M., Witter, R.C., Cahill, N., and Hemphill-Haley, E., 2021, Timing and amount of southern Cascadia earthquake subsidence over the past 1700 years at northern Humboldt Bay, California, USA: GSA Bulletin, v. 133, p. 2137–2156, doi:10.1130/B35701.1.

Page, W.D., and Nishenko, S., 2015, Assessment of Potential Tsuanami Runup at the Humboldt Bay Generating Station Site: PG&E Internal, 89 p.

Priest, G.R., Witter, R.C., Zhang, Y.J., Goldfinger, C., Wang, K., and Allan, J.C., 2017, New constraints on coseismic slip during southern Cascadia subduction zone earthquakes over the past 4600 years implied by tsunami deposits and marine turbidites: Natural Hazards, v. 88, p. 285–313, doi:10.1007/s11069-017-2864-9.

Priest, G.R., Zhang, Y., Witter, R.C., Wang, K., Goldfinger, C., and Stimely, L., 2014, Tsunami impact to Washington and northern Oregon from segment ruptures on the southern Cascadia subduction zone: Natural Hazards, v. 72, p. 849–870, doi:10.1007/s11069-014-1041-7.

Rogers, G., and Dragert, H., 2003, Episodic Tremor and Slip on the Cascadia Subduction Zone: The Chatter of Silent Slip: Science, v. 300, p. 1942–1943, doi:10.1126/science.1084783.

Rollins, J.C., and Stein, R.S., 2010, Coulomb stress interactions among M ≥ 5.9 earthquakes in the Gorda deformation zone and on the Mendocino Fault Zone, Cascadia subduction zone, and northern San Andreas Fault: Journal of Geophysical Research, v. 115, p. 1–19, doi:10.1029/2009JB007117.

Salaree, A., Huang, Y., Ramos, M.D., and Stein, S., 2021, Relative Tsunami Hazard From Segments of Cascadia Subduction Zone For M 7.5–9.2 Earthquakes: Geophysical Research Letters, v. 48, p. e2021GL094174, doi:10.1029/2021GL094174.

Small, D.T., and Melgar, D., 2021, Geodetic Coupling Models as Constraints on Stochastic Earthquake Ruptures: An Example Application to PTHA in Cascadia: Journal of Geophysical Research: Solid Earth, v. 126, p. e2020JB021149, doi:10.1029/2020JB021149.

Staisch, L., 2024, Sensitivity Testing of Marine Turbidite Age Estimates along the Cascadia Subduction Zone: Bulletin of the Seismological Society of America, v. 114, p. 1739–1753, doi:10.1785/0120230252.

Stone, I., Vidale, J.E., Han, S., and Roland, E., 2018, Catalog of Offshore Seismicity in Cascadia: Insights Into the Regional Distribution of Microseismicity and its Relation to Subduction Processes: Journal of Geophysical Research: Solid Earth, v. 123, p. 641–652, doi:10.1002/2017JB014966.

Tréhu, A.M., Blakely, R.J., and Williams, M.C., 2012, Subducted seamounts and recent earthquakes beneath the central Cascadia forearc: Geology, v. 40, p. 103–106, doi:10.1130/G32460.1.

Walton, M.A.L. et al., 2021, Toward an Integrative Geological and Geophysical View of Cascadia Subduction Zone Earthquakes: Annual Review of Earth and Planetary Sciences, v. 49, p. 367–398, doi:10.1146/annurev-earth-071620-065605.

Wang, P.-L., Engelhart, S.E., Wang, K., Hawkes, A.D., Horton, B.P., Nelson, A.R., and Witter, R.C., 2013, Heterogeneous rupture in the great Cascadia earthquake of 1700 inferred from coastal subsidence estimates: Journal of Geophysical Research: Solid Earth, v. 118, p. 2460–2473, doi:10.1002/jgrb.50101.

Wang, K., and Tréhu, A.M., 2016, Invited review paper: Some outstanding issues in the study of great megathrust earthquakes—The Cascadia example: Journal of Geodynamics, v. 98, p. 1–18, doi:10.1016/j.jog.2016.03.010.

Watt, J.T., and Brothers, D.S., 2020, Systematic characterization of morphotectonic variability along the Cascadia convergent margin: Implications for shallow megathrust behavior and tsunami hazards: Geosphere, v. 17, p. 95–117.

Wells, R.E., Blakely, R.J., Sugiyama, Y., Scholl, D.W., and Dinterman, P.A., 2003, Basin-centered asperities in great subduction zone earthquakes: A link between slip, subsidence, and subduction erosion? Journal of Geophysical Research: Solid Earth, v. 108, doi:10.1029/2002JB002072.

Wells, R.E., Blakely, R.J., Wech, A.G., McCrory, P.A., and Michael, A., 2017, Cascadia subduction tremor muted by crustal faults: Geology, v. 45, p. 515–518, doi:10.1130/G38835.1.

Wilson, A., and Ma, S., 2021, Wedge Plasticity and Fully Coupled Simulations of Dynamic Rupture and Tsunami in the Cascadia Subduction Zone: Journal of Geophysical Research: Solid Earth, v. 126, p. e2020JB021627, doi:10.1029/2020JB021627.

Witter, R.C., Kelsey, H.M., and Hemphill-Haley, E., 2003, Great Cascadia earthquakes and tsunamis of the past 6700 years, Coquille River estuary, southern coastal Oregon: Geological Society of America Bulletin, v. 115, p. 1289–1306.

Witter, R.C., Zhang, Y., Wang, K., Goldfinger, C., Priest, G.R., and Allan, J.C., 2012, Coseismic slip on the southern Cascadia megathrust implied by tsunami deposits in an Oregon lake and earthquake-triggered marine turbidites: Journal of Geophysical Research: Solid Earth, v. 117, doi:10.1029/2012JB009404.

APPENDIX D

1. Review of recent Humboldt regional investigations which may have an impact on Buhne Hill and ISFSI facility

Recent investigations into components of southern Cascadia provide additional insight into evolution of the interaction between the Mendocino triple junction (MTJ) and the southern edge of the subduction zone. Several of these investigations were reported in the 2022 Pacific Cell Friends of the Pleistocene (FOP) guidebook field trip in southern Cascadia and Cape Mendocino areas (Patton et al., 2022a). They are non-peer reviewed articles, that, however present original research ranging from graduate thesis projects to US Geological Survey investigations. There are also a series of seismological investigations conducted following the 20 Dec 2021 and 20 Dec 2022 M>6 earthquakes near Petrolia and Ferndale, CA, respectively (Yeck et al., 2023; Yoon and Shelly, 2024; Shelly et al., 2024; Smith et al., 2024).

To the south, Patton and others (Patton, 2022; Patton et al., 2022b) have located an unmapped fault within southern Humboldt that may be an eastern extent of the Russ fault, a major crustal fault immediately north of Cape Mendocino.

Farther south, two Cal Poly Humboldt MS and two BS senior thesis investigations and a study from University of Glasgow were conducted adjacent to the MTJ to address coastal deformation rates and fluvial geomorphology related to MTJ migration. (Crawford et al., 2022; Hartshorn et al., 2022; Robinson et al., 2022; Vermeer and Hemphill-Haley, 2022). McPherson et al (2022) considered the seismological implications of more than 40 years of M>5 earthquakes in the MTJ region.

1.1 Crustal faults associated with the Little Salmon fault zone

The crustal faults of the accretionary prism in southern Cascadia have received new attention in the past few years. Two MS thesis investigations from Cal Poly Humboldt investigated the Little Salmon, and associated Goose Lake and Van Duzen faults (Bold and Michalak, 2022; Nicovich et al., 2024). Several trenches were excavated across the Little Salmon and Goose Lake faults as part of a CGS NEHRP-funded investigation (Ladinsky et al., 2022b, 2022a). These faults were first investigated by Woodward-Clyde (1980). In addition, a USGS investigation considered the interseismic loading strain budget of the Little Salmon and Mad River fault zones regarding regional strain (Materna et al., 2022).

Bold and Michalak (2022) investigated formation and subsequent deformation of a series Yager Creek and Van Duzen River terraces in the vicinity of Hydesville, that are crossed by the Goose Lake fault (GSL) and are adjacent to the Little Salmon fault (LSF) southeast of Buhne Hill (Figure 1). They construct detailed geomorphic maps of the terraces from lidar DEM's (Figure 2). They concluded that older, higher Van Duzen terraces have steeper tread surfaces than those formed along Yager Creek and that the Yager Creek surfaces are offset by the GSL but not the Van Duzen terraces. Radiocarbon, OSL and Beryllium-10 (^{10}Be) provide a range of ages for the surfaces of ~8.8 (Qt7) to 46 ka (Qt18). They estimate a long-term vertical slip rate for the GSL of 0.03 to 0.87 mm/yr but an incision rate of 2.3 to 5.2 mm/yr.

Ladinsky (2022b) excavated a trench across a 6 m-high scarp associated with a splay of the Goose Lake fault (Figure 1) near a previous excavation by Woodward-Clyde (1980) across the Yager Creek surfaces identified by Bold and Michalak (2022). The trench revealed faulted and strongly deformed slack water, pond and fluvial deposits (Figure 3) across a ~2m wide deformation zone. OSL samples collected in two faulted alluvial units provide age estimates of 22.4 ± 2.0 ka and 30.95 ± 2.76 ka ages for the faulted units.

However, there is not a minimum limiting age for a capping unit (which appears to be eroded and not preserved in the geologic record).

Ladinsky et al (2022a) also excavated splays of the Little Salmon fault at a location farther to the southeast of the Goose Lake site (Figure 1). Those trenches exposed thrust faults that abut interpreted Hookton Formation deposits over younger alluvial deposits (Figure 4). Radiocarbon and OSL age estimates allow them to interpret the most recent event (MRE) of possibly 990 to 1570 cal yrs BP, with enough uncertainty that it may be slightly younger.

Ladinsky et al. (2022a) constructed a photo-lineament map of the hills to the southeast of Yager Creek (Figure 1) to reveal distributed fault splays over 1km wide in the southwest facing hillside that are likely the manifestations of nearly vertical bedding plane faults with uphill facing scarps (Figure 5).

Nicovich et al (2024) investigated and mapped a suite of deformed late Pleistocene fluvial terraces along the Van Duzen River, near its confluence with the Eel River to better understand the extent and distribution of active faulting associated with the Little Salmon fault (Figure 6). They identified faulting deforms all but the most active fluvial deposits and refer to this fault as the Van Duzen fault, a southern splay of the LSF (Figure 6c). Progressively increasing scarp heights in older terraces attest to continued fault activity (Figure 6d). Based on assumptions of uplift and erosion rates estimated at other, nearby locations, they estimate the terraces span about 43 k.y. with the youngest being about 3 ka. They estimated a vertical slip rate of 0.06 to 0.38 mm/yr. They were unable to document lateral slip.

Materna et al (2022) analyzed interseismic geodetic velocities across a swath of crustal faults that include the Little Salmon fault zone (LSF) and Mad River fault zone (MRF) (Figure 7) to constrain slip rates. They constructed a visco-elastic model of the upper plate fault region considering geologic slip evidence (Figure 7b). The result is the San Andreas fault system of the San Andreas, Maacama and Bartlett Springs faults enter into southern Cascadia with about 45 mm/yr of dextral shear (Figure 7c). They model about 4 mm/yr of reverse slip on the LSF and MRF. They also model about 11 mm/yr of dextral shear through the area but cannot resolve where it is located within the forearc faults. They also conclude that interseismic coupling of the subduction zone must be almost complete with 40 mm/yr of the convergence rate stored within the upper 25 km of the megathrust in order to satisfy the level information (Patton et al., 2017). They resolve that about 20% of the 40 mm/yr (about 8 mm/yr) must be accounted for within the LSF and MRF and, additionally, some portion of the transform dextral shear penetration into southern Cascadia (Figure 8) which is in agreement with dextral shear modeled by McKenzie and Furlong (2021).

1.2 Cape Mendocino

Farther south, a series of investigations considered marine terrace formation and vertical land motion in the vicinity of coseismic uplift associated with the 1992 M6.6 and M7 earthquakes near Cape Mendocino (Crawford et al., 2022; Hartshorn et al., 2022; Vermeer and Hemphill-Haley, 2022). Additionally, Robinson et al. (2022) conducted geomorphic analysis of the response of the nearby Mattole River and its response to migration associated uplift of the Mendocino Triple Junction.

Vermeer and Hemphill-Haley (2022) conducted geodetic reoccupation of post-1992 level survey sites. They also estimated relative sea level change by a) comparing current intertidal growth positions relative to post-earthquake photos, b) evaluated current growth positions of sea urchins relative to 1992 positions, and c) compared 1992 intertidal photos to current photos. They were examining the amount of post-seismic recovery that had occurred. The idea being that if this was part of the rapidly converging subduction zone, the first 30 years might record appreciably interseismic loading. Instead, they found an

almost immeasurable recovery among all four investigative techniques. They hypothesize that this might suggest the earthquake occurred on a smaller, low slip rate fault.

During related investigations, Hartshorn et al. (2022) and Crawford et al. (2022) mapped portions of the coast that included the 1992 M7 related uplift at Singley Flat/Devils Gate, and also the area to the north at Bear River and Cape Ranch located immediately north of Cape Mendocino (Figure 9). They identified suites of marine terraces, including the 1.5 m high 1992 coseismically formed strath terrace. Using lidar data Crawford et al. (2022) focused on the area that uplifted in 1992 along with a section to the south, both south of Cape Mendocino. They identified 6 terraces above the 1992 surface, similar to those mapped by Merritts (1996) but included additional surfaces (Figure 10). The terrace risers were all about the same height as the 1992 event thus leading to the question if they represent a series of 1992-like events in the Holocene. Based on assumptions of terrace ages Crawford et al. (2022) interpreted a vertical slip rate, at this location, of 2.7 – 2.9 mm/yr.

Hartshorn et al. (2022) investigated the area north of Cape Mendocino, which also, did not have uplift in 1992. They identified only two Holocene terraces in this area at 16 and 20 m elevation having ~10 m-high risers. They speculate that the absence of multiple Holocene terraces of 1.5 m height might indicate 1992-like ruptures are limited to south of Cape Mendocino, and that uplift mechanisms here are different (see Figure 11 for comparison profile).

1.3 Seismology

There are also a series of seismological investigations conducted following the 20 Dec 2021 and 20 Dec 2022 M>6 earthquakes near Petrolia and Ferndale, CA, respectively (Yeck et al., 2023; Yoon and Shelly, 2024; Shelly et al., 2024; Smith et al., 2024)

On 20 December 2021 two earthquakes occurred separated by 11 seconds near Petrolia, the first M6.1 was located near the Mendocino fault (Figure 12), the second, M6.0, was located deeper and 30 km to the north (Yoon and Shelly, 2024). Exactly 1 year later, on 20 December 2022, a M6.4 event occurred near Fortuna causing considerable local damage. Shake maps with PGA for the 2021 M6.0 and 2022 M6.4 earthquakes, (Figures 13 and 14), respectively, show the difference in shaking that occurred near Buhne Hill as a result of these events. Several investigations were conducted to understand the spatial and temporal associations between these three earthquakes and their association with the Gorda plate (all were located within that plate), the MTJ and Cascadia megathrust.

McPherson et al. (2022) posit that earthquakes like the 1992 M7 and associated smaller events are part of a block that is moving upward and toward the west as a result of being impinged by the subduction zone to the north.

FIGURES

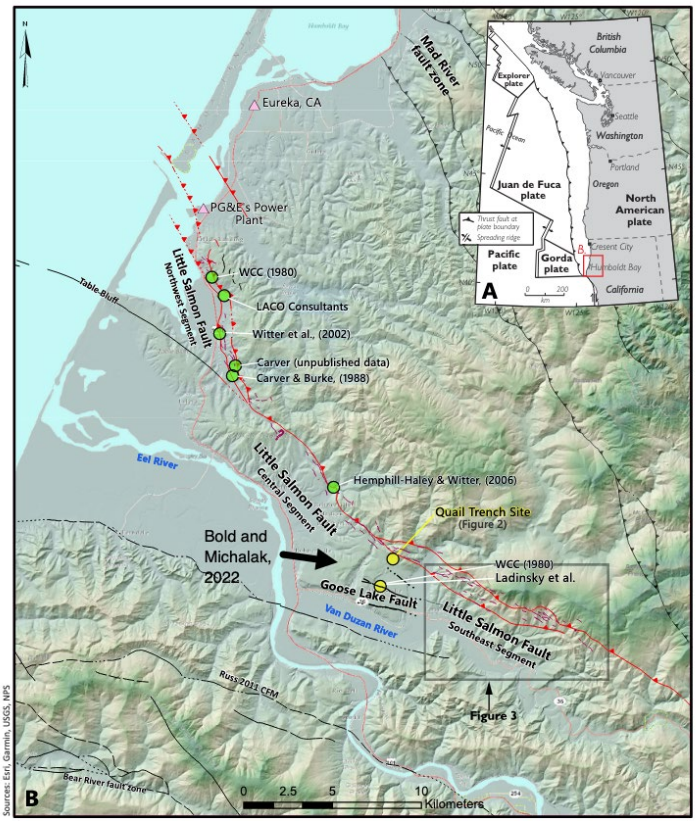

Figure 1 – Location of paleoseismic investigations along the Little Salmon fault including Bold and Michalak (2022) and Ladinsky et al. (2022), from Ladinsky et a. 2022, their figure 1.

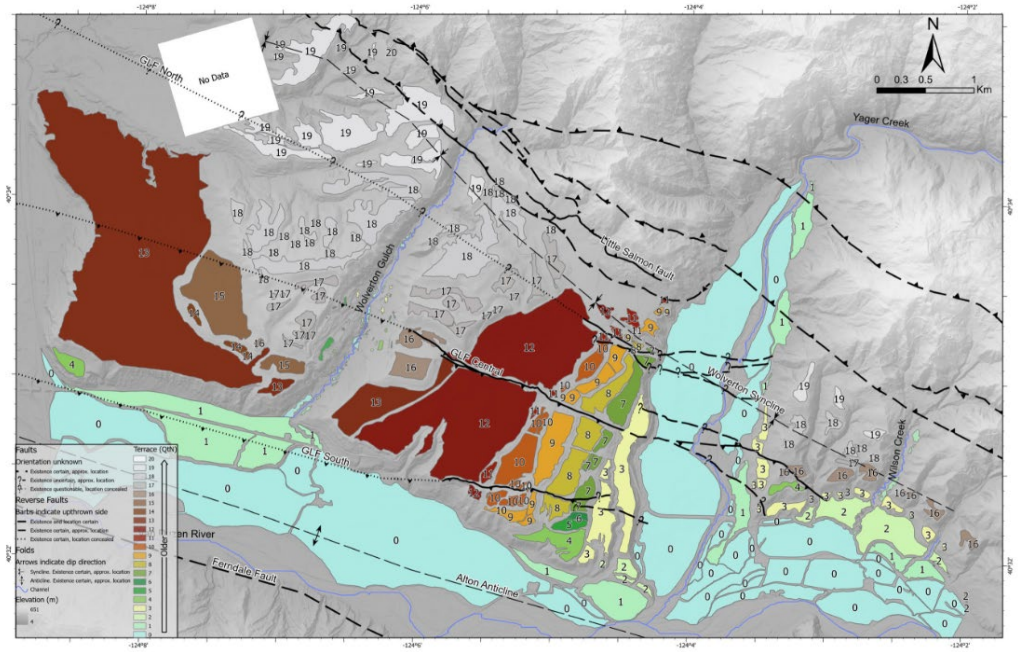

Figure 2 – Twenty fluvial terrace surfaces and traces of the Little Salmon and Goose Lake faults (from Bold and Michalak, 2022, their Figure 2).

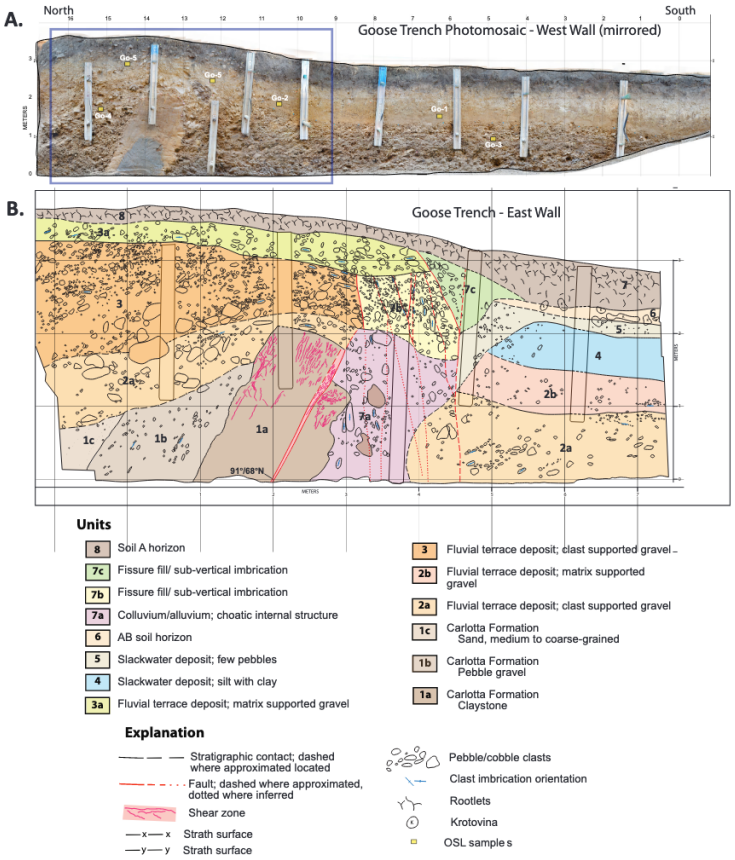

Figure 3 – Goose Lake trench photomosaic and interpretation of a portion of the trench (Ladynski et al. 2022b, their Figure 3).

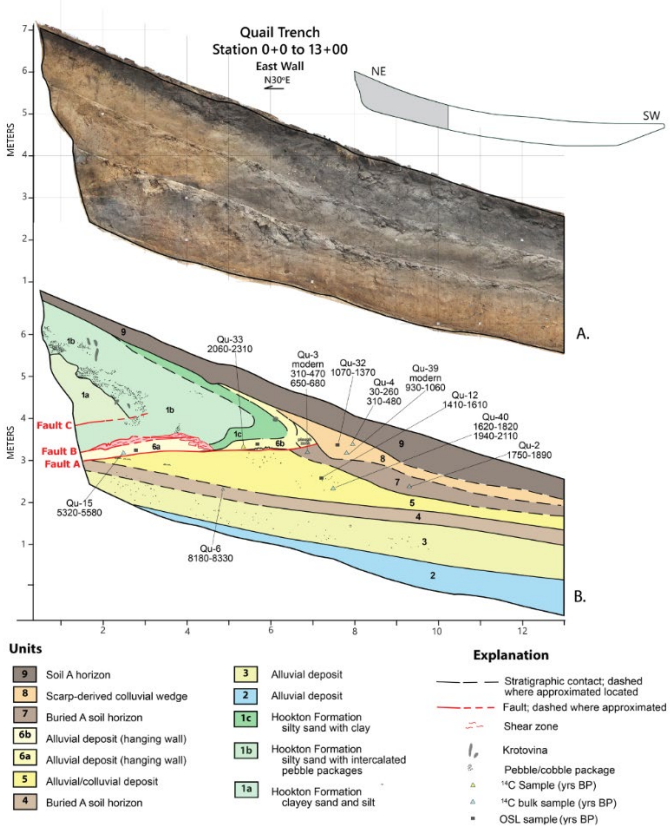

Figure 4 – Photomosaic and interpreted log of the Quail trench along a splay of the Little Salmon fault (Ladinsky, 2022a, their Figure 5).

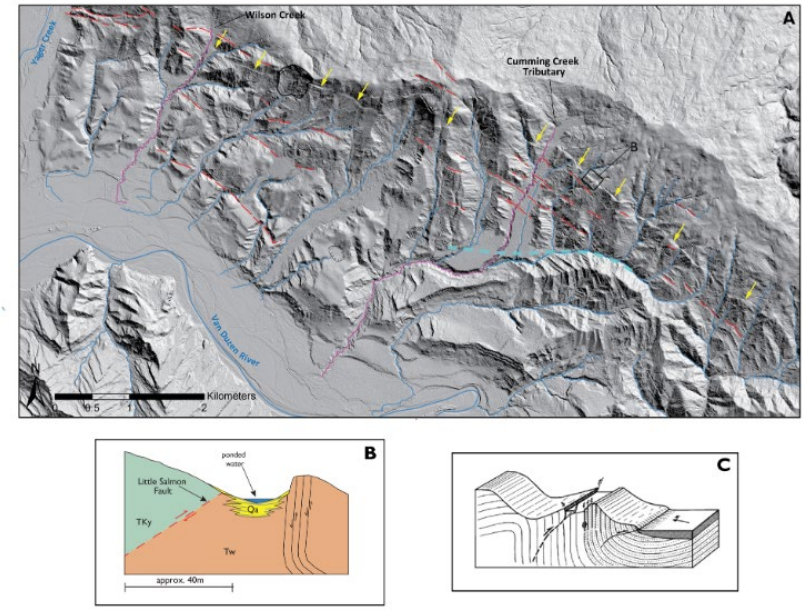

Figure 5 – Topo-lineament map based on a lidar DEM (Ladinsky et al. 2022a, their Figure 3). They interpret red lines to represent downhill and uphill facing scarps formed by bedding plane normal faults in steeply dipping sediments of Tertiary Wildcat Formation. The lineaments are associated with 5 to 50 m wide benches. Northeast-facing scarps are up to 4 m high and southeast-facing scarps are 3m to <10 m high. They interpret these scarps to be largely within a fold created by the larger LSF to the northeast.

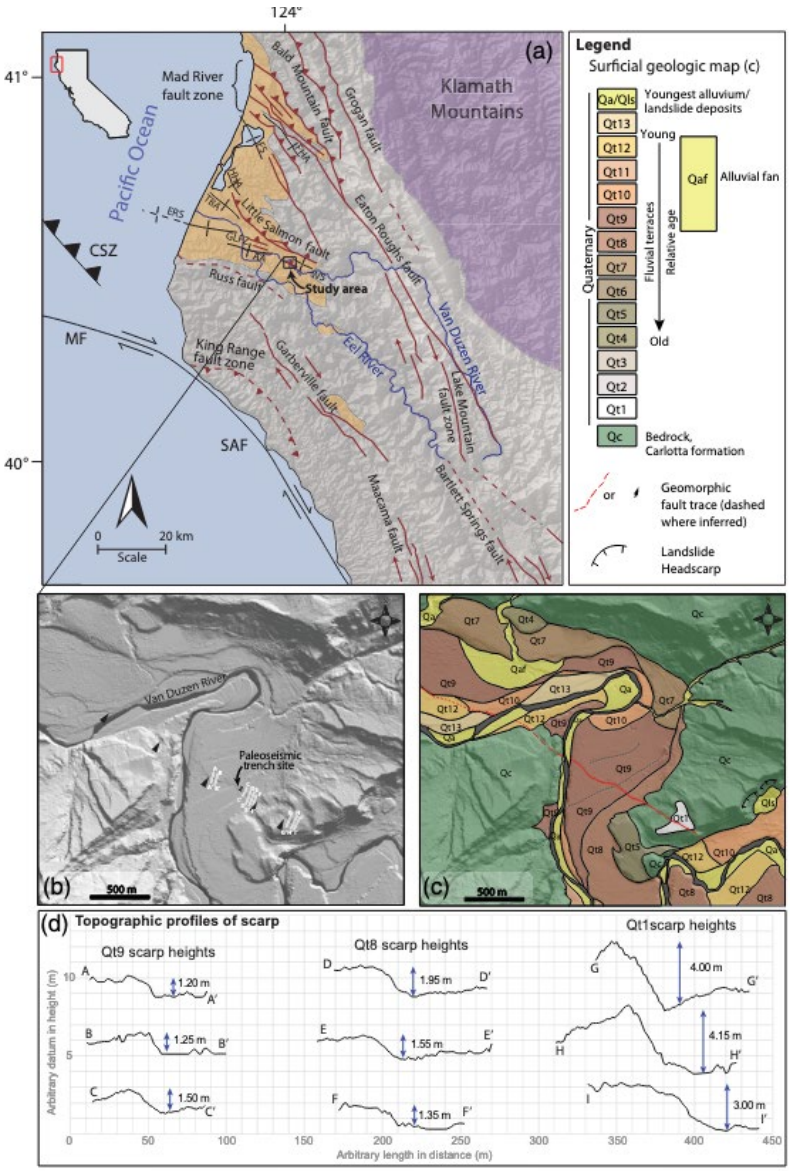

Figure 6 – Location map and geomorphic maps of the Van Duzen fault and river south of the LSF (Nicovich et al., 2024, their Figure 1). (a) Location map, (b) uninterpreted lidar DEM of study site along with location of hand-dug trench, (c) geomorphic map of terraces and fault (red line), (d) topographic profiles across various age terrace surfaces (youngest to oldest – left to right).

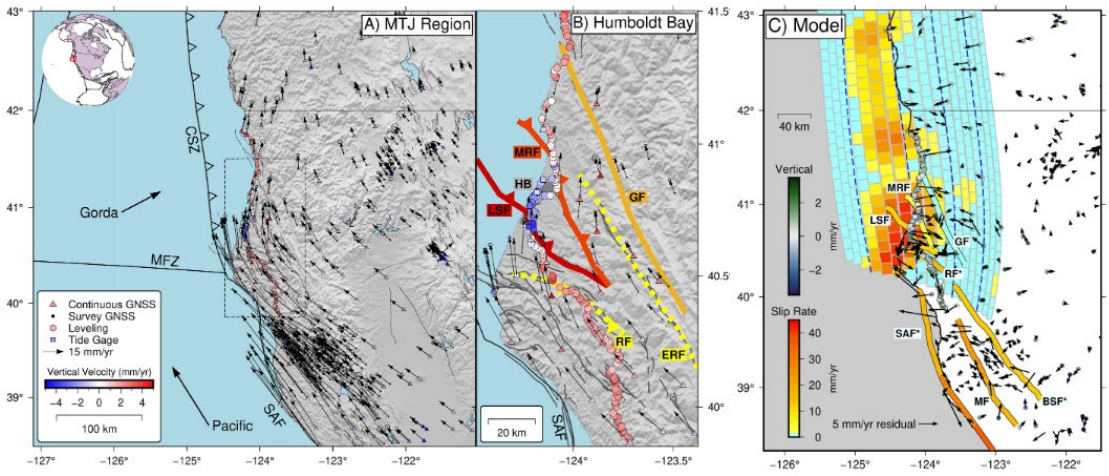

Figure 7 – A) Composite GPS velocities for northwestern CA and southern OR from Materna et al. (2022) their Figure 1. B) Investigation region including Grogan fault (GF), Eaton Roughs fault (ERF), Mad River fault zone (MRF), Little Salmon fault zone (LSF) and Russ fault (RF). Humboldt Bay (HB). Color codes are coolest (lowest activity) to warmest (highest activity). Bluish to pink dots are survey sites from Patton et al. (2017) and represent vertical velocities. Legend is in the corner of Figure 7A. C) Best fitting slip rates (colored traces).

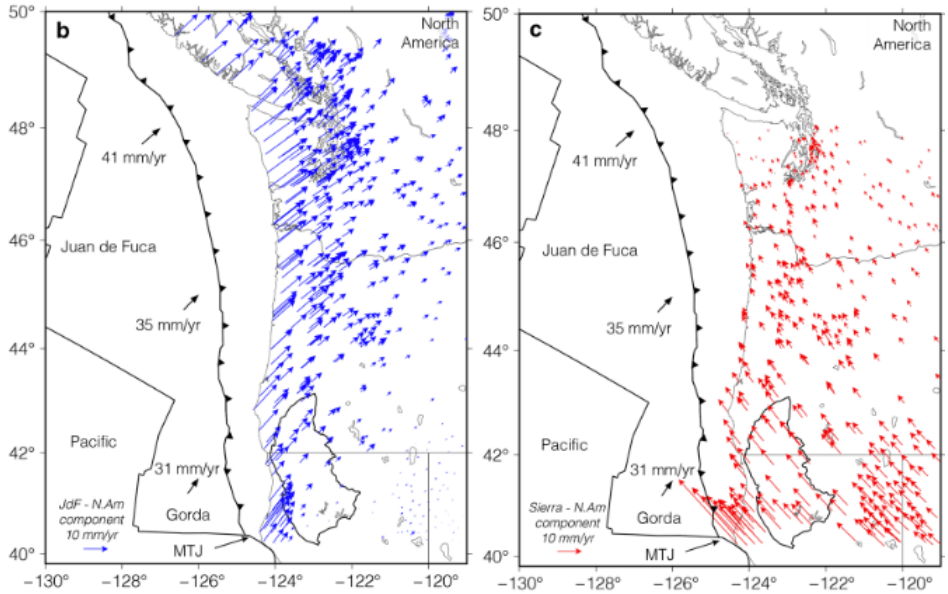

Figure 8 – Geodetic velocities of Cascadia (from McKenzie and Furlong, 2021, their Figure 3b) plate convergence parallel motion showing extent of coupling across the subduction zone, b) northwest-directed motion diminishing to the north and east indicating dextral shear and contraction.

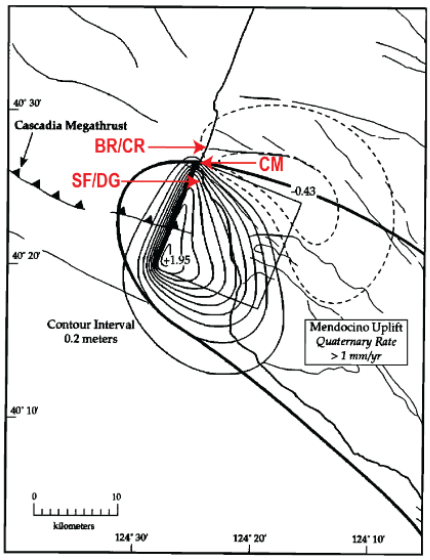

Figure 9 – Map of contours of coseismic uplift (solid lines) and subsidence (dashed lines) associated with the 1992 M7 earthquake - contours from, Murray et al. (1996) with investigation areas of Hartshorn et al. (2022) and Crawford et al. (2022). SF/DG – Singley Flat/Devils Gate, BR/CR – Bear River/Cape Ranch, CM – Cape Mendocino. Hartshorn's investigation was on the BR/CR and DG portion while Crawford principally investigated SF and DG.

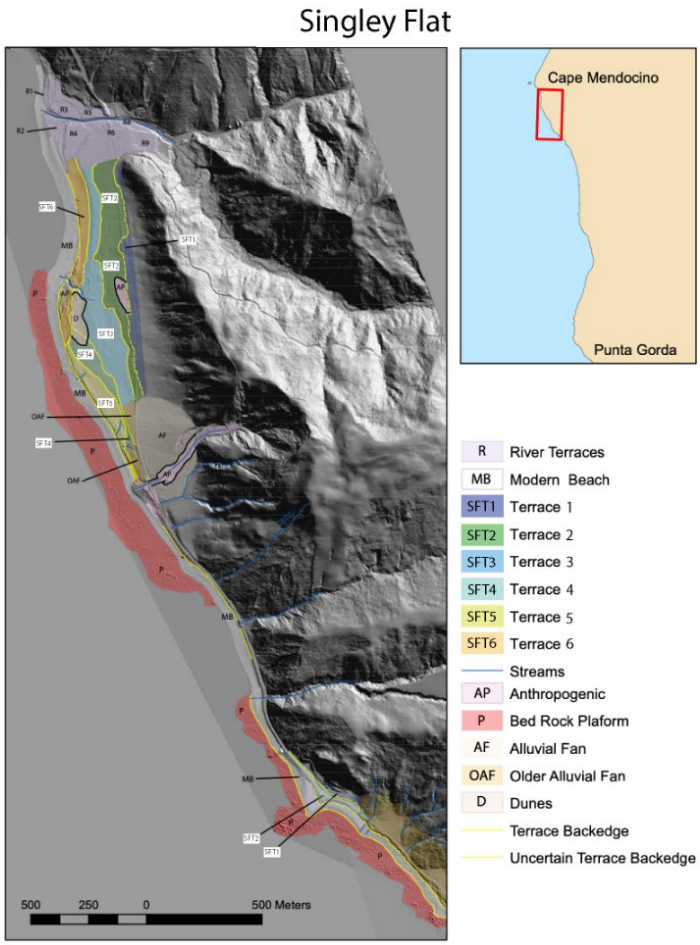

Figure 10 – Geomorphic map at Singley Flat from Crawford et al. (2022, their Figure 2).

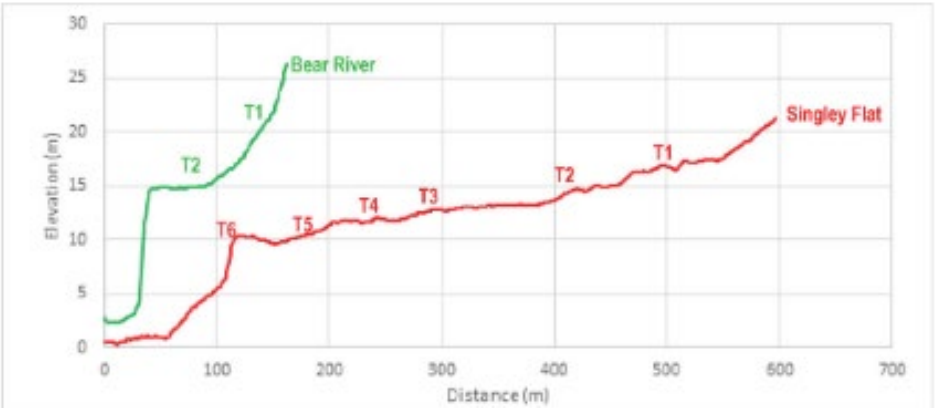

Figure 11 – Topographic profiles at Bear River (north of Cape Mendocino) and Singley Flat to the south of the cape (From Hartshorn et al., 2022, their Figure 2).

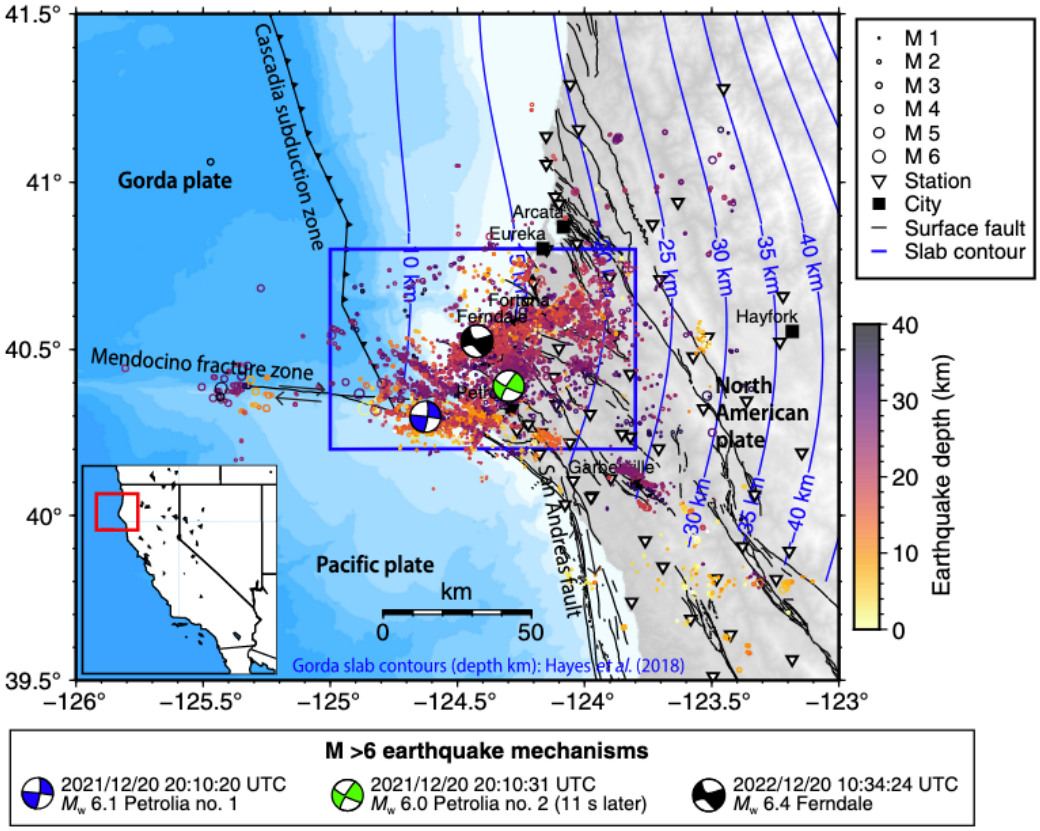

Figure 12 – 20 Dec 2021 and 2022 earthquakes near and north of the Mendocino triple junction (from Yoon and Shelly, 2024, their Figure 1).

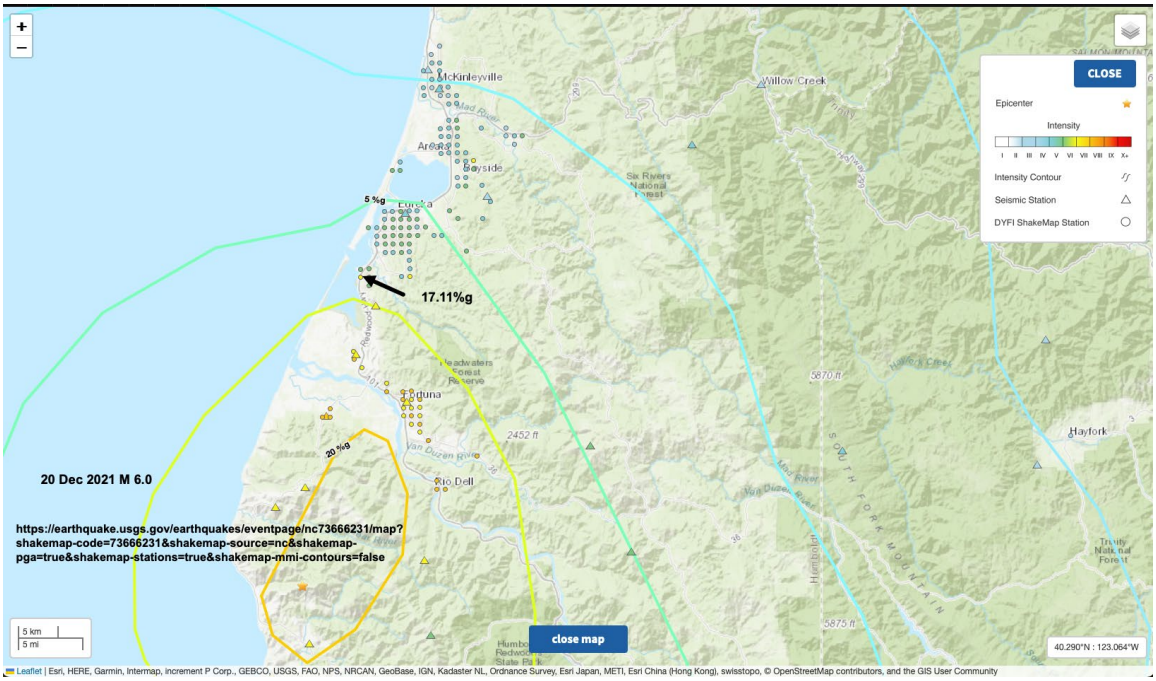

Figure 13 – 20 December 2021 M6.0 earthquake and PGA near Buhne Hill. From USGS https://earthquake.usgs.gov/earthquakes/eventpage/nc73666231/map?shakemap-code=73666231&shakemap-source=nc&shakemap-pga=true&shakemap-stations=true&shakemap-mmi-contours=false

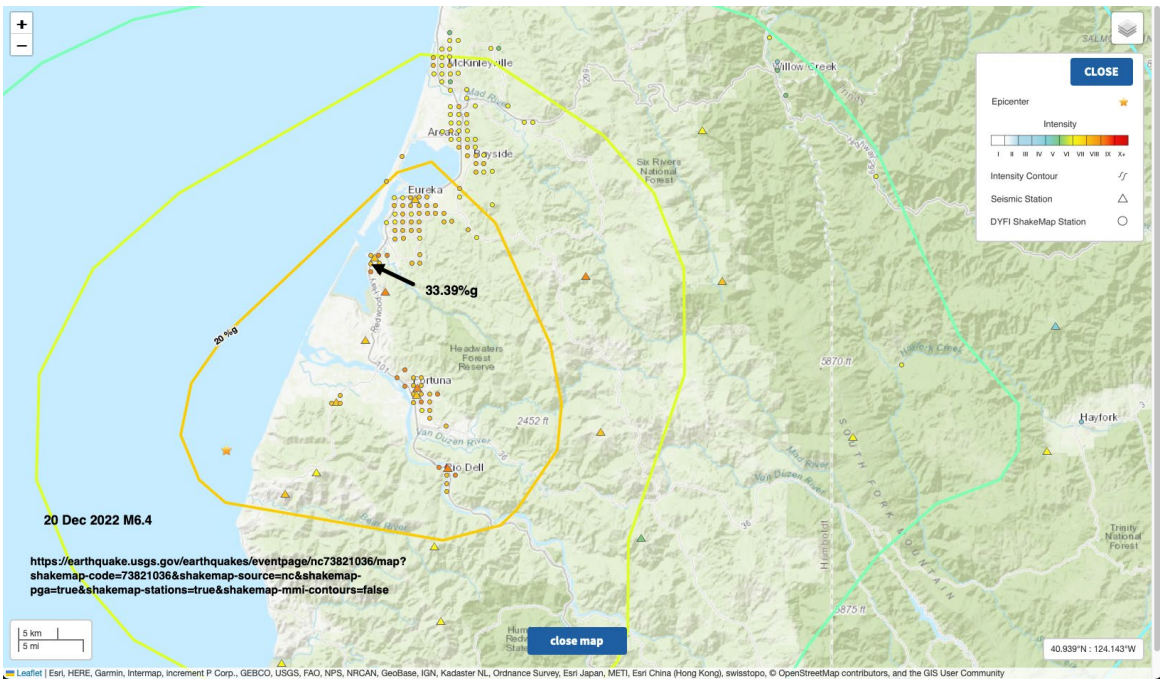

Figure 14 – 20 December 2022 M6.4 earthquake and PGA near Buhne Hill. From USGS https://earthquake.usgs.gov/earthquakes/eventpage/nc73821036/map?shakemap-code=73821036&shakemap-source=nc&shakemap-pga=true&shakemap-stations=true&shakemap-mmi-contours=false

REFERENCES

Bold, S.E., and Michalak, M.J., 2022, Incision And Deformation Of The Yager Creek–Van Duzen River Fluvial Terraces From Qua- ternary Mapping And Geochronology: Triangle of Doom V.2 - Archeology, Stratigraphy, Tectonics, Geomorphology, and Geophysics in the Region of the Mendocino Triple Junction, p. 101–108.

Crawford, B., Hartshorn, E., Hemphill-Haley, M., and Michalak, M., 2022, A New Look at Coastal Uplift and Holocene Marine Terrace Formation South of Cape Mendocino, California, *in* p. 42–49.

Hartshorn, E., Crawford, B., Hemphill-Haley, M., and Michalak, M., 2022, An Abrupt Transition: Documenting Changes in Marine Terrace Morphology Across Cape Mendocino, California: Triangle of Doom V.2 - Archeology, Stratigraphy, Tectonics, Geomorphology, and Geophysics in the Region of the Mendocino Triple Junction - FOP Guidebook, p. 50–54.

Ladinsky, T., Kelsey, H., Michalak, M., Witter, R., and Bold, S., 2022a, A Paleoseismic and Geomorphic Investigation of the Central Segment of the Little Salmon Fault, Humboldt County, CA: Triangle of Doom V.2 - Archeology, Stratigraphy, Tectonics, Geomorphology, and Geophysics in the Region of the Mendocino Triple Junction - FOP Guidebook, p. 114–130.

Ladinsky, T., Kelsey, H., Michalak, M., Witter, R., and Bold, S., 2022b, A Paleoseismic Investigation of the Goose Lake Fault, Humboldt County, CA: Triangle of Doom V.2 - Archeology, Stratigraphy, Tectonics, Geomorphology, and Geophysics in the Region of the Mendocino Triple Junction, p. 108–113.

Materna, K., Murray, J., Pollitz, F., and Patton, J.R., 2022, Interseismic Fault Loading in California's North Coast Constrained by Geodetic Data:Triangle of Doom V.2 - Archeology, Stratigraphy, Tectonics, Geomorphology, and Geophysics in the Region of the Mendocino Triple Junction - FOP Guidebook, p. 196-198.

McKenzie, K.A., and Furlong, K.P., 2021, Isolating non-subduction-driven tectonic processes in Cascadia: Geoscience Letters, v. 8, p. 10, doi:10.1186/s40562-021-00181-z.

McPherson, R.C., Patton, J.R., and Hemphill-Haley, M., 2022, A Sequence of Earthquakes Beyond the Northern San Andreas and Their Connection to Singley Flat Terraces: Triangle of Doom V.2 - Archeology, Stratigraphy, Tectonics, Geomorphology, and Geophysics in the Region of the Mendocino Triple Junction - FOP Guidebook, p. 77–82.

Merritts, D.J., 1996, The Mendocino triple junction: Active faults, episodic coastal emergence, and rapid uplift: Journal of Geophysical Research: Solid Earth, v. 101, p. 6051–6070, doi:10.1029/95JB01816.

Murray, M.H., Marshall, G.A., Lisowski, M., and Stein, R.S., 1996, The 1992 M=7 Cape Mendocino, California, earthquake: Coseismic deformation at the south end of the Cascadia megathrust: Journal of Geophysical Research: Solid Earth, v. 101, p. 17707–17725, doi:10.1029/95JB02623.

Nicovich, S.R., Hemphill-Haley, M., and Leroy, T., 2024, Deformed Latest Pleistocene Fluvial Terraces Reveal Complex Active Faulting within Tectonic Transition Zone, Mendocino Triple Junction, Northern California: The Seismic Record, v. 4, p. 62–71, doi:10.1785/0320230043.

Page, W.D., and Nishenko, S., 2015, Assessment of Potential Tsuanami Runup at the Humboldt Bay Generating Station Site: PG&E Internal, 89 p.

Patton, J.R., 2022, Tectonic Datums: Eel River Fluvial Terraces: Triangle of Doom V.2 - Archeology, Stratigraphy, Tectonics, Geomorphology, and Geophysics in the Region of the Mendocino Triple Junction - FOP Guidebook, p. 130–139.

Patton, J.R., Hemphill-Haley, M., McPherson, R.C., Micahalak, M.J., and Nicovich, S., 2022a, Triangle of Doom V2.0, Archeology, Stratigraphy, Tectonics, Geomorphology, and Geophysics in the Region of the Mendocino Triple Junction, *in* p. 235, https://www.fop.cascadiageo.org/pacific_cell/2022/2022_PAC_CEL_FOP_GUIDEBOOK.pdf (accessed September 2024).

Patton, J.R., Hemphill-Haley, M., Streig, A., and Leroy, T., 2022b, Tectonic Offset of Latest Pleistocene Fluvial Terrace Treads in Shively, Humboldt County, California: Triangle of Doom V.2 - Archeology, Stratigraphy, Tectonics, Geomorphology, and Geophysics in the Region of the Mendocino Triple Junction - FOP Guidebook, p. 140–148.

Patton, J.R., Leroy, T.H., Williams, T.B., Hemphill-Haley, M.A., McPherson, R., and Anderson, J.K., 2017, Perplexing records of coseismic subsidence; evaluation of sources for coseismic subsidence in the southern Cascadia subduction zone, Northern California: Geological Society of America, 2017 annual meeting & exposition, v. 49.

Robinson, M., Flanagan, S., and Hemphill-Haley, M., 2022, Terrace Formation in the Upper Headwater Region of the Mattole River Watershed Across the Mendocino Triple Junction, Northwest California, *in* Triangle of Doom V.2 - Archeology, Stratigraphy, Tectonics, Geomorphology, and Geophysics in the Region of the Mendocino Triple Junction - FOP Guidebook, p. 33–41.

Shelly, D.R., Goldberg, D.E., Materna, K.Z., Skoumal, R.J., Hardebeck, J.L., Yoon, C.E., Yeck, W.L., and Earle, P.S., 2024, Subduction intraslab-interface fault interactions in the 2022 M_w 6.4 Ferndale, California, earthquake sequence: Science Advances, v. 10, p. eadl1226, doi:10.1126/sciadv.adl1226.

Smith, J.A., Moschetti, M.P., and Thompson, E.M., 2024, Comparing subduction ground-motion models to observations for Cascadia: Earthquake Spectra, v. 40, p. 1787–1817, doi:10.1177/87552930241256673.

Vermeer, J., and Hemphill-Haley, M., 2022, Interseismic Lithospheric Response of the Southern End of the Cascadia Subduction Zone Since the 1992 Cape Mendocino M 7.1 Earthquake: Triangle of Doom V.2 - Archeology, Stratigraphy, Tectonics, Geomorphology, and Geophysics in the Region of the Mendocino Triple Junction - FOP Guidebook, p. 202–208.

Woodward-Clyde Consultants, 1980, Evaluation of the potential for resolving the geologic and seismic issues at the HBPP Unit No. 3: Summary to Pacific Gas and Electric company, San Francisco, CA:, 74, plus appendix p.

Yeck, W.L., Shelly, D.R., Materna, K.Z., Goldberg, D.E., and Earle, P.S., 2023, Dense geophysical observations reveal a triggered, concurrent multi-fault rupture at the Mendocino Triple Junction: Communications Earth & Environment, v. 4, p. 94, doi:10.1038/s43247-023-00752-2.

Yoon, C.E., and Shelly, D.R., 2024, Distinct Yet Adjacent Earthquake Sequences near the Mendocino Triple Junction: 20 December 2021 Mw 6.1 and 6.0 Petrolia, and 20 December 2022 Mw 6.4 Ferndale: The Seismic Record, v. 4, p. 81–92, doi:10.1785/0320230053.

APPENDIX E

1 HUMBOLDT BAY TSUNAMI HAZARD UPDATE

1.1 Tsunami Hazard Modeling Updates

New tsunami hazard modeling since Page and Nishenko (2015) and SAFFR (2013) (Figure 1) are part of a California-wide tsunami Probabilistic Tsunami Hazard Assessment (PTHA) effort by Thio (2019). That effort includes Humboldt Bay (Figures 2, 3 and 4) and is produced by the State of California at different scales for the North Coast and Humboldt Bay (State of California, 2020, 2021). It is notable that the State of California North Coast maps rely on Thio (2019) models.

California Geological Survey (California Geological Survey, 2021) and the Redwood Coast Tsunami Work Group (RCTWG, https://rctwg.humboldt.edu) produced the tsunami inundation maps shown in Figures 2 and 3.

Destructive forces of tsunamis not only include the landward force and flooding of the incoming waves, but also the erosion and deposition by backwash as debris-filled water rushes back to the ocean, typically at high flow velocities (for example in harbors inundated during the 2011 M9 Tohoku-Oki earthquake and tsunami (Udo et al., 2016) and elsewhere (Borrero et al., 2015). The combined landward flow and subsequent backwash can result in areas of coastal erosion and deposition in the nearshore as well as sediment scour in ports and harbors. Recently, numerical modeling to forecast morphodynamic changes caused by shallow water velocity currents have been conducted (Son et al., 2020). Morphodynamic effects of the inundation could have an eroding impact on Buhne Hill, particularly on the bluff side.

Far field tsunamis are a fairly frequent occurrence on the North Coast, with 33 tsunamis recorded since the installation of the first tide gauge at Crescent City in 1933 (Admire et al., 2011, 2014). To date, Humboldt Bay has not suffered damage from far field tsunamis, although higher current velocities have been recorded. In Humboldt Bay, Acoustic Doppler Current Profilers (ADCP) have been installed (Figure 5) to measure tsunami and other currents (Admire et al., 2014). The ADCP's were operational during the 2010 M8.8 Chile and 2011 M9.0 Tohoku-Oki, Japan earthquakes and were able to calculate peak tsunami wave amplitude and peak current speeds for both events (Figure 6). Admire et al. (2014) report that tsunami currents from the 2010 Chile earthquake lasted within Humboldt Bay for approximately 30 hours with peak velocities of about 1.15 ft/s (0.35 m/s) and peak water amplitudes of about 0.75 ft (0.23 m). The 2011 Japan earthquake resulted in a tsunami signal that lasted more than 40 hours in the bay with water velocities of between 2.0 and 2.8 ft/s (0.6 and 0.84 m/s) measured during the first 2 hours with a peak amplitude of 2.6 ft (0.81 m). The "Physical Oceanographic Real-time System (PORTS) project, which included some of the ADCP locations reported by Admire (2014), a collaborative effort at Humboldt Bay between NOAA and Cal Poly Humboldt (https://tidesandcurrents.noaa.gov/ports/index.html?port=hb) currently maintains a continuous monitoring system in Humboldt Bay in the event of tsunami activity to acquire "*Better estimates of the currents generated by tsunamis [which] can be used to improve numerical modeling and to provide better understanding of the hazards in ports and harbors caused by currents"* (Admire et al., 2014, p. 3402).

1.2 Probabilistic Tsunami Hazard Analysis (PTHA)

In addition to the PTHA conducted for coastal California by Thio (2019) which included Humboldt Bay (Figure 7) there have been few tsunami hazard studies specifically focused on northernmost California. However, there have been tsunami hazard evaluations conducted along other portions of the Cascadia Subduction Zone (CSZ) that are germane to Buhne Hill and the ISFSI

Goda (2023) has conducted a PTHA for Vancouver Island, Canada that considers full rupture of the CSZ using both time-dependent earthquake recurrence and stochastic rupture models. The stochastic models consider variability in fault geometry, position, and earthquake slip distribution. He concluded that coastal exposure to the subduction zone source and local bathymetry will be major contributors to variability of tsunami inundation along Vancouver Island.

Davies et al. (2018) conducted a global PTHA that included a study site near Seaside, OR, and included the CSZ as an earthquake and tsunami source. They concluded that, referenced to Mean Sea Level (MSL) a 1/100 exceedance tsunami would have peak wave heights of 16 ft (5.0 m) and a 1/500 exceedance event would have peak wave heights of 43.3 ft (13.2 m). These values are similar to an earlier PTHA conducted specifically for Seaside, OR (González et al., 2009) that estimated peak elevations of 1/100 and 1/500 exceedance of 13 ft (4 m) and 34.4 ft (10.5 m), respectively.

Sepulveda et al. (2021) consider the role of future sea level rise (SLR) in the PTHA and propose the non-stationary probabilistic tsunami hazard assessment (nPTHA) in their evaluation of hazards in the North China Sea. They consider SLR models RCP2.6, 4.5, 6 and 8.5 proposed by the Intergovernmental Panel on Climate Change (IPCC, 2022). They conclude that the impact of SLR can be significant for long-recurrence seismic sources, beyond 100 years.

There is little information about the effects of the 1964 M9.2 Prince William Sound, Alaska tsunami at Humboldt Bay, however, the NOAA National Centers for Environmental Information Natural Hazards Viewer provides some information that at Fields Landing and King Salmon water heights of 1-2 m (3 to 7 feet) were observed (Figure 8).

The associated website https://www.ngdc.noaa.gov/hazel/view/hazards/tsunami/runup-more-info/4349 provides further information about the tsunami in Humboldt Bay.

Lander et al., (1993) report that:

The Eureka Boat Basin suffered little damage but the water rose over the ten-foot seawall and eight feet into the street at the height of the rise. The tide was six feet. The bay was filled with logs and debris. Half of the sea and channel markers were moved off their stations by the surge. Nine changes in the tide were reported between midnight and 4:30 A.M. with an eight to nine feet tide at the channel entrance. "It was like someone pulled the cork out of the bay. The velocity was tremendous. It came back in just as fast and kept repeating".

The site reports that Robert Wiegel (1965) reported:

"…maximum run-up elevations above the tide stages as probably 3.1 feet at the Coast Guard Station on North Spit, about 4.7 to 5.1 feet at the Municipal Marina, Eureka about 4.5 feet at the entrance to King

Salmon Slough, and 3.8 feet at the Pacific Gas and Electric Power Plant intake (0.6 miles upstream on the King Salmon Slough.)"

The NEIC site also documents that Magoon (1965) stated that there were:

…14 knot currents in the channel opposite the Coast Guard Station. Professor Gast, Humboldt State College, estimated the ***maximum height as 14 feet (7 foot amplitude*** *based on water lines on docks and structures)."*

1.3 Updates on Tsunami Record for the North Coast at Humboldt Bay

To date, no definitive tsunami deposits have been identified at study locations along northern Humboldt Bay (Arcata Bay), which is relatively sheltered from the Pacific Ocean by intervening high sand dunes between the mouth of Humboldt Bay and the Mad River (Engelhart et al., 2016; Hemphill-Haley, 2017; Padgett et al., 2021, 2022; Pritchard, 2004).

Patton (2004) found no evidence at Hookton Slough for a tsunami deposit associated with the ~ M9.0 CSZ earthquake in 1700 C.E., and evidence for the 1700 C.E. deposit at the South Humboldt Bay sites studied by Carver et al. (1998) is possible but equivocal because of the proximity of the study sites to the ocean and overlapping radiocarbon ages with the age of destructive coastal storms in the late 19th century (e.g., Hemphill-Haley et al., 2019). Other older events are recorded the site and it is likely that the coast at Humboldt Bay was impacted by the CSZ tsunami in 1700 C.E. as there is abundant evidence for this event at coastal sites to the north at Crescent City and elsewhere in coastal Del Norte County (Abramson, 1998; Carver et al., 1998; Garrison-Laney, 1998; Hemphill-Haley et al., 2019; Peterson et al., 2011).

FIGURES

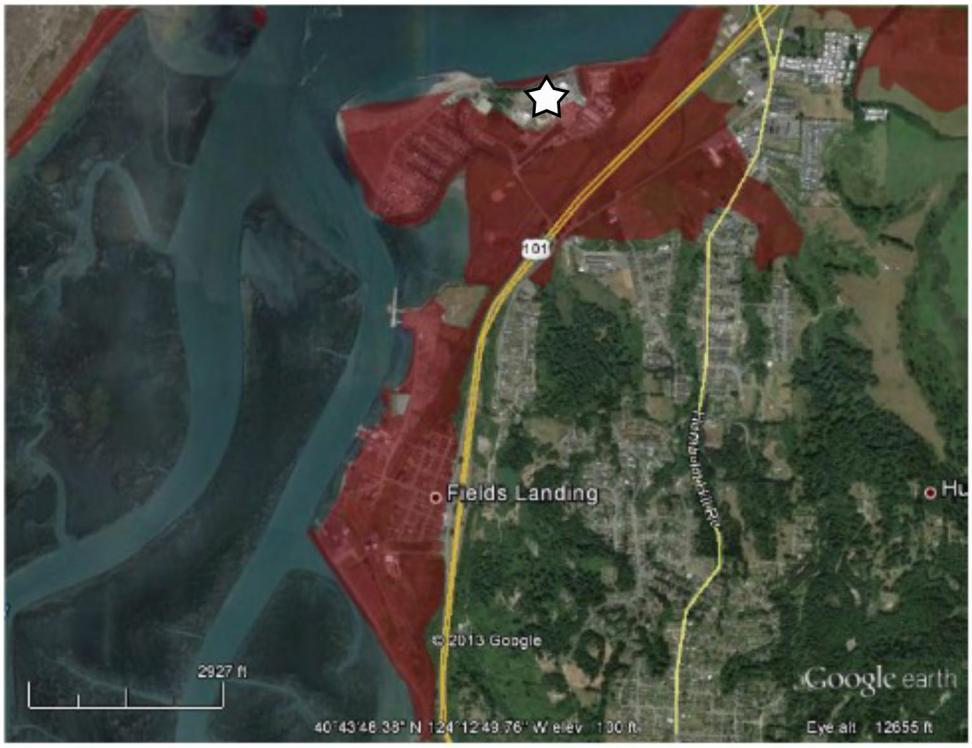

Figure 1 – Tsunami inundation map of the Fields Landing area including Buhne Point and the ISFSI site (SAFFR Tsunami Modeling Working Group, 2013). Note: Buhne Hill and the ISFSI site (white star) are not within the inundation area (red shading).

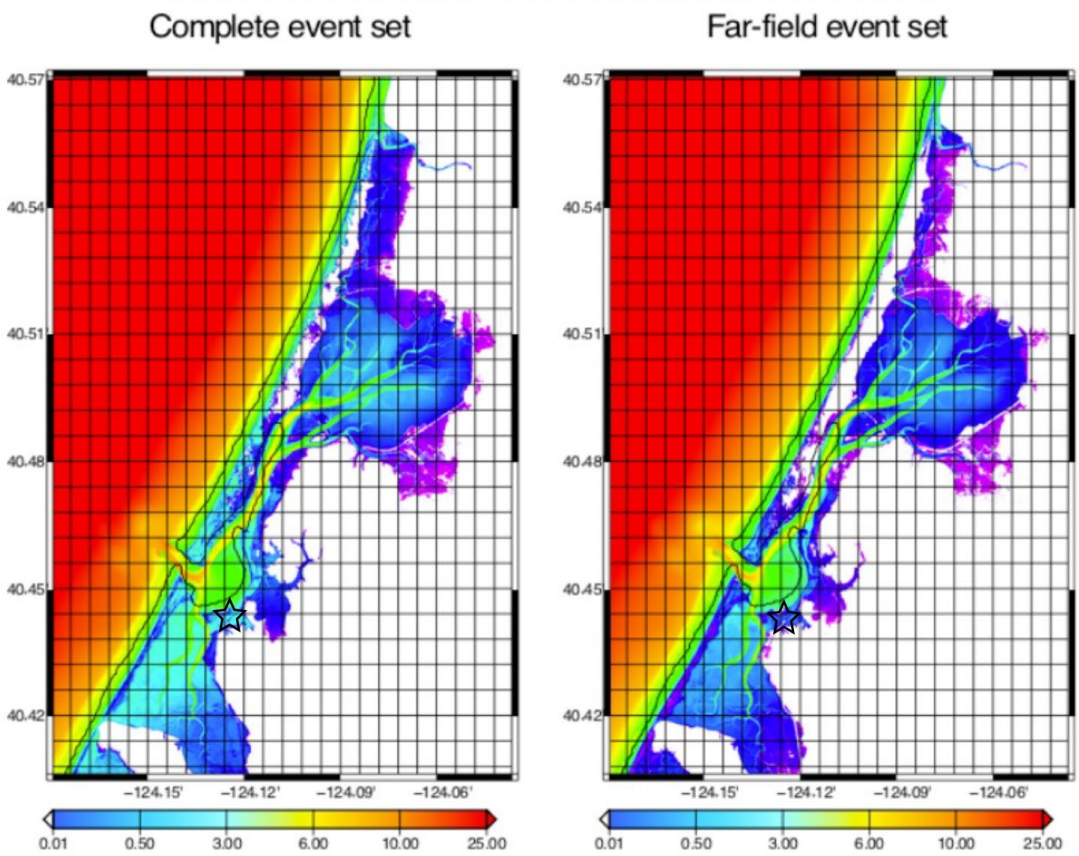

Figure 2 – Probabilistic tsunami flow depths for Humboldt Bay considering a 2475 year model (from Thio, 2019). Left map includes local and far-field sources while the map on the right considers only far-field sources. Approximate location of ISFSI depicted by open star. As noted in the report there is not substantial difference in the inundation pattern between the two source models. Elevation units are in meters.

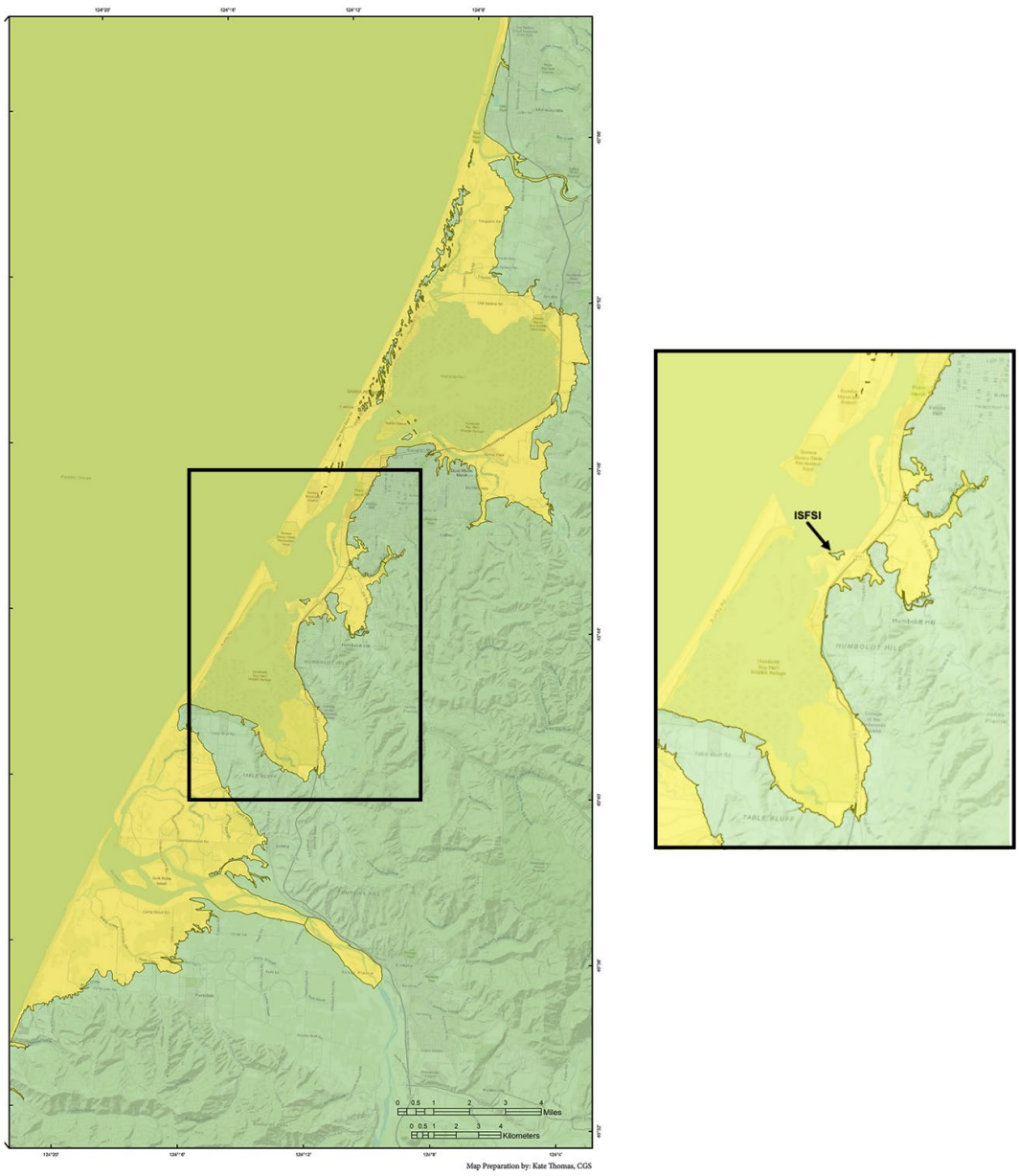

Figure 3 –Humboldt Bay tsunami inundation map (State of California, 2021). Areas highlighted in yellow are considered likely to be inundated corresponding to a 975-year average return period tsunami event model with a 5% probability of exceedance in 50 years. At this resolution it is apparent that Buhne Hill is not inundated during this scenario. This map is based on modeling by Thio (2019).

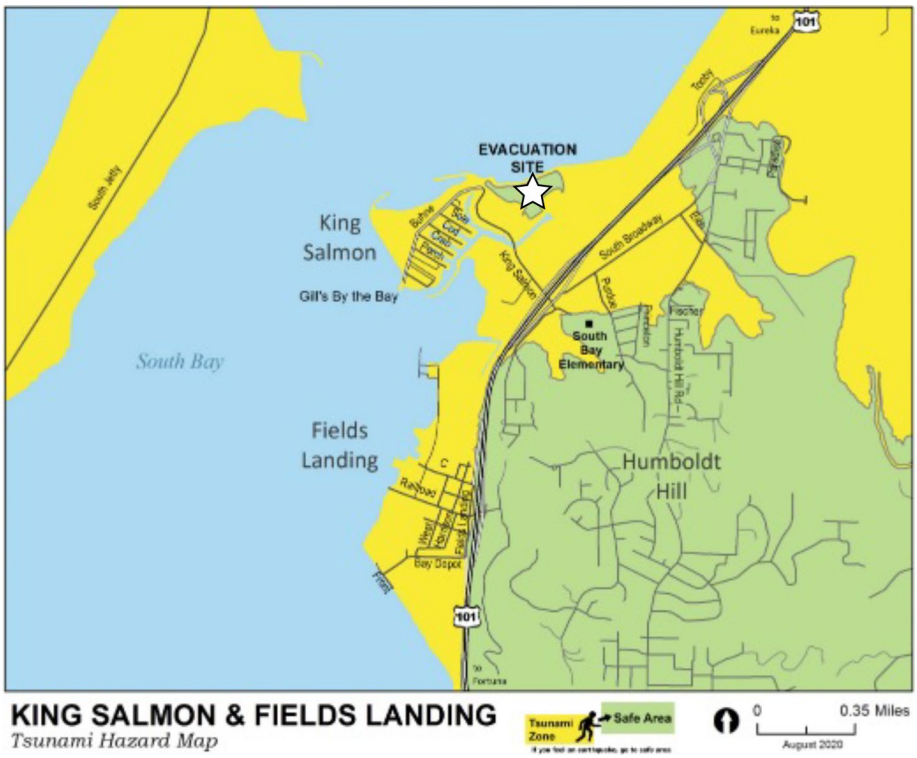

Figure 4 – Tsunami inundation map for King Salmon and Fields Landing (State of California, 2021). This map was produced in association with the Redwood Coast Tsunami Working Group (RCTWG, https://rctwg.humboldt.edu) Yellow shading indicates areas of inundation. Buhne Hill and the ISFSI site (star) are not inundated in this model and are considered a local evacuation site. Modeling is based Thio (2019).

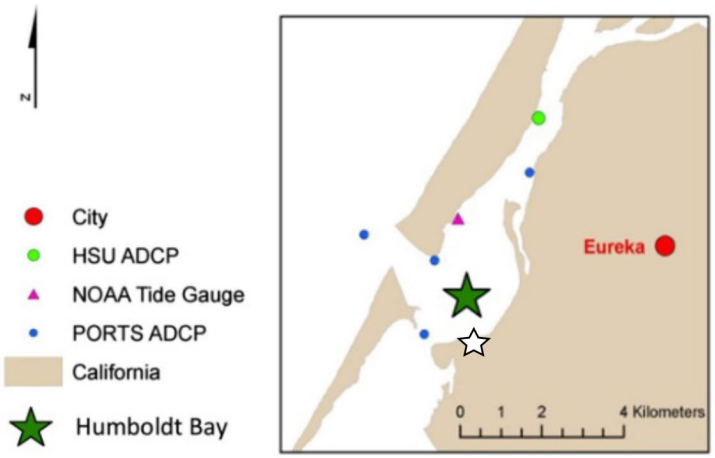

Figure 5 – Humboldt Bay with NOAA tide gauge site (pink triangle), Acoustic Doppler Current Profiler (ADCP) (green dot), and ADCP sites deployed as part of ongoing NOAA PORTS project (blue dots). White star indicates approximate location of ISFSI. Modified from Admire et al., (2014).

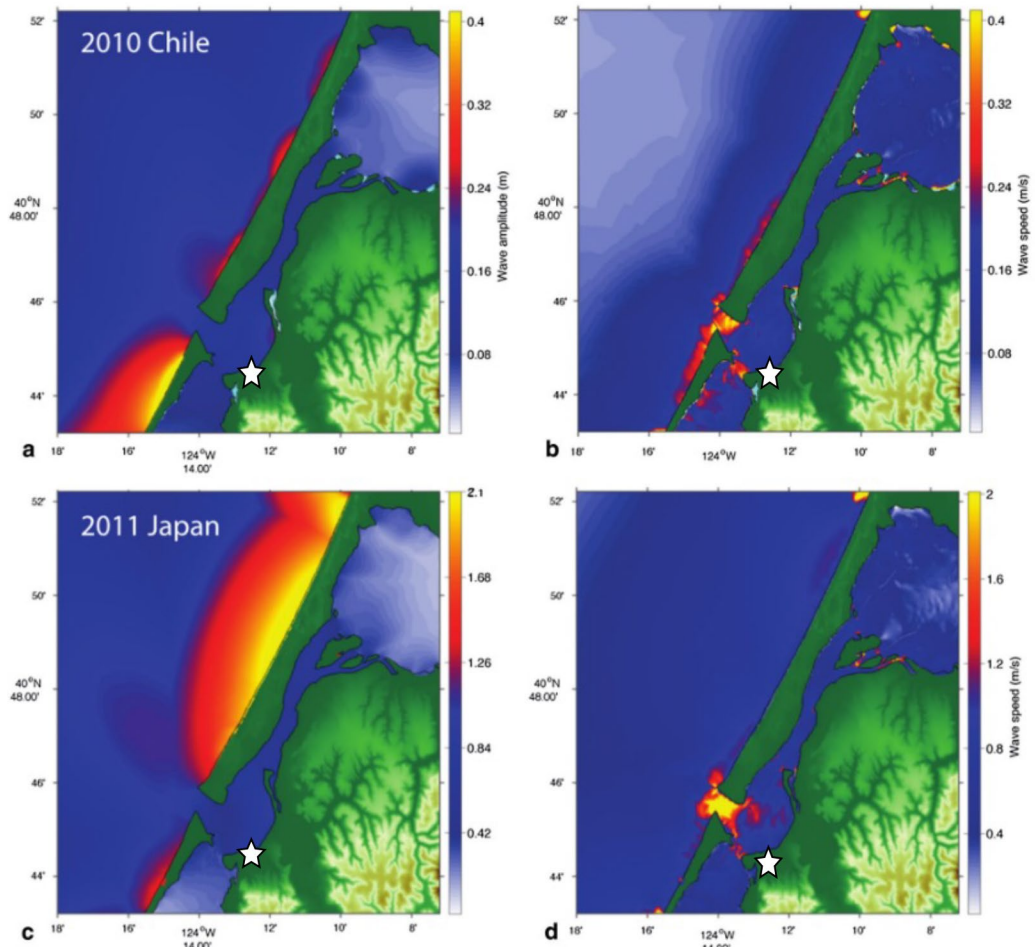

Figure 6 – Peak tsunami wave amplitudes (a, c) and peak current speeds (b, d) computed by the MOST model for the 2010 Chile and 2011 Japan tsunamis for the coast and entrance to Humboldt Bay. Amplitudes were predicted to be largest on the coastal side of the North Spit with increased currents focused at the harbor entrance (from Admire et al. (2014)).

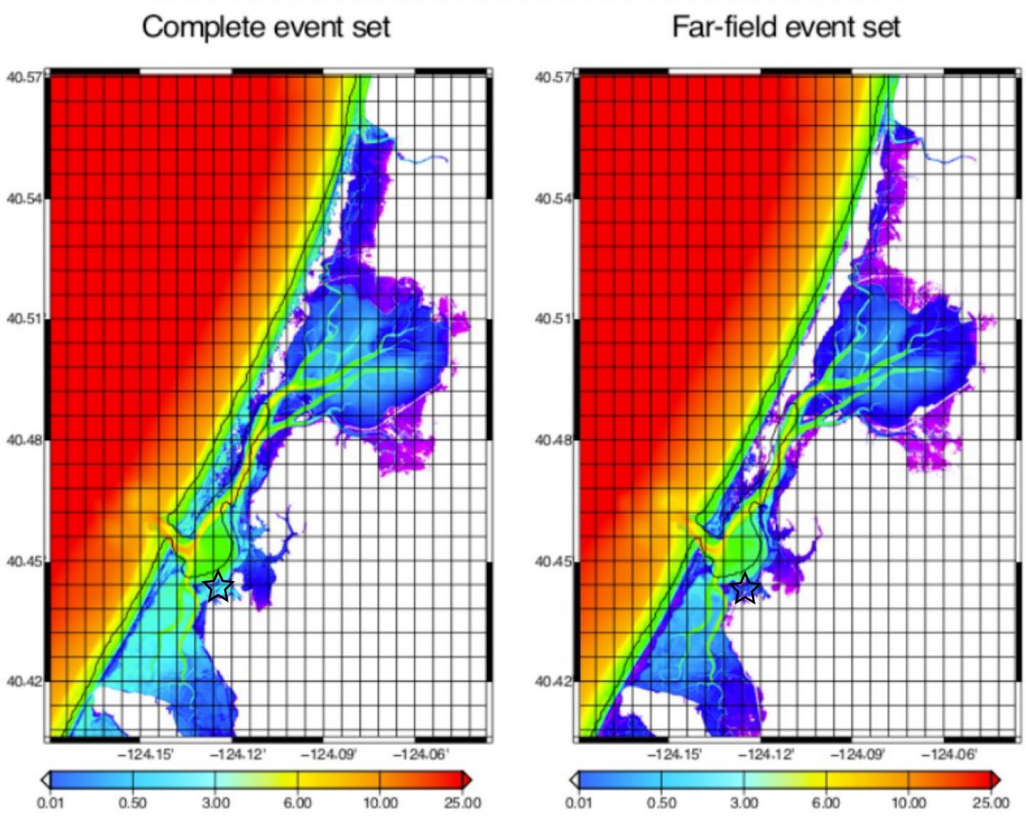

Figure 7 – Comparison of full-event, including CSZ megathrust (Left) and only far-field events (right) for a 2475 year probabilistic tsunami flow depth Heights are in meters.(Thio, 2019).

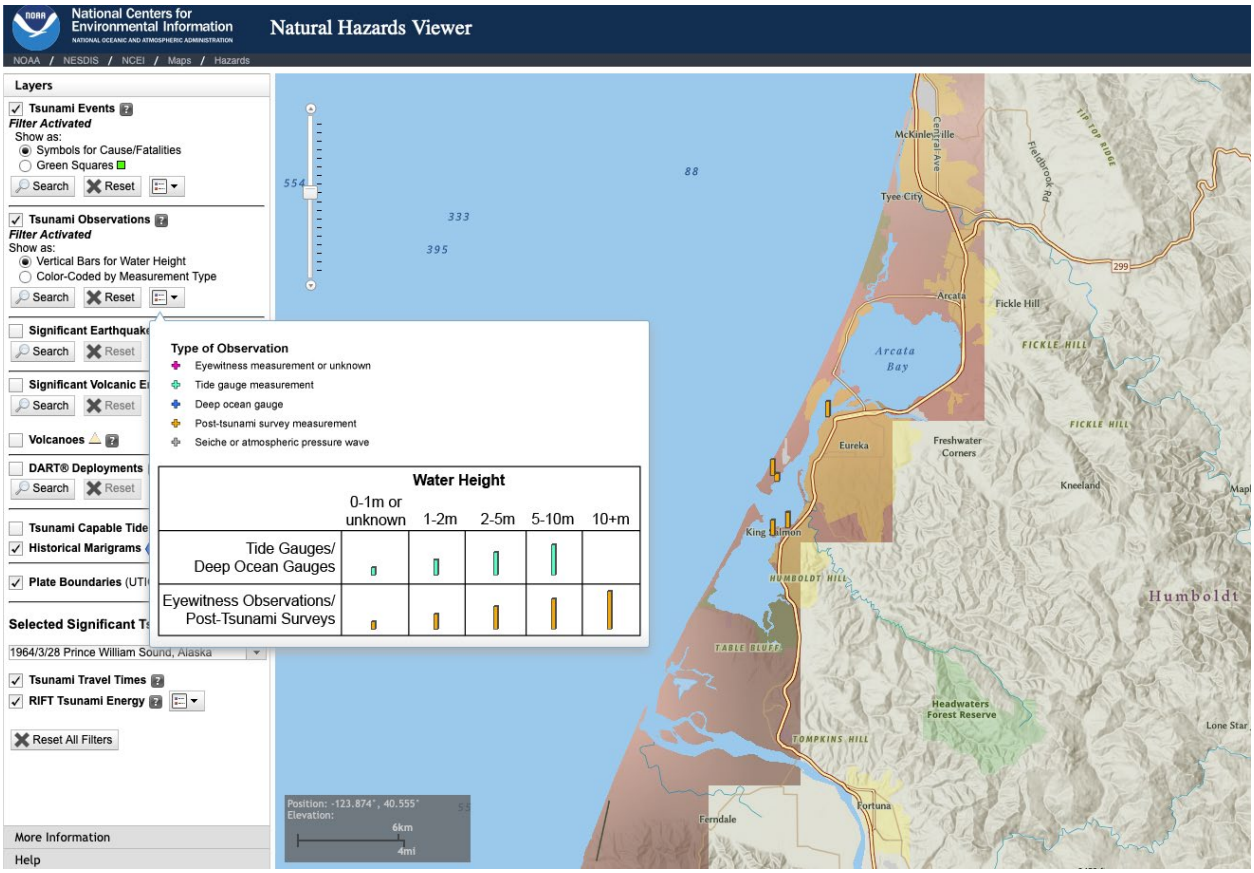

Figure 8 – Screenshot of NOAA Natural Hazards Viewer webpage showing reported wave heights at King Salmon as a result of the 1964 M9.2 Prince William Sound, Alaska earthquake https://www.ncei.noaa.gov/maps/hazards/?tsEvent=1954

References

Abramson, H. F. (1998). Evidence for tsunamis and earthquakes during the last 3500 years from Lagoon Creek, a coastal freshwater marsh, northern California [Masters Thesis]. Humboldt State University.

Admire, A. R., Dengler, L. A., Crawford, G. B., Uslu, B. U., Borrero, J. C., Greer, S. D., & Wilson, R. I. (2014). Observed and Modeled Currents from the Tohoku-oki, Japan and other Recent Tsunamis in Northern California. Pure and Applied Geophysics, 171(12), 3385–3403. https://doi.org/10.1007/s00024-014-0797-8

Admire, A. R., Dengler, L., Crawford, G., Uslu, B., Montoya, J., & Wilson, R. (2011). Observed and Modeled Tsunami Currents on California's North Coast. AGU Fall Meeting Abstracts, 03.

Bahuguna, A., Nayak, S., & Roy, D. (2008). Impact of the tsunami and earthquake of 26th December 2004 on the vital coastal ecosystems of the Andaman and Nicobar Islands assessed using RESOURCESAT AWiFS data. International Journal of Applied Earth Observation and Geoinformation, 10(2), 229–237. https://doi.org/10.1016/j.jag.2008.02.010

Borrero, J. C., Lynett, P. J., & Kalligeris, N. (2015). Tsunami currents in ports. Philosophical Transactions of the Royal Society A: Mathematical, Physical and Engineering Sciences, 373(2053), 20140372. https://doi.org/10.1098/rsta.2014.0372

California Geological Survey. (2021). California Official Tsunami Inundation Maps. California Department of Conservation. https://www.conservation.ca.gov/cgs/tsunami/maps

Carver, G. A., Abramson, H. A., Garrison-Laney, C. E., & Leroy, T. H. (1998). Investigation of paleotsunami evidence along the north coast of California (p. 238). prepared for Pacific Gas and Electric Company.

Davies, G., Griffin, J., Løvholt, F., Glimsdal, S., Harbitz, C., Thio, H. K., Lorito, S., Basili, R., Selva, J., Geist, E., & Baptista, M. A. (2018). A global probabilistic tsunami hazard assessment from earthquake sources. Geological Society, London, Special Publications, 456(1), 219–244. https://doi.org/10.1144/SP456.5

Engelhart, S. E., Hemphill-Haley, E., Kelsey, H. M., & Padgett, J. S. (2016). Refined Estimates of Coseismic Subsidence along the Southern Cascadia Subduction Zone in Northern Humboldt Bay (Arcata Bay): Collaborative Research with University of Rhode Island and Humboldt State University (NERHP Final Technical Report No. G14AP00128, G14AP00129; p. 38). U.S. Geological Survey.

Feldens, P., Schwarzer, K., Szczuciński, W., Stattegger, K., Sakuna, D., & Somgpongchaiykul, P. (2009). Impact of 2004 Tsunami on Seafloor Morphology and Offshore Sediments, Pakarang Cape, Thailand. Polish Journal of Environmental Studies, 18(1), 63–68.

Garrison-Laney, C. E. (1998). Diatom evidence for tsunami inundation from Lagoon Creek, a coastal freshwater pond, Del Norte County, California [Masters Thesis, Humboldt State University]. http://dspace.calstate.edu/handle/10211.3/140561

Goda, K. (2023). Probabilistic Tsunami Hazard Analysis for Vancouver Island Coast Using Stochastic Rupture Models for the Cascadia Subduction Earthquakes. GeoHazards, 4(3), Article 3. https://doi.org/10.3390/geohazards4030013

González, F. I., Geist, E. L., Jaffe, B., Kânoğlu, U., Mofjeld, H., Synolakis, C. E., Titov, V. V., Arcas, D., Bellomo, D., Carlton, D., Horning, T., Johnson, J., Newman, J., Parsons, T., Peters, R., Peterson, C., Priest, G., Venturato, A., Weber, J., … Yalciner, A. (2009). Probabilistic tsunami hazard assessment at Seaside, Oregon, for near- and far-field seismic sources. Journal of Geophysical Research: Oceans, 114(C11). https://doi.org/10.1029/2008JC005132

Hazarika, H., Kasama, K., Suetsugu, D., Kataoka, S., & Yasufuku, N. (2013). Damage to Geotechnical Structures in Waterfront Areas of Northern Tohoku Due to the March 11, 2011 Tsunami Disaster. Indian Geotechnical Journal, 43(2), 137–152. https://doi.org/10.1007/s40098-012-0021-7

Hemphill-Haley, E. (2017). Observations on the distributions of modern benthic diatoms to improve estimates of past coseismic land-level changes, Humboldt Bay, California. Seismological Research Letters, 8(2B). https://www.seismosoc.org/wp-content/uploads/2018/09/srl-2017035.1.pdf

Hemphill-Haley, E., Kelsey, H. M., Graehl, N., Casso, M., Caldwell, Loofbourrow, C., Robinson, M., Vermeer, J., & Southwick, E. (2019). Recent sandy deposits at five northern California coastal wetlands—Stratigraphy, diatoms, and implications for storm and tsunami hazards (USGS Numbered Series Nos. 2018–5111; Scientific Investigations Report, p. 187). U.S. Geological Survey. http://pubs.er.usgs.gov/publication/sir20185111

IPCC. (2022). The Ocean and Cryosphere in a Changing Climate: Special Report of the Intergovernmental Panel on Climate Change. Intergovernmental Panel on Climate Change. https://doi.org/10.1017/9781009157964

Lander, J. F., Lockridge, P. A., & Kozuch, M. J. (1993). Tsunamis Affecting the West Coast of the United States, 1806-1992 (No. 29; NGDC Key to Geophysical Records, p. 254). National Oceanic and Atmospheric Administration.

Magoon, O. T. (1965). Structural Damage by Tsunamis. American Society of Civil Engineers Specialty Conference on Coastal Engineering, 35–68.

McAdoo, B. G., Ah-Leong, J. S., Bell, L., Ifopo, P., Ward, J., Lovell, E., & Skelton, P. (2011). Coral reefs as buffers during the 2009 South Pacific tsunami, Upolu Island, Samoa. Earth-Science Reviews, 107(1), 147–155. https://doi.org/10.1016/j.earscirev.2010.11.005

Padgett, J. S., Engelhart, S. E., Kelsey, H. M., Witter, R. C., & Cahill, N. (2022). Reproducibility and variability of earthquake subsidence estimates from saltmarshes of a Cascadia estuary. Journal of Quaternary Science, 37(7), 1294–1312. https://doi.org/10.1002/jqs.3446

Padgett, J. S., Engelhart, S. E., Kelsey, H. M., Witter, R. C., Cahill, N., & Hemphill-Haley, E. (2021). Timing and amount of southern Cascadia earthquake subsidence over the past 1700 years at northern Humboldt Bay, California, USA. GSA Bulletin, 133(9–10), 2137–2156. https://doi.org/10.1130/B35701.1

Page, W. D., & Nishenko, S. (2015). Assessment of Potential Tsunami Runup at the Humboldt Bay Generating Station Site (p. 89) [Internal]. PG&E.

Peterson, C. D., Carver, G. A., Cruikshank, K. M., Abramson, H. F., Garrison-Laney, C. E., & Dengler, L. A. (2011). Evaluation of the use of paleotsunami deposits to reconstruct inundation distance and runup heights associated with prehistoric inundation events, Crescent City, southern Cascadia margin. Earth Surface Processes and Landforms, 36(7), 967–980. https://doi.org/10.1002/esp.2126

Pritchard, C. J. (2004). Late Holocene relative sea-level changes, Arcata Bay, California: Evaluation of freshwater syncline movement using coseismically buried soil horizons [Masters Thesis, Humboldt State University]. http://dspace.calstate.edu/handle/2148/883

SAFFR Tsunami Modeling Working Group. (2013). Modeling for the SAFRR Tsunami Scenario—Generation, Propagation, Inundation, and Currents in Ports and Harbors. In S. L. Ross & L. M. Jones (Eds.), The SAFRR (Science Application for Risk Reduction) Tsunami Scenario (p. 136). U.S. Geological Survey Open-file Report 2013-1170-D. https://pubs.usgs.gov/of/2013/1170/d/

Sepúlveda, I., Haase, J. S., Liu, P. L. -F., Grigoriu, M., & Winckler, P. (2021). Non-Stationary Probabilistic Tsunami Hazard Assessments Incorporating Climate-Change-Driven Sea Level Rise. Earth's Future, 9(6), e2021EF002007. https://doi.org/10.1029/2021EF002007

Son, S., Lynett, P., & Ayca, A. (2020). Modelling scour and deposition in harbours due to complex tsunami-induced currents. Earth Surface Processes and Landforms, 45(4), 978–998. https://doi.org/10.1002/esp.4791

State of California. (2020). Humboldt County tsunami hazard map—South Bay [Tsunami hazard map]. California Geological Survey and California Governor's Office of Emergency Services. https://rctwg.humboldt.edu/sites/default/files/tsunamibrochures_humboldtcounty_october2020.pdf

State of California. (2021). Tsunami hazard area map, Humboldt county—Base map [Map]. California Geological Survey and California Governor's Office of Emergency Services.

Thio, H. K. (2019). Probabilistic Tsunami Hazard Maps for the State of California (Phase 2) (p. 168) [Technical Report]. AECOM.

Udo, K., Takeda, Y., & Tanaka, H. (2016). Coastal morphology change before and after 2011 off the Pacific Coast of Tohoku earthquake tsunami at Rikuzen-Takata coast. Coastal Engineering Journal, 58(4), 1640016-1-1640016–16. https://doi.org/10.1142/S0578563416400167

Wiegel, R. (1965). Protection of Crescent City, California from Tsunami Waves for the Redevelopment Agency of the City of Crescent (No. M–4825; p. 111).

Wilson, R., Davenport, C., & Jaffe, B. (2012). Sediment scour and deposition within harbors in California (USA), caused by the March 11, 2011 Tohoku-oki tsunami. Sedimentary Geology, 282, 228–240. https://doi.org/10.1016/j.sedgeo.2012.06.001